UiT
THE ARCTIC UNIVERSITY OF NORWAY

FACULTY OF SCIENCE AND TECHNOLOGY

Department of Geology

Time-lapse seismic interpretation of injected CO_2 plume at the Sleipner Field, North Sea

—

Espen Valberg

EOM-3901 Master's Thesis in Energy, Climate and Environment

June 2014

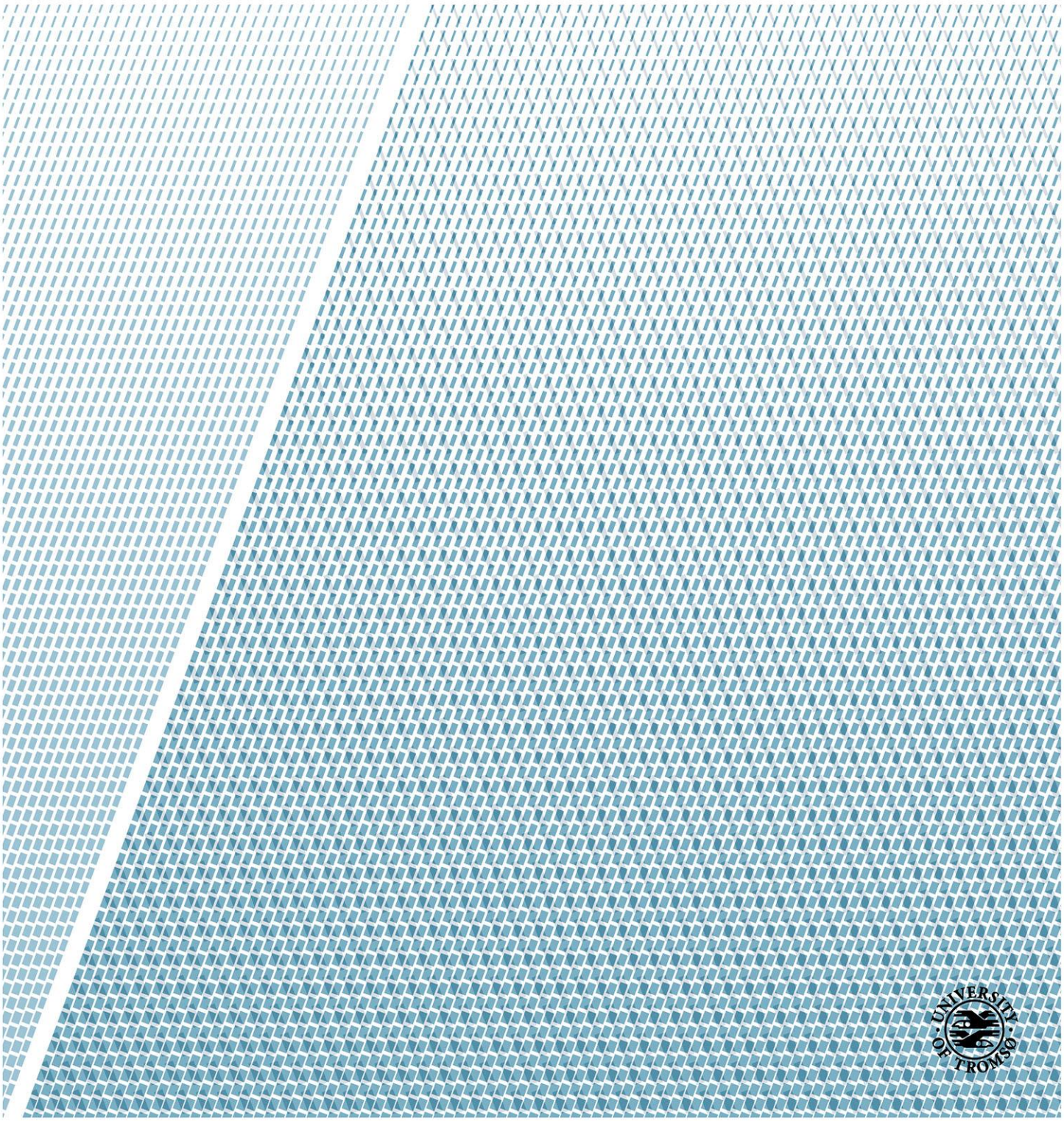

Abstract

One of the methods to cope with the increase of emitted greenhouse gases has been to capture CO_2 gas from a point source and storing it within the Earths subsurface; "Carbon Capture and Storage" (CCS).

Since 1996, Statoil and its partners have injected CO_2 into a saline aquifer called the Utsira formation located in the North Sea. About 0.9Mt of CO_2 is injected into the formation yearly, with a total injection volume estimated to be approximately 25Mt of CO_2. The reservoir conditions of the formation have been interpreted to be good, with porosities in the range 35-40% and permeability in the range 2-5 Darcy's. The injection is occurring at a vertical depth of approximately 1000m below the sea level, where the storage formation has a thickness of approximately 300m, and is overlain with sediments interpreted to constitute enough seal for the planned injection. The most widely used monitoring technique at the CCS project is to compare 3D seismic datasets obtained at different times, where the evolution of the CO_2 can be monitored in a 4D seismic time-lapse sequence.

In this thesis, four 3D seismic datasets have been interpreted for detecting and mapping the injected CO_2 at the Sleipner facility. One of the dataset was acquired before the injection began and the three others were acquired after 5, 8 and 10 years of injection.

The 4D seismic time-lapses have proven to be suitable for detection of injected CO_2, where small CO_2 thicknesses of only one meter can be visualized. The CO_2 from the three post-injection datasets is observed as a series of bright sub-horizontal reflections, where they have been observed to accumulate at nine specific layers within the storage formation. The accumulations are interpreted to be located beneath shales within the reservoir. Amplitude anomalies of the internal layers, and for the whole plume, have shown to have a general elliptical planform with the long axis in a NNE-SSW direction. This is presented to be a response of the topography of the capping layers.

Reflection amplitude-changes have been observed on the time-lapse seismic data, where the lower layers seem to be dimming and the upper layers seem to be brightening as more CO_2 is being injected. The dimming is proposed to be caused by several factors, including energy reduction of overlying brightening CO_2 layers and upward migration from deeper to shallower layers.

Storage security within the injection site have been examined, both the integrity of the caprock situated above the CO_2 plume and changes of the seabed surface. Neither show any signs of threat to storage security.

Acknowledgement

Nei har du sett, da var 5 års skolegang snart over! Det har vært en lang og innholdsrik tidsperiode, hvor jeg har trivdes veldig godt. Det er mange person som har vært gode å ha i disse årene, og ønsker å takke noen av dem her.

Først og fremst må jeg få takke min veileder, Stefan Bünz, for både hjelp til å velge relevante fag gjennom de siste årene samt finne en spennende masteroppgave som var litt ulik de tidligere.

Jeg ønsker spesielt å takke alle mine medstudenter, både mine klassekamerater på Energi og Miljø, og alle de ulike individene her på «geobrakka». Det har vært mange humørfylte stunder som har gjort skolegangen veldig mye lettere. Har ikke lyst til å nevne navn, i fare for forlegne andre, men spesiell takk til Kristian Kjerkreit må være med. Det har vært et kjempefint samarbeid fra første skoledag og nå helt til siste masterinnspurten.

En takk må også gå til fussball-spillet her på brakka - som har hjulpet godt for å døyve stresset i den siste tiden (til de flestest irritasjon (!)).

En kjempestor takk går også til min kjæreste og samboer Marta, som har hold ut med meg gjennom alle disse årene med sene kvelder og til tider sliten hjerne. Du har vært helt fantastisk!

Takk til Elizabeth, Leif og Amund som har hjulpet meg med engelsken min på masteroppgaven, da jeg i skrivende stund virker å være i hvert fall en fjerdedels dyslektiker. Thank you!

Da ser jeg fram mot en ny tid med nye utfordringer, dette blir bra!

Espen Valberg

Juni 2014

«Han kom, ble svett, dett var dett»

- Marve Fleksnes, lagerleder

Contents

1. Introduction

1.1 Objective

The primary objective for this thesis is to detect, map and understand the distribution of injected CO_2 in a sub-seabed storage formation, and how this distribution changes with continued injection. The secondary objective is to examine the integrity of the overlying caprock, and to map out potential changes due to leakage of underlying CO_2.

1.2 Increase of emitted greenhouse gases

Earth's population has grown very rapidly in the last decades; during the 20th century alone the world's population grew from 1.65 billion to 6 billion, which is a total increase of 263% (Worldometer, 2013). As the population continues to grow rapidly and global standards of living improve, the need for energy has begun to be pushed to new heights. In meeting this increased demand, an increase in energy consumption has been shown to also increase the amount of greenhouse gases emitted into the atmosphere. These increased greenhouse gas concentrations have been proven to have negative side-effects on the climate and environment (IPCC, 2007). These gases include Carbon dioxide (CO_2), Methane (CH_4), Nitrous oxide (N_2O), Hydrofluorocarbons (HFC_s), Perfluorcarbons (PFC_s) and Sulfur hexafluoride (SF_6). In the last decade, awareness of the gas emissions and their negative impacts on the climate has been granted much attention, both from the media and from expert panels; increased greenhouse gas emissions are globally thought of as being one of the hottest issues in recent history. Many of us will understand that this will probably be even a hotter issue in the years to come, as it seems we are heading towards a "point of no return".

1.2.1 High increases of emitted greenhouse gases in the last decade

The closing decades of the twentieth century and the early years of the present century were unusually warm. Globally speaking, the last 30 years have been the warmest years since accurate records began slightly over 100 years ago. Twelve of the thirteen years between 1995 and 2007, rank among the warmest in the instrumental record of global air surface temperature that began around 1850, with the years 1998 and 2005 being the warmest. Section from (Houghton, 2009).

Global greenhouse gas (GHG) emissions have grown considerably since pre-industrial times. The rapid increase in the atmospheric concentration of these greenhouse gases is thought to be caused by human activities, especially the more extensive use of carbon-based energy sources.

Gases have different warming potentials, which are expressed proportional the warming caused by one ton of CO_2. For example, 1Gt of CH_4 has the same warming effect on the Earth as 21Gt of CO_2. The global emissions of CH_4, N_2O, HFC_s, PFC_s and SF_6 have increased by over 70% in the period between 1970 and 2004 (figure 1.1). In the same period, the yearly emission of GHG into the atmosphere has been estimated to have grown from 28.7 to 49Gt of carbon dioxide equivalents ($GtCO_2$-eq), as seen in figure 1.1. The atmospheric increase of these gases has not been equal; CO_2 emission has increased approximately 80% between 1970 and 2004, and thus represents 77% of the total anthropogenic GHG emission in 2004. The sectors of largest growth in global GHG emissions between 1970 and 2004 are the energy- and transport sectors, with increases of 145% and 120%, respectively. Other sectors with large increases of global GHG emissions are the industrial (56%) and the land use (40%) sectors. Section from (IPCC, 2007).

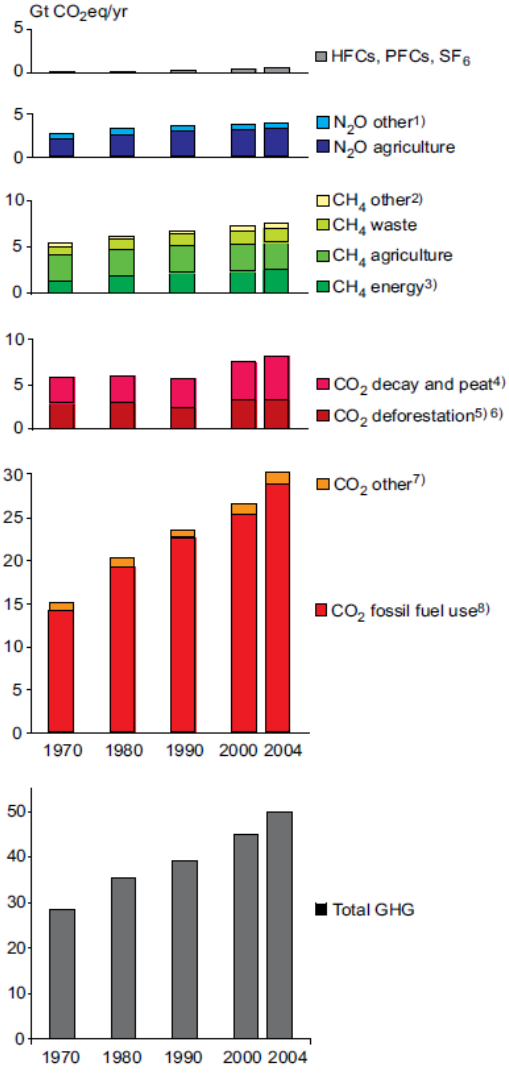

Figure 1.1: Global warming potential weighted by their global warming potential in the period 1970 to 2004. From (IPCC, 2007).
Notes:

1. Other N_2O includes industrial processes, deforestation/savannah burning, waste water and waste incineration.
2. Other is CH_4 from industrial processes and savannah burning.
3. Includes emissions from bioenergy production and use.
4. CO_2 emission from decomposition of above ground biomass that remains after logging and deforestation and CO_2 from peat fires and decomposition of drained peat soils.
5. As well as traditional biomass use at 10% of total, assuming 90% is from sustainable biomass production. Corrected for 10% carbon of biomass that is assumed to remain as charcoal after combustion.
6. For large-scale forest and scrubland biomass burning averaged data for 1997 – 2002 based on Global Fire Emission Data base satellite data.
7. Cement production and natural gas flaring.
8. Fossil fuel use includes emissions from feedstocks.

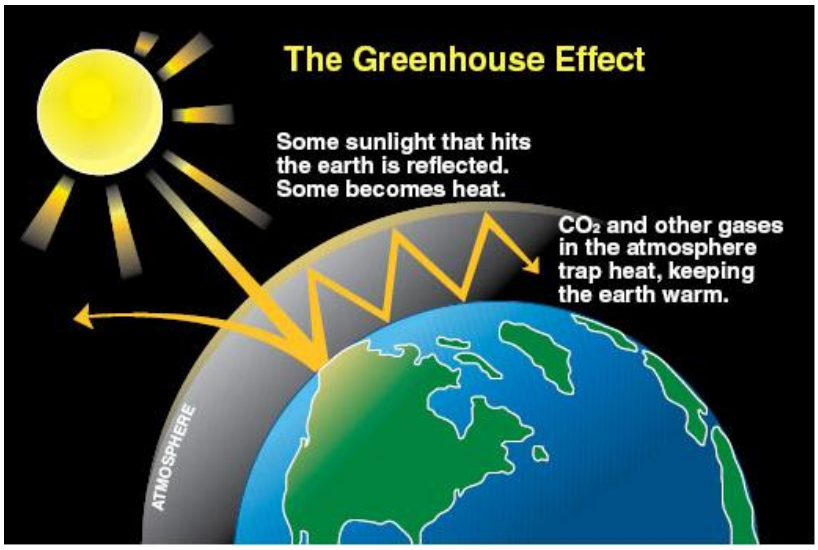

Figure 1.2: Schematic illustration of the greenhouse effect. It can be observed that the ultraviolet radiation emitted by the sun is absorbed at the earth. The earth will radiate infrared radiation which is absorbed by gases in the atmosphere, which again is radiating infrared radiation down do earth again and thus cause an extra warming earth. From (http://www.ecy.wa.gov/climatechange/whatis.htm, 2014)

Evidence continues to accumulate that the release of CO_2 via the burning of fossil fuels interferes dangerously with the climate system. Models predict that, without actions to curb the growth of GHG in the atmosphere, we risk triggering catastrophes, such as cessation of the dominant pattern of ocean circulation, loss of the West Antarctic Ice Sheet, and an increase in the number of category-five hurricanes. Greenhouse gases in the atmosphere change the climate by allowing ultraviolet light in and prohibiting the reflected infrared light from escaping into outer space; this is termed "the greenhouse effect" (figure 1.2). By burning fossil fuels, which are mainly composed of hydrogen and carbon, we add CO_2 into the atmosphere. In 2011, the Earth's atmosphere contained about 800 billion tons of carbon in the form of CO_2. Combustion of fossil fuels currently adds about 8 billion tons of CO_2 every year (figure 1.3). Naturally occurring "sinks", which extract CO_2 from the atmosphere, remove about 4 billion tons of CO_2 every year. This means that in 2011 there was a net input of 4 billion tons of CO_2 into the atmosphere. Section from (Büenz, 2013; CMI, 2011).

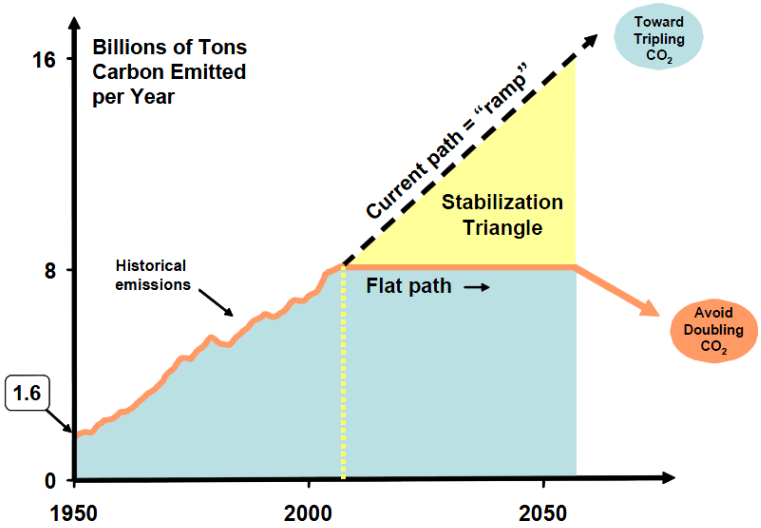

Figure 1.3: Yearly atmospheric increases of CO_2 in the atmosphere. The yearly increase in 1950 is estimated to have been about 1.6 billion tons, whereas in modern day it is estimated to be over 8 billion tons CO_2 emitted every year. By inhibiting the amount of emitted CO_2 from increasing, the curve will flatten out, and thus the decrease can begin. From (CMI, 2011)

1.2.2 Mitigation options

The observed rapid increase of atmospheric GHG has inspired a considerable amount of research in order to find new ways to reduce the emissions. The Carbon Mitigation Initiative (CMI, 2011) have proposed five main classes of ways to reduce the CO_2 emission into the atmosphere, where the overall goal is to "flatten" the CO_2 emission curve as can be seen in figure 1.3, such that every year the CO_2 emission increases by 8 billion tons.

Efficiency and conservation:

Increase of efficiency and conservation can be accomplished by several methods. It is mainly focusing on the *transport efficiency* (by changing the engine system from petrol to diesel, and to replace heavier materials with lighter), *Transport conservation* (by avoiding unnecessary driving in forms of better urban planning and better use of collective transport means), *building efficiency* (by better use of building insulations and installation of solar panels etc. on rooftops), and *efficiency in electrical production* (by replacing older turbines with newer and more efficient ones, especially at coal-burning facilities).

Fossil fuel based strategies:

Replace "dirty" (i.e. coal-based) energy sources with more environmentally friendly energy sources from natural gas-plants.

Nuclear energy:

The nuclear fission currently provides approximately 17% of the world's electricity, and produces little or no CO_2 in its production. Exchanging fossil fuel-based power plants for nuclear power plants will therefore reduce the amount of emitted CO_2.

Renewable- and bio storage energy:

Replacing the fossil fuel-based energy sources with renewable energy sources will reduce the amount of emitted CO_2 during energy production. This can be done by using *wind electricity* (extract the kinetic energy from the wind), *solar power* (extract the radiation energy from the solar radiation), and *wind hydrogen* (generation of hydrogen using wind energy). Bio storage is also an alternative to reduce the emission of CO_2 via the use of *biofuels* (where re-use of waste and other bio products is used for energy generation), and *forest- and soil storage* (where the deforestation is stopped, and reforestation is engaged, increasing the amount of carbon taken out of the atmospheric circulation and relegated to carbon sink.

Carbon Capture and Storage (CCS):

Theoretically, the capture and storage of the CO_2 generated by energy sources would mean that it is possible to continue using coal, oil and natural gas to meet the energy demand without emitting harmful gases into the atmosphere.

Carbon dioxide is being injected into underground saline formation at two location on the Norwegian continental shelf: at the Snøhvit field in the Barents Sea and at the Sleipner field in the North Sea. The CCS in general and the project occurring at the Sleipner field will be presented more in detail, as it is the study area for this thesis.

1.3 Carbon Capture and Storage (CCS)

1.3.1 What is CCS?

Carbon capture and storage is, as briefly explained in the previous subsection, one method to reduce the growing emission of CO_2 into the atmosphere. IPCC define this as:

> *"Carbon dioxide (CO_2) capture and storage (CCS) is a process consisting of the separation of CO_2 from industrial and energy-related sources, transport to a storage location and long-term isolation from the atmosphere" (IPCC, 2005)*

Point sources for CO_2 include large fossil fuel- or biomass energy facilities, major CO_2 emitting industries, natural gas production, synthetic fuel plants and fossil fuel-based hydrogen production plants (Büenz, 2013; IPCC, 2005).

Three main storage techniques are used in CCS projects (Figure 1.4): *oceanic storage* (CO_2 is released directly into the ocean water column or on the deep seabed), *industrial storage* (fixation of CO_2 into inorganic carbonates) and *geological storage* (CO_2 is stored in the pores of a reservoir rock via injection through a well; this will be described more detailed in the next subsection).

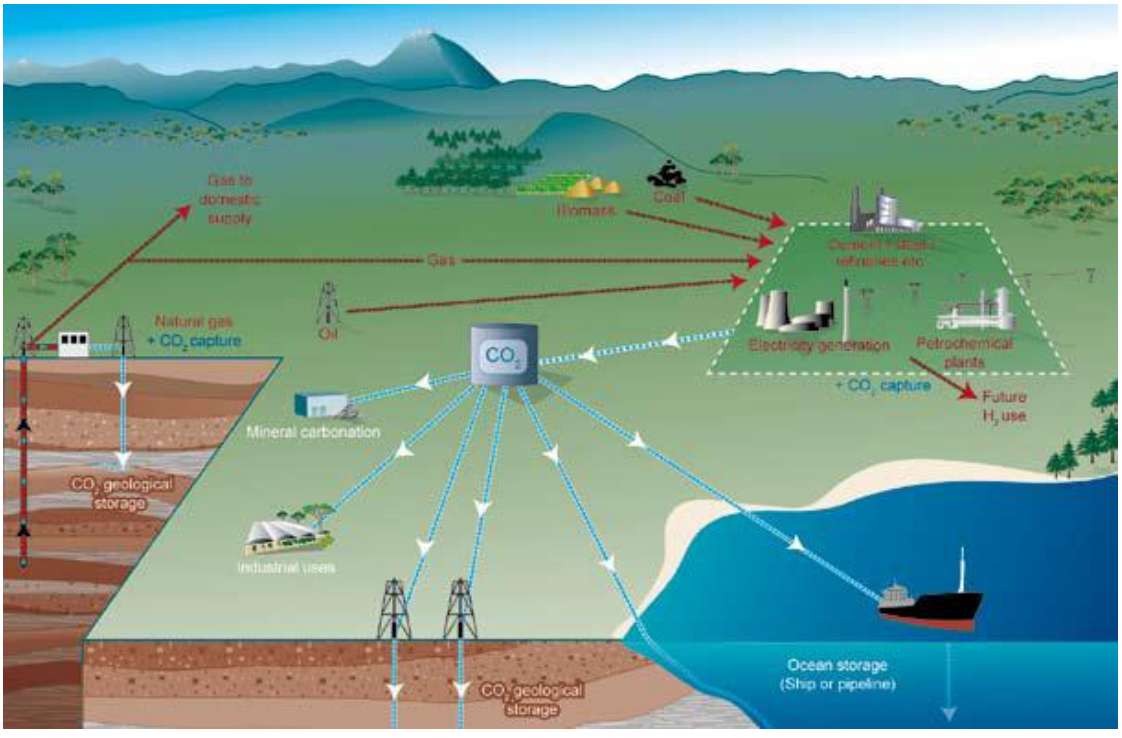

Figure 1.4: The three main CO_2 storage options. The options are divided into geological storage, ocean storage and industrial storage. From (IPCC, 2005)

1.3.2 Geological underground storage formations

The injection of CO_2 in deep geological formations involves many of the same technologies that have been developed in the oil and gas industry, and offers perhaps the most immediate method for ameliorating anthropogenic CO_2 emissions (Herzog, 1999). To be classified as a potential CO_2 storage formation, the formation must possess certain properties. These properties are used to describe the formation's ability to contain fluids, and are described and evaluated in the same way as for a hydrocarbon reservoir. These properties include porosity (the space between the grains), permeability (the ability of fluids to move within the storage reservoir), trap structure, and a sealing unit to prohibit the stored content to migrate further upwards (IPCC, 2005; Rafaelsen, 2013). A short description of the petroleum system will be given at the end of this chapter. The total amount of CO_2 that can be stored in an underground storage formation is dependent on both the values for the mentioned properties, but also on the volume of the formation.

Suitable storage formations can occur in both onshore and offshore sedimentary basins (natural large-scale depressions in the Earth's crust that are filled with sediments), as well as in unmineable coal beds (figure 1.5) (IPCC, 2005). The objective of underground storage is to contain CO_2 for a long enough period of time to mitigate global warming. The average storage time should be in the order of at least a few thousands of years, however, in a well-selected storage site, the retention time will most likely be indefinite. Furthermore, annual leakage from the storage site should not exceed 0.01% of the injected CO_2 (Andy Chadwick et al., 2008; Lindeberg & Bergmo, 2003).

As mentioned in the previous subsection, the CCS geological storage project taking place at the Sleipner field involves injecting CO_2 into an underground aquifer. An aquifer is a body of porous and permeable sedimentary rocks where there is water in the pore space. Injection into aquifers is the most widespread technique for geological storage as the aquifers tend to have relatively good porosities and permeabilities (IPCC, 2005; NPD, 2011). This technique will therefore be focused on further in the thesis.

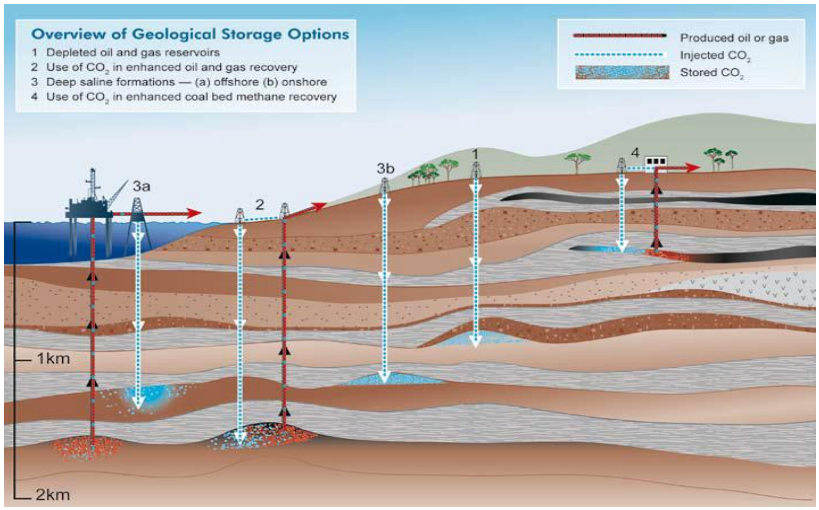

Figure 1.5: The four main storage options for CO_2 in geological formation. The four main types are storing in depleted oil and gas reservoirs, storing close to production fields to increase the production (enhanced oil recovery), storing into deep saline formations, and storing in unminable coal beds. From (IPCC, 2005)

1.3.3 CO_2 behavior in the underground saline aquifer

CO_2 storage in underground saline aquifers is generally expected to take place at depths below 800m, where the ambient pressures and temperatures result in CO_2 existing as a liquid or in a supercritical state (figure 1.6b) (IPCC, 2005). In a supercritical state, the CO_2 has the density of a fluid, but the compressibility of a gas (Rob Arts et al., 2004a). By maintaining the pressure regime as presented in figure 1.6a, the volume required for geological storage at depths beneath 800m is only a small fraction of what is required for lower pressures, indicating that more CO_2 may be stored at the underground locations in the supercritical state than in the liquid phase (IPCC, 2005; NETL, 2010).

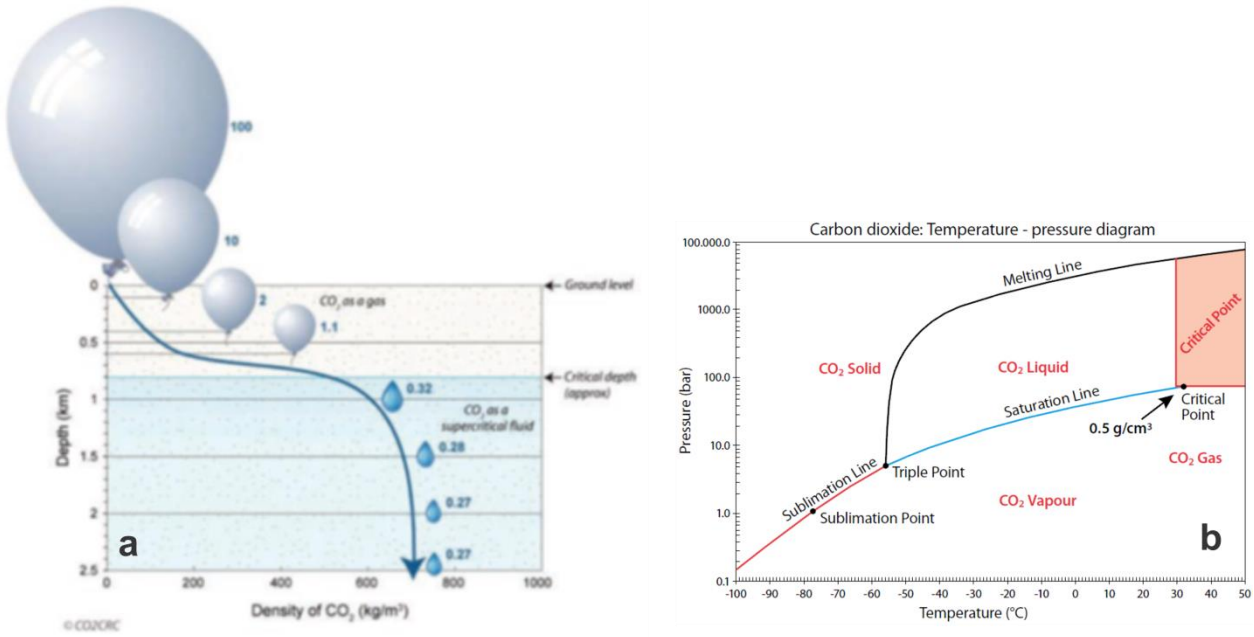

Figure 1.6: The effect of pressure on CO_2. a) In the subsurface with a normal pressure and temperature gradient the CO_2 will enter the fluid phase at about a depth of 700m, and is observed to shrink to only a fraction of the surface size. From (NETL, 2010) b) Temperature-pressure diagram for CO_2; it can be observed that above 30°C and 80 bars the CO_2 will enter the supercritical phase. When entering the critical zone, pure CO_2 will have a density of only 0.5g/cm^3. From (NPD, 2011).

Under supercritical conditions, the density of the CO_2 will range from 50-80% of the density of water (500 - 800 kg/m^3). When CO_2 is used in storage formations other gases are often added, e.g. methane and butenes, in order to maximize the flow, which alters the densities of the injected gas. How the CO_2 behaves after it leaves the injection well(s) is determined by the pressure gradients created by the injection well(s), the original hydraulic gradients, and the buoyancy force relative to the original formation fluids. Because the density of the CO_2 is up to 50% lighter than the normal formation fluid, the buoyance force tends to drive the CO_2 upwards while driving the formation fluids out of the trap structures. Furthermore, the behavior of the CO_2 is dependent on the geological characteristics of the storage formation and the trapping mechanisms. Section from (IPCC, 2005)

In summation, the injected CO_2 flows as a response to the combined pressure gradients, and will always flow towards the areas with the lowest pressure (this is the same as for hydrocarbons (Rafaelsen, 2013)).

When CO_2 is injected into a saline aquifer, the CO_2 will infiltrate the space originally occupied by the normal formation fluid. The fraction of the retained fluids depends on physical and geochemical trapping mechanisms. *Physical trapping* refers to structural and stratigraphical trap formations (figure 1.7a), as well as capillary trapping (figure 1.7b), all of which inhibit upward migration of the CO_2 mechanically. *Geochemical trapping* refers to reactions between the injected CO_2, the formation fluid (equation 1.1a) and the reservoir rock (equation 1.1b). On century timescales, the CO_2 can dissolve in the formation water and sink downwards due to gained density and is prohibited from migrating upwards towards the surface (solubility trapping). On millennial timescales, chemical reactions between the dissolved CO_2 and the host rock, especially iron minerals, which can lead to generation of carbon minerals and thus trap the CO_2 as solids (mineral trapping). Therefore, the storage security will enhance as the injected CO_2 is trapped over longer timescales (figure 1.8). The rate at which the CO_2 is trapped by the different mechanisms is dependent on the nature of the water flow in the storage formation, and will usually differ from one location to another. Section from (Hermanrud et al., 2009; IPCC, 2005)

$$CO_2(g) + H_2O \leftrightarrow H_2CO_3 \leftrightarrow HCO_3^- + H^+ \leftrightarrow CO_3^{2-} + 2H^+ \qquad (1.1a)$$

$$3\,Kfeldspar + 2H_2O + 2CO_2 \leftrightarrow Muscovite + 6\,Quartz + 2K^+ + 2HCO_3^- \qquad (1.1b)$$

Equation 1.1: a) Dissolution of CO_2 in formation waters eliminates the buoyant forces that drive it upwards (solubility trapping). b) Formation of bicarbonate ions by reaction with the sodium and potassium basic silicate or calcium, magnesium and iron carbonate or silicate minerals in the storage formation (mineral trapping).

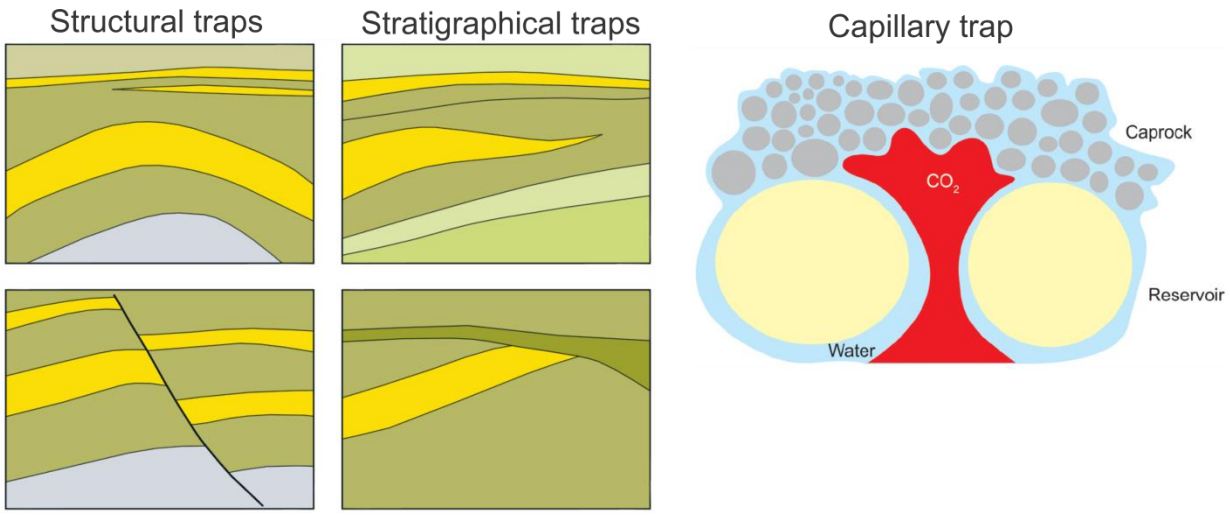

Figure 1.7: Trapping mechanisms. Left: Structural traps (included here are anticlinal and fault traps), stratigraphical traps (included here are pinch out and unconformity traps), and where the yellow color indicates sandstone layers while the green color indicates impermeable rock. From (NPD, 2011). Right: Capillary (residual) trapping, where the CO_2 is trapped inside a porous rock after having been flushed through. From (Hermanrud et al., 2009)

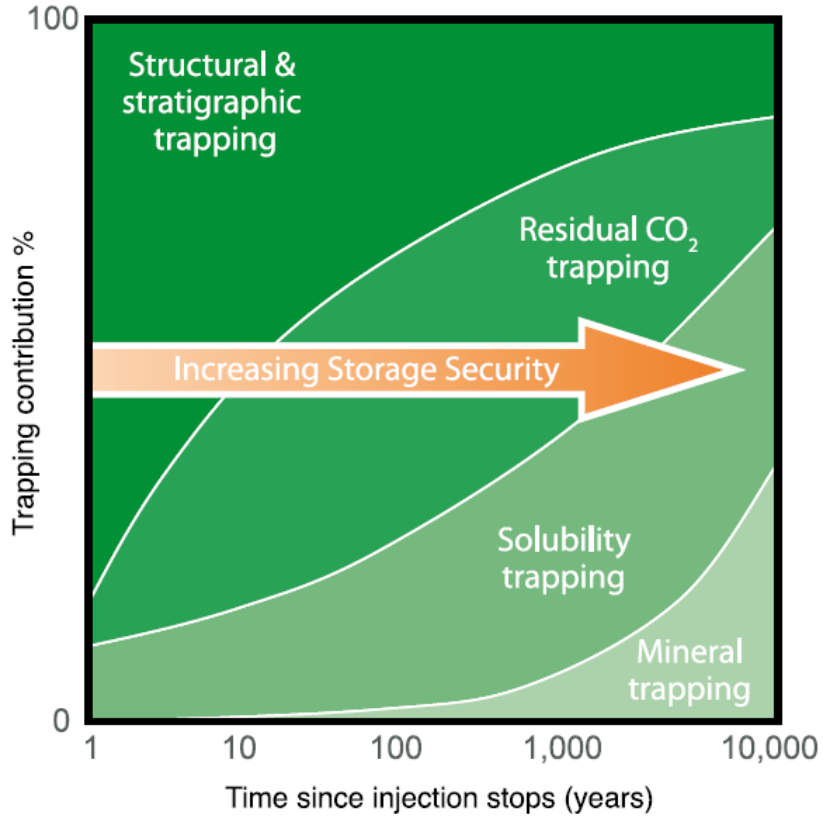

Figure 1.8: The storage security of a CCS project in a saline formation is dependent on a combination of physical and geochemical mechanisms. The first trapping mechanism is usually the physical trapping, however, over time geochemical trapping mechanisms increase and hence the storage security increases. From (IPCC, 2005)

1.3.4 Local impacts for CCS on saline formations

For safety reasons, it is necessary that the underground storage formation is capable of handling the amount of the injected CO_2 without impacting the marine/terrestrial ecology or groundwater. It is important to consider all potential environmental impacts of the CO_2 injection (Andy Chadwick et al., 2008). The main environmental consequence of leakage from a CO_2 injection formation is groundwater pollution from migration of CO_2 away from the main storage formation. Furthermore, injected CO_2 concentrations can become deadly for locally living organisms (Andy Chadwick et al., 2008). Lack of communication between the pore spaces in the reservoir (i.e. poor permeability) can result in a local pressure buildup near the injection well that can fracture the overlying sealing sediments, resulting in CO_2 leakage (R. A. Chadwick, Williams, Williams, & Noy, 2012).

1.3.5 Site screening and selection

In order to determine where to inject and store CO_2, one must consider different possible storage locations. The storage locations are evaluated on several geological criteria, which include *reservoir efficacy* (static storage capacity and dynamic storage capacity), *reservoir properties* (depth, net reservoir thickness, porosity, permeability, salinity and stratigraphy), and *caprock efficacy* (lateral continuity, thickness and capillary entry pressure) (Andy Chadwick et al., 2008) as seen in table 1.1 (below).

	Positive indicators	Cautionary indicators
RESERVOIR EFFICACY		
Static storage capacity	Estimated effective storage capacity much larger than total amount of CO_2 to be injected	Estimated effective storage capacity similar to total amount of CO_2 to be injected
Dynamic storage capacity	Predicted injection-induced pressures well below levels likely to induce geomechanical damage to reservoir or caprock	Injection-induced pressures approach geomechanical instability limits
Reservoir properties		
Depth	>1000 m < 2500m	< 800 m > 2500 m
Reservoir thickness (net)	> 50 m	< 20 m
Porosity	> 20%	< 10%
Permability	> 500 mD	< 200 mD
Salinity	> 100 gl^{-1}	< 30 gl^{-1}
Stratigraphy	Uniform	Complex lateral variation and complex connectivity of reservoir facies
CAPROCK EFFICACY		
Lateral continuity	Stratigraphically uniform, small or no faults	Lateral variations, medium to large faults
Thickness	> 100 m	< 20 m
Capillary entry pressure	Much greater than maximum predicted injection-induced pressure increase	Similar to maximum predicted injection-induced pressure increase

Table 1.1: Key geological indicators for storage site suitability. From (Andy Chadwick et al., 2008)

1.3.6 Monitoring techniques

After the site-screening and location for the CO_2 is done, one must choose monitoring tool such that the CO_2 injection can be followed from the surface. It is essential to acquire a baseline (i.e. pre-injection) image of the storage structure and to monitor the evolution of the CO_2 plume throughout the injection process. This can efficiently be done using 4D seismic imaging (Andy Chadwick et al., 2008; S. Holloway, 2004). The 4D seismic time-lapse dataset is comprised of several 3D seismic datasets acquired over the same area and with the same acquisition parameters, which make it possible to study the growth of the CO_2 plume over time. This monitoring tool has been providing the best results on offshore CCS projects and is the main tool used in this thesis. Additional monitoring techniques have been developed by the petroleum industry, though most have yet to be tested (Andy Chadwick et al., 2008; Rafaelsen, 2013) (figure 1.9).

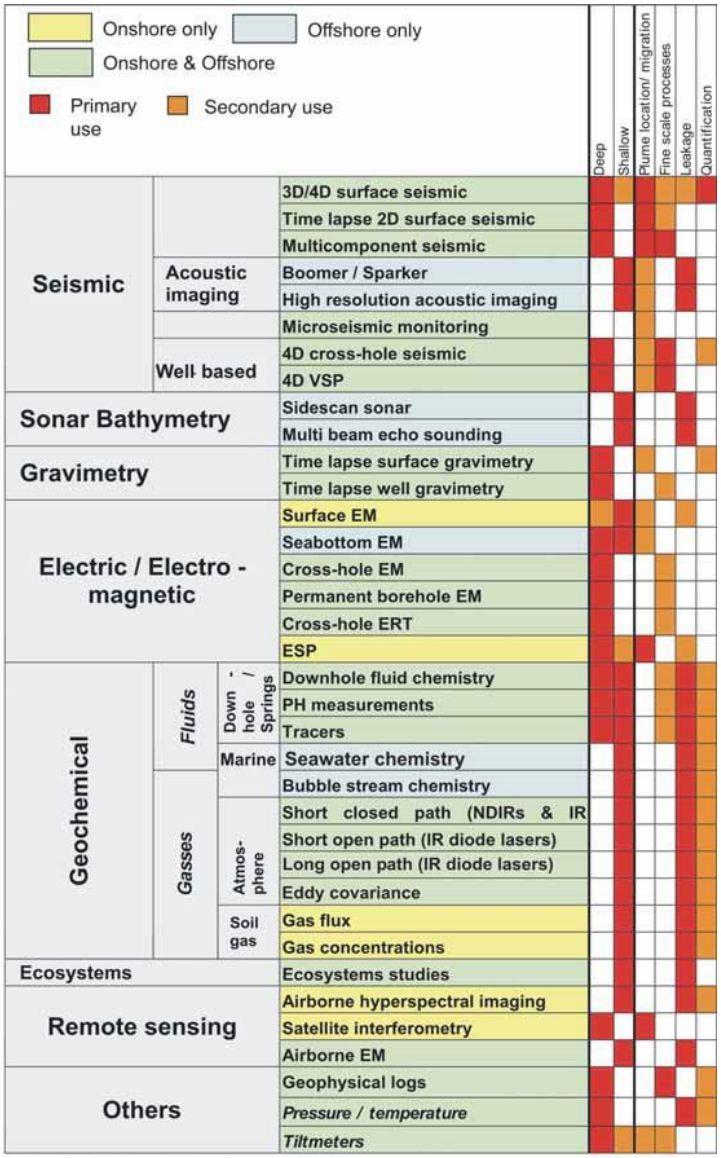

Figure 1.9: Showing variety of potential monitoring tools and techniques that can be applied to CCS projects. From (Andy Chadwick et al., 2008)

1.4 The petroleum system and general fluid migration

A petroleum system are geological elements and processes necessary to generate and store hydrocarbons. The elements are: 1) *Source rock* (a rock rich in organic matter that, if heated sufficiently, will generate oil and/or gas). 2) *Reservoir rock* (permeable rock that possesses the two properties porosity and permeability). 3) *Seal rock* (impermeable rock that inhibits further vertical migration of the hydrocarbons). 4) *Overburden rock* (sediments deposited above). The processes are: 1) *Generation* (hydrocarbon generation from the kerogen in the source rock). 2) *Trap formation* (Generation of a trap structure in the petroleum system) 3) *Migration and accumulation* (migration of hydrocarbon in permeable layers and accumulating under a trap formation). Section from (Rafaelsen, 2013; Selley, 1998).

Fluid migration is movement of fluids in underground strata with enough permeability, and is driven by the pressure and density differences, were the fluids tend to migrate towards areas with lowest pressures. It is therefore usual to find fluids at the shallowest part of an underground capping topography, where (if multiphase flow) the fluids are stacking upon each other due to density differences. In a hydrocarbon reservoir with hydrostatic pressure gradient, there can be found gas on top of oil on top of formation water (figure 5.10)). The migration of fluids is usually divided into two main modes (figure 5.10): *Primary* migration is referred to the fluid movement out from the source rock and into permeable carrier beds. *Secondary* migration is referred to internally movement of fluids inside the permeable carrier beds and into reservoir traps. The secondary migration in driven by pressure and density differences and the fluids normally migrates to the shallowest part of a permeable bed until it accumulates under an impermeable layer or upwards to the next layer. Section from (Rafaelsen, 2013; Selley, 1998).

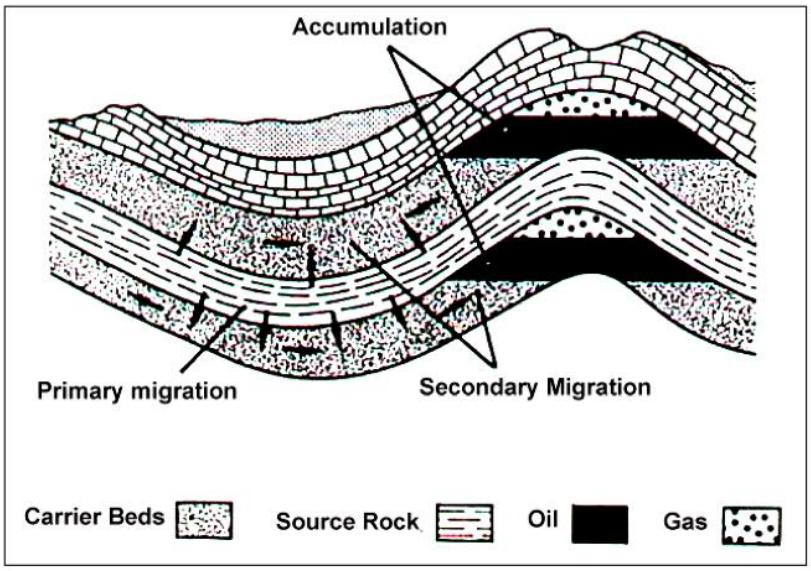

Figure 1.10: Illustrating the two main migration modes. Primary migration is referred to migration from source rock and into a permeable carrier bed. Secondary migration is referred to migration internally in the carrier beds where the fluid seek the areas with lowest pressures. Figure from (Tissot & Welte, 1984).

1.4.1 Seismic indication of fluid flow

The seismic datasets can be used for detection of fluids and their pathways in the subsurface, especially gas. Gas in the subsurface often produce seismic signals that can be separated from the surrounding strata since gas has lower densities and acoustic velocities compared to the normal formation fluids. Common types of gas indicators are: 1) *Amplitude anomalies* (referred to reflection amplitude following a certain pattern, and can be further divided into; bright spots and dim spots). 2) *Flat spots* (referred to the reflection pattern produced from the interface between a gas layer and the underlying fluid, which can be flat if the pressure regime is hydrostatic). 3) *Polarity/phase reversal* (referred to the change of polarity of the seismic signal when it enters a gas-bearing layer). 4) *Velocity effects* (referred to shifting of seismic reflectors beneath gas-bearing layers, where they are being observed lower than they are due to the change of acoustic impedance). 5) *Other effects* (referred to effects like loss of high frequencies and diffractions). The actual seismic response of these effects can be seen in figure 1.11. Section from (Andreassen, 2009). A general introduction into seismic theory will be presented in chapter 3 when the data and methods are explained.

Because the oil and gas (expelled from the kerogen in deep source rock) have lower densities compared to the normal formation fluids, they tend to migrate upward the subsurface to balance the density differences, often through sedimentary layers. When migrating upward the subsurface they often create observable "evidence" of their pathways that can be seen on seismic datasets. There are several different fluid flow pathways, and is divided into groups dependent on their characteristics on the seismic data: 1) *Gas chimneys* (referred to represent fractured caprock with irregularly distributed low-velocity gas-zones leaking from underlying reservoirs). 2) *Fault zones* (fluid migration through fractures and along fault planes that inhibits permeable zones). 3) *Acoustic pipes* (sub-vertical, circular, narrow zones of acoustic masking where the continuity of reflections is disrupted over a long vertical extent). (Andreassen, 2009; Loseth, Gading, & Wensaas, 2009) Examples of fluid flows observed on the seismic dataset can be seen in figure 4.12.

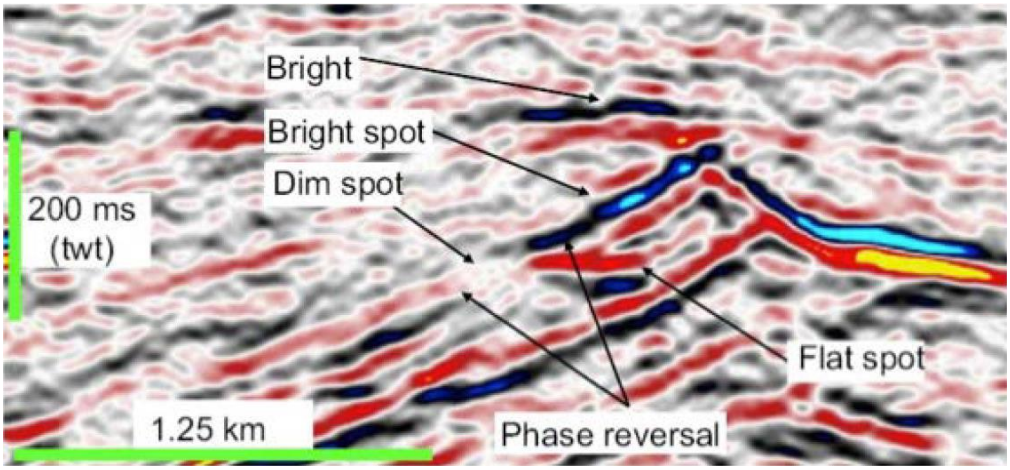

Figure 1.11: Seismic section indicating several indications for gas accumulation in a reservoir. From (Andreassen, 2009).

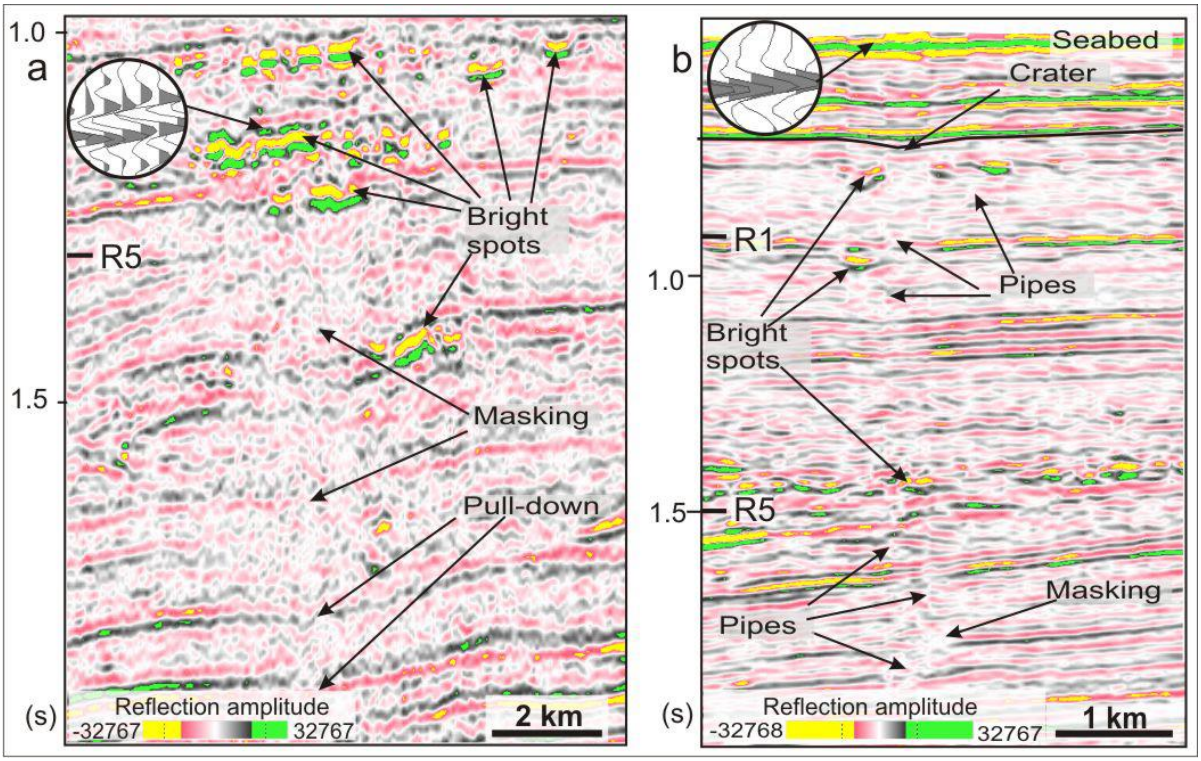

Figure 1.12: Seismic profiles indicating fluid flow. a) Showing pronounced zone of acoustic masking associated bright spots and pull-down of underlying reflectors. b) Showing acoustic pipes interpreted to represent fractures pathways for gas-bearing fluids, and associated acoustic masking and bright spots. The fluid flow pathway can be followed up to a pockmark crater on a buried horizon. From (Andreassen, 2009).

2. Study area

The focus of this thesis is the injection and storage of CO_2 at the Sleipner fields. At the Sleipner gas field in the North Sea, CO_2 is being stripped from the produced natural gas, and injected into a sand layer called "Utsira storage formation", also referred to as "Utsira sand" and "Utsira reservoir", and the project is considered as the first application of CO_2 storage in deep saline aquifers in the world (A. Chadwick, Arts, Eiken, Williamson, & Williams, 2006b; Torp & Gale, 2004). In 1996, Statoil and its partners started the injection of CO_2 from the Sleipner East platform, where CO_2 is injected into a saline aquifer, the Utsira formation, at a depth of about 1000m below the seabed with an annual injection rate of about 0.9Mt CO_2 (Rob Arts et al., 2004a; Hagen, 2012). The CO_2 is separated from the Sleipner West field, and injected into the Utsira formation through a 2.3 km long horizontal well (figure 2.1) (R. Arts et al., 2004b).

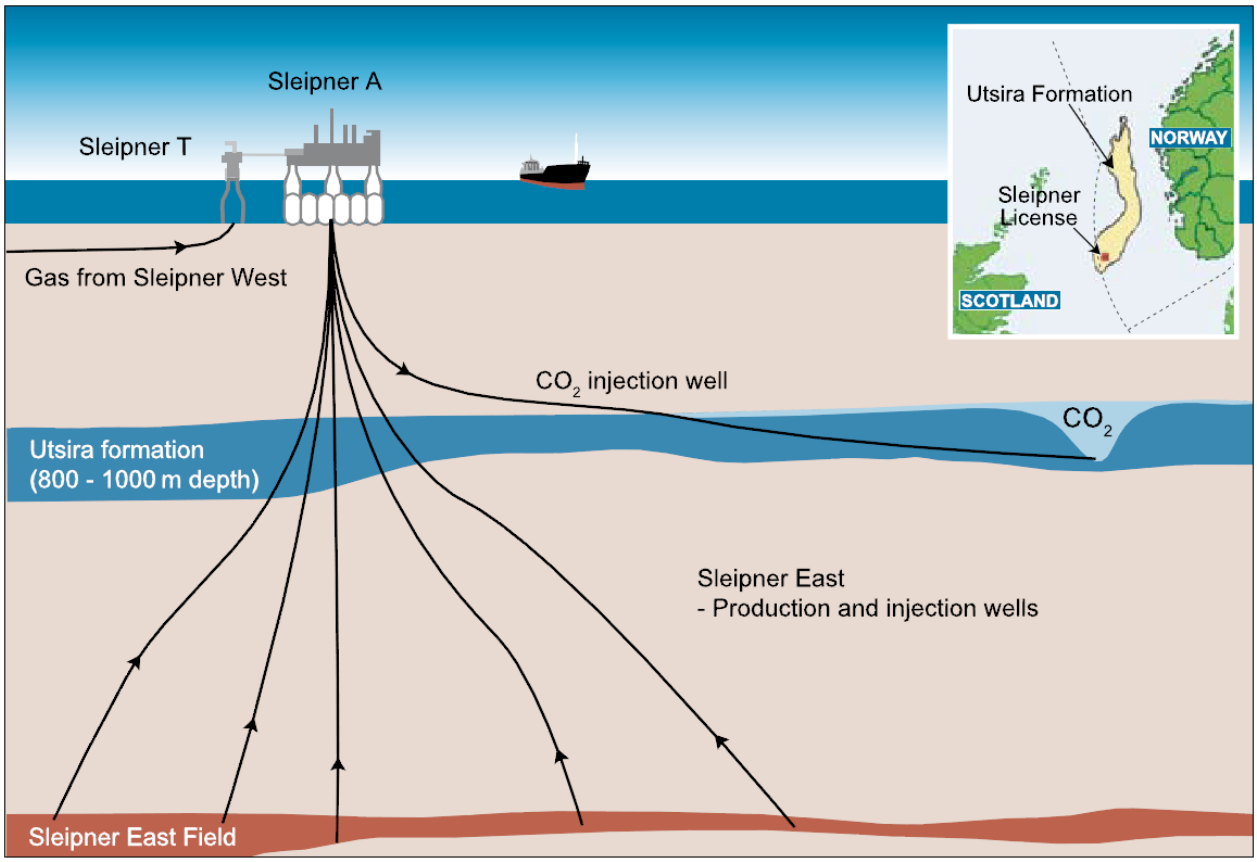

Figure 2.1: Simplified image of the cross section at the Sleipner CCS facility. The CO_2 is being injected from the same platform as production from the Sleipner east field is occurring at. Inset: Location of the Utsira formation and the Sleipner license. From (IPCC, 2005)

The Sleipner fields are located in the Norwegian block 15/9 in the North Sea, approximately 250 km from the west coast of Norway, close to the UK border (figure 2.1 inset). The offshore platforms on the Sleipner licenses are producing gas/condensate from the Tertiary and Jurassic reservoir, located underneath the injection formation by near-vertical wells (figure 2.1) (S. Holloway, 2004).

According to official Norwegian government sources the Sleipner West field originally contained 202 GSm^3 rich gas, which has a CO_2 content ranging from 4 to 9.5% (S. Holloway, 2004). To be able to deliver natural gas directly from the Sleipner West into the gas pipelines, transported and sold to Europe, the CO_2 content in the gas has to be reduced to a level beneath 2.5%. This reduction of CO_2 requires a CO_2 removal process from the gas (S. Holloway, 2004). The CO_2 is removed from the natural gas by an active amine process in one of the processing modules at the Sleipner T platform (located at the Sleipner East Field) (S. Holloway, 2004). Due to the high CO_2 taxes, the extracted CO_2 from the natural gas are stored in the underground Utsira formation rather than being vented into the atmosphere (S. Holloway, 2004).

In addition, to reduce emission of CO_2, the injection and monitoring of CO_2 provides further knowledge about the fluids behavior in the subsurface and is very suitable for developing feedback models. The CCS project has received more attention than predicted, with several SACS (Saline Aquifer CO_2 Storage) projects that have followed the injection. (Andy Chadwick et al., 2008). This will hopefully provide an inspiration for other companies to consider similar projects in the future.

2.1 Short geological description and development

The North Sea basin is an epicontinental basin, confined by the Scandinavian and British landmasses, where a seaway connects it in the north with the Norwegian-Greenland Sea (Gregersen, Michelsen, & Sørensen, 1997). The North Sea has experienced three major episodes of extensional tectonism between the Permian and Mesozoic time periods, which created two main graben structures; the Central Graben in the south central part and the Viking Graben in the northern part, with adjacent structural elements (figure 4.2) (Gregersen et al., 1997; NPD, 2011).

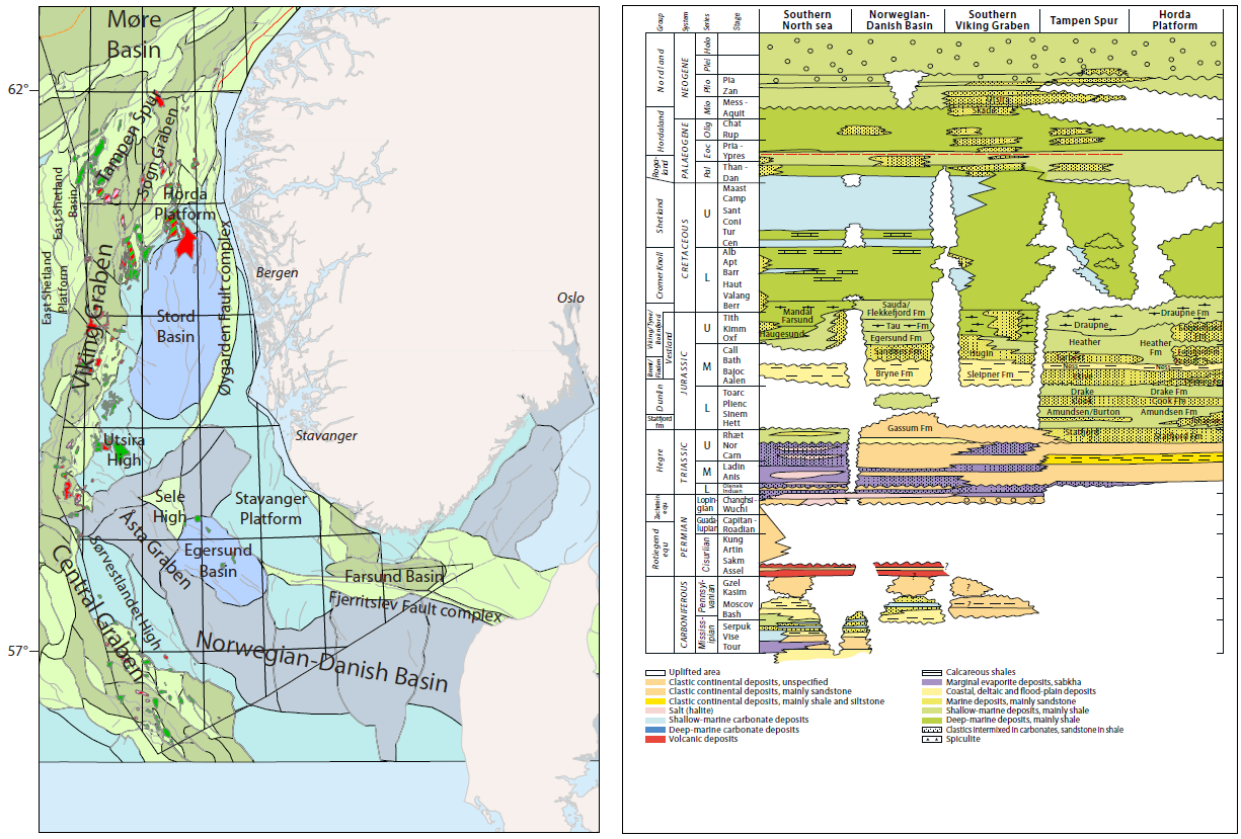

Figure 2.2: Main geological structures (left) and litostratigraphic chart (right) of the North Sea. From (NPD, 2011)

Major tectonic activities in the region ceased by the Early Cretaceous and the basin became dominated by post-rifts, regional subsidence, and was filled in by sediments that were supplied from the surrounding topographical highs (Gregersen et al., 1997). Four main periods of depositional sequences occurred in the Cenozoic time; Paleocene, Eocene, Oligocene and Miocene, which are interpreted to be the main sediment infilling in the upper parts of the North Sea (Gregersen et al., 1997). During the Cenozoic, uplift of basin margins due to inversion and thermal subsidence created by warming of the down-faulted blocks produced a general eastward dip that created a series of submarine fans transported from the Shetland Platform towards the East (Head, Riding, Eidvin, & Chadwick, 2004; NPD, 2011). The sands transported from the Shetland Platform

in the west interfingered by the overlying Hordaland Group and the underlying Rogaland Group (Gregersen et al., 1997). In the Miocene a deltaic system had developed from the Shetland Platform towards the Norwegian sector of the North Sea and is represented by the Skade and Utsira formation (NPD, 2011) (figure 2.3 & 2.4). Due to major uplift and Quaternary glacial erosion of the Norwegian mainland, thick sequences of material were deposited into the North Sea during the Neocene (Head et al., 2004; NPD, 2011). The majority of sediments from the Paleocene to Pliocene time periods can be observed in figure 2.4, where it displays a prograding deltaic system from the west, supplying sandy and silty sediments to the Norwegian sector (Ramberg, Bryhni, Nøttvedt, Solli, & Nordgulen, 2006).

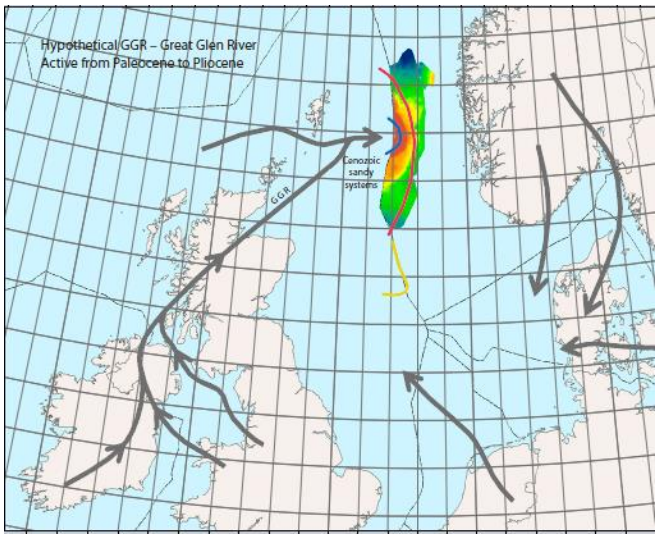

Figure 2.3: Illustrating sedimentary deltaic sediment supply from the west during the Paleocene to Pliocene. From (NPD, 2011)

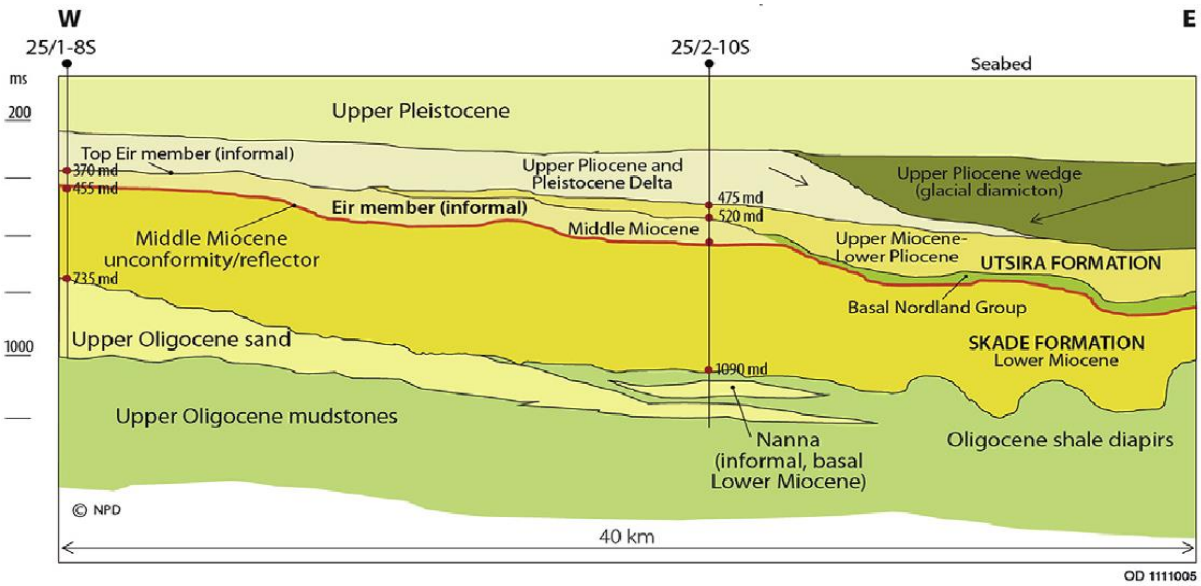

Figure 2.4: Geological cross-section over the North Sea, where eastward basinally infill can be seen. From (Pham et al., 2013)

2.2 The Utsira storage formation

2.2.1 Extent and geology

The Utsira storage formation extends over 400 km from north to south, and between 50 to 100 km from east to west, which gives an approximately formation area of 26 000 km^2 (figure 2.5) (Torp & Gale, 2004). The top of the Utsira formation (figure 2.5a) has a smooth variation in depth, with a range from 500m in the northwest side, and over 1500m in the north. Around the Sleipner area, the depth to the formation lies in the range 800-900m. From the thickness map (figure 2.5b) it can be observed that the thickness of the formation is quite variable, with thickness from about 25m in the thinnest region, to about 300m in the thickest region. There are two main depocentres in the formation, with one located in the north (where thickness locally exceeds 200m) and one in the southern region (where the thickness locally are ranging up to 300m, at the Sleipner area). The top of Utsira formation near Sleipner possesses a general dip to the south and is characterized by small domes of low relief, while the base of Utsira formation is more complex and is characterized by numerous mounds (R. A. Chadwick et al., 2004a; Gregersen et al., 1997).

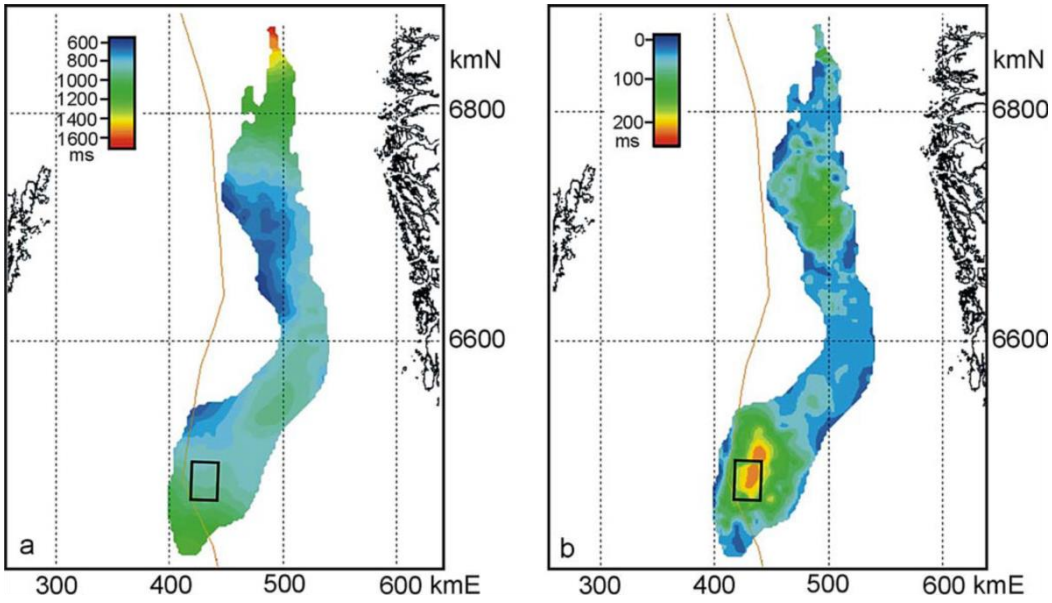

Figure 2.5: Illustrating the regional extent of the Utsira formation. a) Estimated depth to the top of the formation. b) Thickness of the formation, calculated from the Utsira top and down to Utsira base. The black square indicates the injection site, where the thickness of the formation is at the greatest and depth to top is in the range 8-900m. From (Torp & Gale, 2004)

Since the Utsira formation is not a hydrocarbon reservoir, it has not been well studied prior to its emergence as a candidate for underground CO_2 storage, and the knowledge of the fluid flow system in these shallow parts are relatively scarce. The regional reservoir maps were constructed from several 2D seismic data lines that constitute approximately 16 000 km 2D lines, and information

from around 130 wells penetrating the reservoir unit (R. A. Chadwick et al., 2004a). The Utsira sediments comprise of a basinally restricted deposit of Mio-Pliocene age, with recent age determination conducted biostratigraphically in a well several kilometers south of the injection site to range from middle Miocene (c. 11 Ma) to earliest Pliocene (c. 3Ma) (R. A. Chadwick et al., 2004a). The eastern and western limits are defined by stratigraphical onlap (figure 2.6); to the southwest it passes laterally into finer-grained sediments and to the north it occupies a narrow, deepening channel (displayed in figure 2.5a) (R. A. Chadwick et al., 2004a; Gregersen et al., 1997). Locally in the north, depositional patterns are quite complex with some isolated depocentres, and smaller areas of non-deposition within the main depocentres (R. A. Chadwick et al., 2004a).

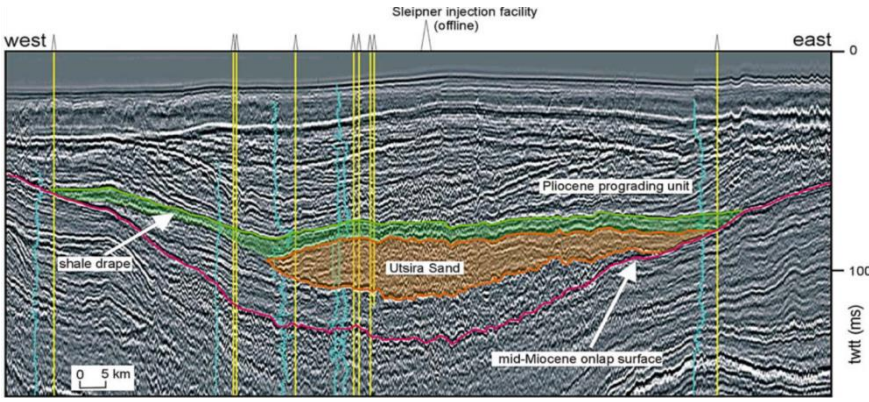

Figure 2.6: Regional seismic line the Cenozoic sag-basin through the southern part of Utsira formation. From (Torp & Gale, 2004)

The sand-dominated packages of the Utsira formation are identified on wire-line logs from relatively low gamma ray, sonic velocity, and neutron density values (Gregersen et al., 1997; Zweigel et al., 2004). From the well-logs spikes of high gamma ray, velocity and density values can be observed. The spikes in the gamma-ray values can be explained by several reasons, e.g. certain minerals included in the sand (glauconite, illite etc.), or by the presence of finer-grained sediments in the sand (Henriksen, 2013; Rider, 1996). Since spikes are observed in other logs as well, it can be assumed that the gamma-ray spikes are not caused by presence of certain minerals, but are most likely caused by thin intra-reservoir shale layers interfingering with the sand packages and have a similar petrophysical characterization as the shales from the overlying Nordland shales (Zweigel et al., 2004).

It is possible to differentiate between two types of inter-reservoir shale layers in the Utsira formation. Throughout the logs relatively small spikes can be observed located within the whole reservoir, interpreted to be small (0.5 – 1m) shales, and one larger spike close to the top of the reservoir, interpreted to be a thicker and more continuous shale layer (6 – 7m) (figure 2.7) (Zweigel et al., 2004). The thicker shale layer was interpreted to be more or less continuous over the injection area. It is separating an eastward thickening sand body (referred to as "(upper) sand package" in the thesis) from the underlying main part of the Utsira formation, and consist of the same sand material as the main reservoir (Hagen, 2012; Zweigel et al., 2004). Diverging from the small inter-reservoir shale layers, the large shale layer can be correlated between several wells, as displayed in figure 2.7, and it is possible to observe the growth of the sand body in the E-W direction, which

gives a different (though very small – 0.3º) dip difference between the top Utsira and large shale layers. This can, however, make a significant difference of the migration route for the injected CO_2 in whether it accumulates and migrates under the thick shale or it accumulates and migrates under the Utsira reservoir top.

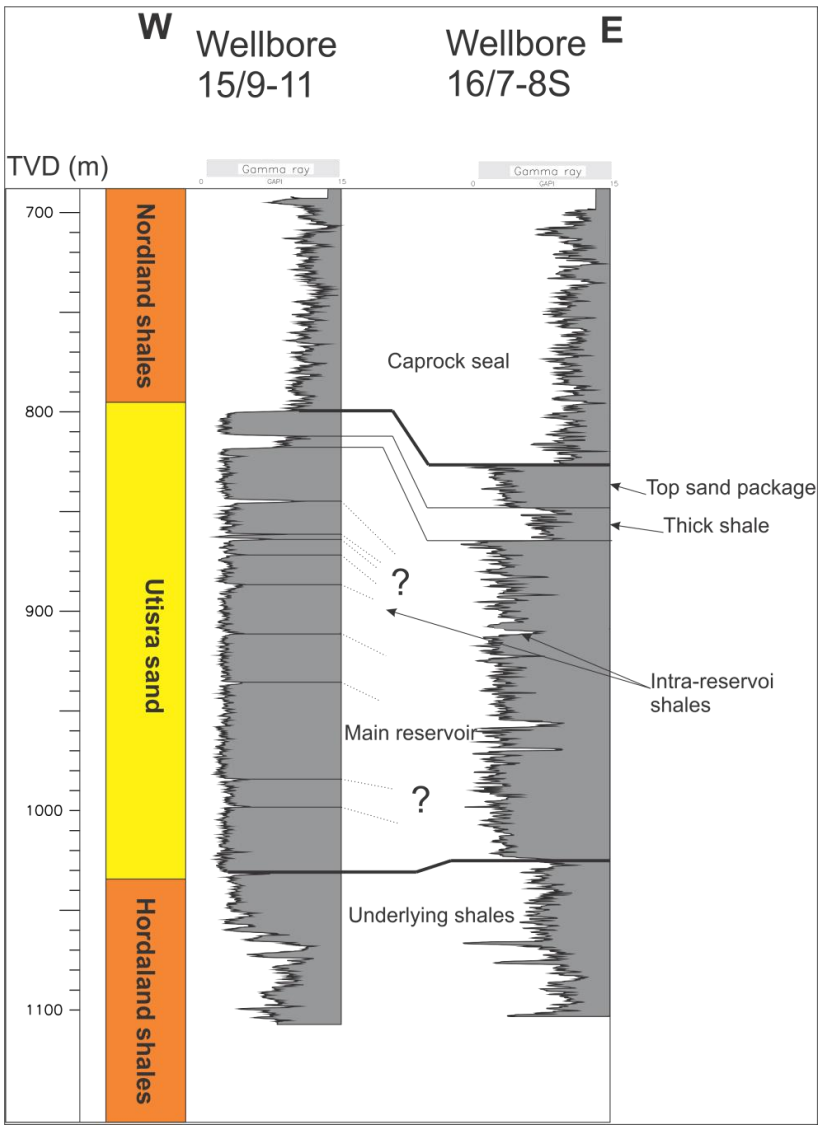

Figure 2.7: Showing two wells correlated over the Utsira formation or sand in the direction W-E. It can be seen that there are several spikes on the gamma ray log over the sand, indicating shale layers, with one thick close to the caprock seal and several small ones in the main reservoir. The thick shale is enough prominent to be correlated between the wells in the same way as for the top and base of Utsira. However, the small shales within the reservoir are not so prominent, and are impossible to correlate between the wells. Distance between the wells is about 10km. Origin of the well data is gathered from NPD (NPD, 2014a, 2014b).

There is, however, no wells that penetrate the Utsira formation relatively close to the injection site, since the injection well is a horizontal well (figure 2.1) penetrating the formation several kilometers away from the injection site (Bickle, Chadwick, Huppert, Hallworth, & Lyle, 2007).

2.2.2 Direct over and underburden of Utsira formation

Before the injection of the CO_2 can take place, it is crucial to conduct a complete investigation of the over- and underburden at the injection site, as mentioned in chapter 1. The most important aspect of the investigation is to be confident that the overburden does not exceed a critical limit for the planned injection volume, but since the underburden in the storage site contains mud characteristics, further investigations need to be conducted before CO_2 can be injected.

The overburden can be divided into three main sealing units (figure 2.8). The direct overburden of the Utsira formation is the lowest seal unit, which forms a shaly basin-restricted unit of approximately 50 – 100m thick and is a part of the Nordland Group (R. A. Chadwick et al., 2004a). This seal extends more than the estimated area of migration of the planned injected CO_2 and is interpreted to be the primary sealing unit (R. A. Chadwick et al., 2004a). Cut samples of the unit have been tested via core samples and it is estimated that it could trap a CO_2 column of several hundred meters and form a satisfactory seal to free CO_2 (with capillary entry pressures in the range between 3 and 5.5 MPa) (R. A. Chadwick et al., 2012; R. A. Chadwick et al., 2004a). Situated above this unit is the middle seal, which mostly comprises of prograding sediment wedges of Pliocene age, dominantly shaly in the basin center, but coarsening into a sandier facies upwards and towards the margins (R. A. Chadwick et al., 2004a). Above this is the upper seal which comprises of glacio-marine clays and glacial tills of Quaternary age (R. A. Chadwick et al., 2004a).

The argillaceous nature of the caprock lacks visible faulting. It is likely plastic, in a self-sealing mechanical state, and it accounts for a considerable thickness (lowest + middle seal is about 200m), together with an additional 500m of mostly fine-grained glacial tills, were considered to constitute an effective seal (Andy Chadwick et al., 2008).

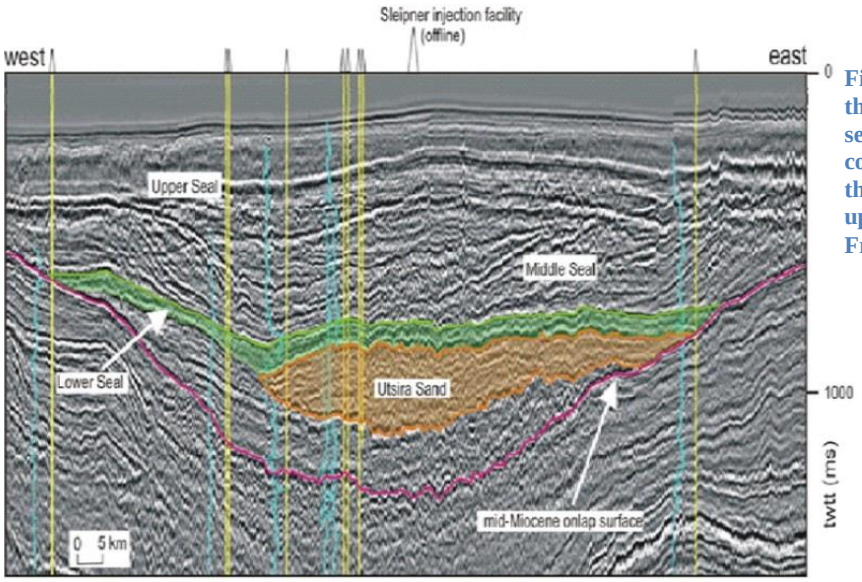

Figure 2.8: Seismic crossection through the storage site, indicating the three sealing units. The three sealing units is composed by the lower seal found near the Utsira top, the middle seal and the upper seal lying in the uppermost part. From (S. Holloway, 2004)

The direct underburden of the Utsira formation consists of predominantly shaly sediments from the Hordaland Group, which exhibit severe deformation by soft sediment mobilization and polygonal faulting. The deformation is presumed to be triggered by the rapid deposition of the marine Utsira formation sediments on the underlying muddy, gas-charged Oligocene and Lower Miocene deposits (figure 2.9) (Gregersen et al., 1997; Zweigel et al., 2004). On the Utsira formation base, mud diapirs and mud volcanoes can be found (figure 2.9a), along with local depressions on the Utsira formation top, created by the compressions of these mobilized soft sediments, resulting in thickness variations of the formation (Gregersen et al., 1997; Zweigel et al., 2004). There is no evidence for faulting in the interior of the Utsira formation, with the exception of the margins of some of the mobilized shales and diapirs (figure 4.9b), but it may constitute a threat to storage safety if the shales re-mobilize or the faults re-activates in later periods (Andy Chadwick et al., 2008; Zweigel et al., 2004).

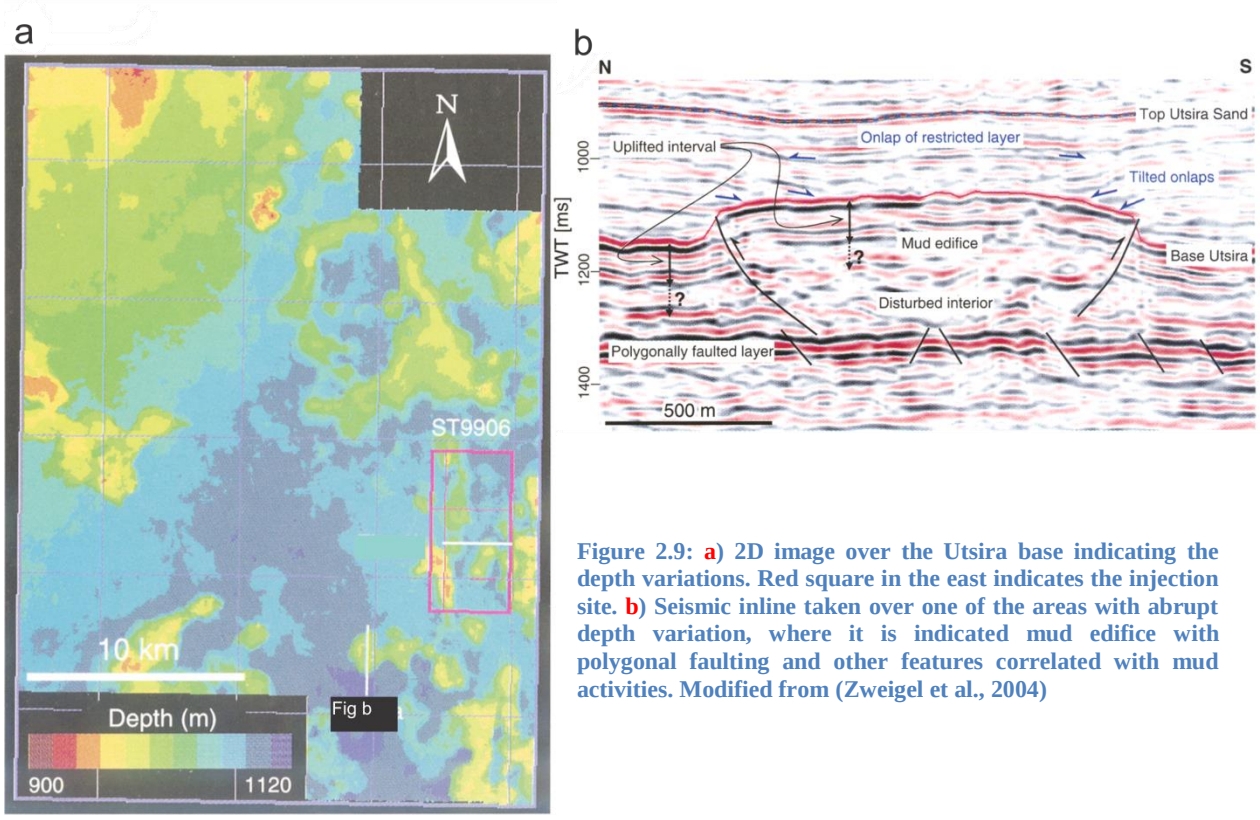

Figure 2.9: a) 2D image over the Utsira base indicating the depth variations. Red square in the east indicates the injection site. b) Seismic inline taken over one of the areas with abrupt depth variation, where it is indicated mud edifice with polygonal faulting and other features correlated with mud activities. Modified from (Zweigel et al., 2004)

The CO_2 injection site is positioned below a dome structure in the top Utsira formation. The dome has a diameter of approximately 1.2km and a height above spill-points of approximately 12m with the top of the dome located about 820m TVDss (Zweigel et al., 2004). The spill points are saddles or "channels" that link the dome to other domal structures in the north, south and west (Zweigel et al., 2004). Since the trap is of such short relief it is important that the estimation for the time-depth conversion is accurate, and a wrong measure of only a few percent will correspond to poor estimations for the trap and CO_2 migration.

2.2.3 Reservoir properties

The reservoir properties were measured almost exclusively from ditch cuttings, along with a few short cores obtained from the wells that penetrated the formation (Zweigel et al., 2004). The macroscopic and microscopic analysis of the cores and cut samples of the Utsira sand (table 2.1) demonstrate unconsolidated and uncemented medium to well sorted sand, with grains predominantly angular to sub-angular, and consist primarily of quartz with some feldspar and calcite fragments (R. A. Chadwick et al., 2004a; Zweigel et al., 2004).

Well	15/9-A23	15/9-A23	15/9-A23	15/9–16	15/9–16	15/9–16	15/9–16	15/9–15
Sample depth (mMD)	1080.04	1080.80	1084.19	850–860	890–900	950–960	1000–1010	880–890
Detrital grains								
Quartz	72.3	71.4	76.1	50.7	66.7	58.7	76.7	65.3
Feldspar	8.5	14.1	4.9	7.3	3.7	4.0	2.7	2.0
Muscovite	0.5	0.0	0.5	0.0	1.3	0.3	0.0	0.7
Biotite	0.5	0.0	0.0	0.0	0.0	0.0	0.0	0.0
Calcite (shell fragments)	11.2	7.3	5.4	18.0	17.0	8.0	7.7	4.7
Clay pellets	3.7	2.1	3.3	1.3	1.0	0.0	0.3	0.3
Glauconite	0.0	0.0	0.0	1.3	1.0	0.7	0.7	0.7
Organic matter	0.0	0.0	0.5	1.0	0.3	0.0	0.0	0.0
Matrix	0.5	1.0	0.0	0.0	0.0	0.0	0.0	0.0
Heavy minerals	0.0	1.6	0.0	0.0	0.0	0.0	0.0	0.0
Detrital rock fragments								
Chert	0.0	0.0	0.0	0.0	0.0	1.3	0.3	0.0
Quartzite	0.0	0.0	0.5	0.3	0.7	2.3	3.7	0.7
Gneiss	0.5	0.0	0.0	0.3	1.0	0.0	0.7	0.0
Sandstone	0.0	0.0	0.0	0.0	0.0	0.3	0.3	0.3
Shale/schist	0.0	0.0	0.0	4.3	1.0	16.3	4.7	23.3
Diagenetic (cements etc)								
Illite cement	1.1	0.0	1.6	0.0	1.0	0.0	0.7	0.3
Illite pseudomorph	0.0	0.5	1.1	1.3	0.3	0.0	0.0	0.0
Chlorite rim	0.0	0.0	5.4	0.0	0.0	0.0	0.0	0.0
Chlorite cement	0.0	0.0	2.7	0.0	0.0	0.0	0.0	0.0
Calcite cement	0.5	0.5	0.5	0.0	0.0	0.0	0.0	0.0
Quartz cement	0.0	0.5	0.0	0.0	0.7	0.0	0.3	0.0
Pyrite	0.0	0.5	0.0	14.0	4.3	8.0	1.3	1.7
Siderite	0.5	0.0	0.0	0.0	0.0	0.0	0.0	0.0
Sum clays	4.8	2.6	14.1	4.0	3.3	0.7	1.7	1.3
Sum components	100.0	99.5	102.7	100.0	100.0	100.0	100.0	100.0

Table 2.1: Showing the results from the modal analysis of the Utsira sand samples. All samples are obtained from ditch cuttings, except the results form well 15/9-A23 which is obtained from the Utsira sand core. All numbers in Vol. % of the solid portion of the sample. From (Zweigel et al., 2004)

The porosity of the Utsira sand was determined by modal analysis from thin sections, by liquid invasion on core samples, and from density logs (Zweigel et al., 2004). There was much variation in the measurements, but an average porosity of 35 – 40% was considered being a good estimate which is supported by the shallow burial and low compaction rate of the sand (Andy Chadwick et al., 2008; Zweigel et al., 2004).

The permeability was measured in four 1.5 inch cores on different length (table 2.2) and weighted by the core size differences (Zweigel et al., 2004). There was significant variation in the measurements, with values ranging from 1 to 8 Darcy's, but the samples could be estimated to have an average permeability of around 2D (Zweigel et al., 2004). There is no significant difference between vertical and horizontal permeability, and the permeability may appear low compared to the high porosity measurements. This may be explained by the lack of intermediate grain sizes, in the case that the larger grains constitute the high porosity, while the smaller grains block the pore throats and hence reducing the permeability (Zweigel et al., 2004).

Core	Length (m)	Permeability (mD)	Weight factor
Vertical	1.15	1845	0.7930
Vertical	0.10	3252	0.0690
Horizontal	0.10	2550	0.0690
Horizontal	0.10	1621	0.0690
Weighted average and standard deviation:		1975 ± 418	

Table 2.2: Showing the measured permeability obtained from the cores obtained over the injection formation, in both horizontal vertical directions. The values are weighted by their relatively core sizes. From (Zweigel, Arts, Lothe, & Lindeberg, 2004)

The heterogeneity of the Utsira formation is interpreted to be very good in the upper sand package between the big shale and the top Utsira, whereas it is interpreted to be somewhat lower in the main reservoir, due to the small intra-reservoir shale layers interrupting the sand (Zweigel et al., 2004)

Only one temperature measurement in the shallow Utsira sand exists, and it is 37°C at 1038m bsl (Zweigel et al., 2004). For a water depth of around 80m and a seabed temperature assumed to be 4.8°C, the geothermal gradient can be calculated to have the value 33°C/km, which gives a reservoir temperature in the range 28°C and 41°C at the reservoir top and base, respectively (figure 2.10) (Zweigel et al., 2004). Since there is no evidence for overpressure in the formation (measurements from the well-head), the hydrostatic pressure gradient can be used for fluid pressure, which was calculated based on tabulated pressure and temperature-dependent density data from brine containing 3.5% salt, and gives a reservoir pressure in the range 80 to 110 bar (figure 2.10) (Zweigel et al., 2004). The density of the injected CO_2 is dependent on the pressure, temperature and the amount of impurities (some methane and butenes is included in the mix for flow purposes), and is expected to be stored in the formation as a supercritical fluid with a density around 700 kg/m^3 (figure 2.10a) (Eiken et al., 2011; Zweigel et al., 2004). The injected CO_2 in Utsira formation cools down after being injected, as observed in figure 2.10b (Eiken et al., 2011).

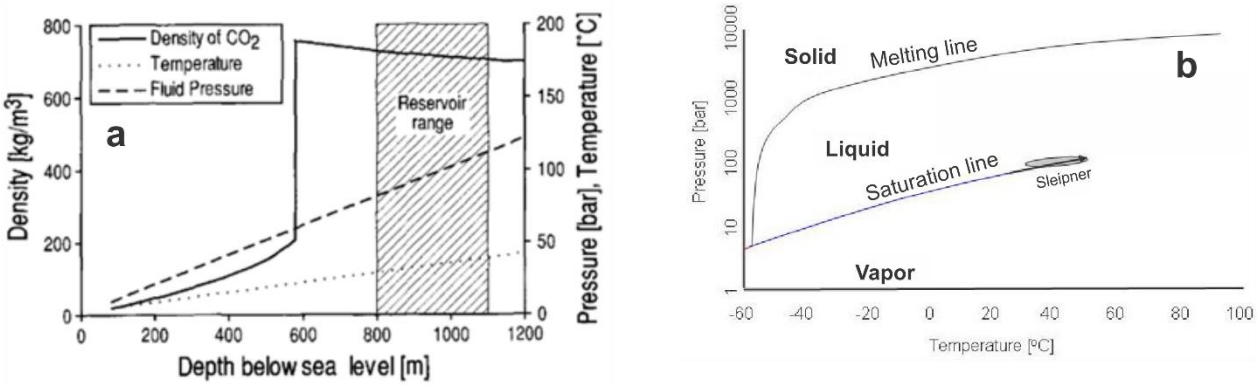

Figure 2.10: a) Combined graph for the temperature, fluid pressure and CO_2 density as function of depth in the Sleipner site. The Utsira reservoir range can be observed inside the shaded box. From (Zweigel et al., 2004). b) Phase diagram for pure CO_2 as a function of pressure and temperature, with well-head and bottom-hole situations for Sleipner shown with arrow, and reservoir conditions showed in shaded areas. It can be observed that at the injected CO_2 at Sleipner cools down in the reservoir. Modified from (Eiken et al., 2011)

2.2.4 Storage capacity

Assessment of the total reservoir storage potential is required to devise a long-term injection strategy as mentioned in the introduction. If the whole formation volume is considered with the average reservoir properties, the maximum storage capacity for Utsira storage formation is calculated to be approximately 6 x 10^{11} m^3 (R. A. Chadwick et al., 2004a). For a reservoir with relatively low structural relief such as the Utsira reservoir, the total pore volume of the reservoir cannot necessarily be utilized. A more realistic measurement of its storage capacity would have to only include the possible storing within the pores at the structural traps close to the predicted migration distance of the CO_2 (R. A. Chadwick et al., 2004a). This storage capacity is calculated and expected to be approximately 6.6 x $10^8 m^3$, which is roughly 20 times more than the planned injection volume of approximately 3 x $10^7 m^3$ (Andy Chadwick et al., 2008; R. A. Chadwick et al., 2004a).

In addition, the CO_2 can be expected to migrate and accumulate beneath the intra-reservoir shales to increase the storage capacity by allowing a larger amount of CO_2 to dissolute and be mineral trapped in the vertical extent (R. A. Chadwick et al., 2004a; Torp & Gale, 2004).

2.2.5 Why the Utsira formation was chosen as CO_2 injection site

When it was decided that the extracted CO_2 from the natural gas should be injected into the subsurface rather than being vented into the atmosphere there was several alternatives on where to do it, including the Utsira formation (Andy Chadwick et al., 2008; Korbol & Kaddour, 1995). These were mostly rejected on the basis of incompatibility. Some of the other alternatives were:

- To use the CO_2 for enhanced oil recovery (EOR) in nearby oil/gas fields. Here the amount of extracted CO_2 must match the amount needed for EOR, which was decided to be too unpredictable.
- Inject CO_2 into the Sleipner East gas/condensate field (Heimdal Formation) for enhanced gas recovery. For this alternative, there was a threat that the injected CO_2 may contaminate the produced gas.
- Injection into the Skagerrak Formation at about 2500m depth. This lies close to the Sleipner East gas/condensate reservoir, and therefore it may be a risk of contamination of the products.

For these reasons, the Utsira formation was chosen to be the storage formation. Even though the storage in Utsira formation is not optimal, due to the possible lost vision of the underlying gas/condensate reservoirs when the CO_2 is stored above and the relatively low relief of the main CO_2 trap (Andy Chadwick et al., 2008). Although this chapter explained that the Utsira storage formation possesses good reservoir conditions that are suitable for injection of CO_2, and with a relatively good storage security.

2.3 Injection rate and monitoring of injected CO_2 at the Sleipner facility

As explained in chapter 1.3.6, the main monitoring tool at the Sleipner CO_2 injection site is the seismic acquisition (4D seismic time-lapse); though there have been several other tools and techniques acquired over the injection site. Other tools that have been acquired are the wellhead pressure and flow rate (continuous), sampling of the gas composition intermittently, gravimetrical repeated surveys, electromagnetic surveys, and seabed surveys (Eiken et al., 2011; Hagen, 2012) (figure 2.11).

As mentioned in the beginning of this chapter, the injection rate has approximately been 0.9M tons CO_2 each year, such that the Utsira formation contained 4.25Mt injected CO_2 by 2001, 6.85Mt CO_2 by 2004 and 8.5Mt CO_2 by 2006 (years of which is interpreted in this thesis).

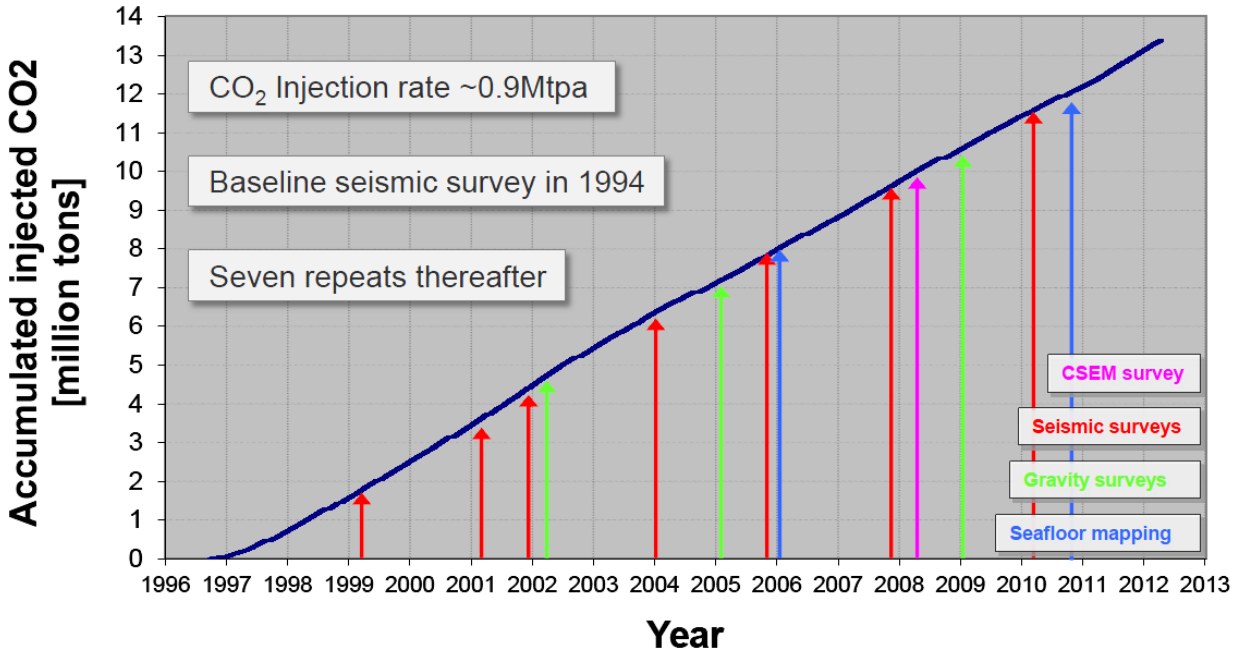

Figure 2.11: Showing the accumulated injection of CO_2 over the years from the injection started (1996) and to 2012. It can also be seen the different monitoring techniques obtained over the injection time. It is not marked the acquisition of the pre-injection baseline survey which was acquired two years before the injection started (1994). From (Hagen, 2012)

The reason why the use of seismic tools for monitoring the injection of CO_2 in an underground storage formation is important is that it produces good reflections even when the accumulation is low. This is especially seen on the Sleipner injection site. Even with the CO_2 in a supercritical, rather than a gaseous, state it has been shown that CO_2 accumulations with a thickness as low as about a meter can be detected – far below the conventional seismic resolution limit (which are approximately 7m in this case) (S. Holloway, 2004).

3. Data and methods

3.1 Datasets

For this thesis, multiple conventional 4D seismic datasets provided by Statoil obtained from the Sleipner CO_2 storage facility have been interpreted. The seismic datasets used was acquired in 1994 (baseline (i.e. pre-injection)), 2001, 2004 and 2006, which all was processed in 2007. Since the seismic datasets have been processed equally they cover the same area and have the same inline and crossline coordinates, which is covering an area of 5.8km (inline) x 3.1km (crossline) = 18km^2, and situated in the North Sea about 250km from the west coast of Norway – close to the UK boarder (Torp & Gale, 2004) (figure 3.1) as explained in chapter 2.

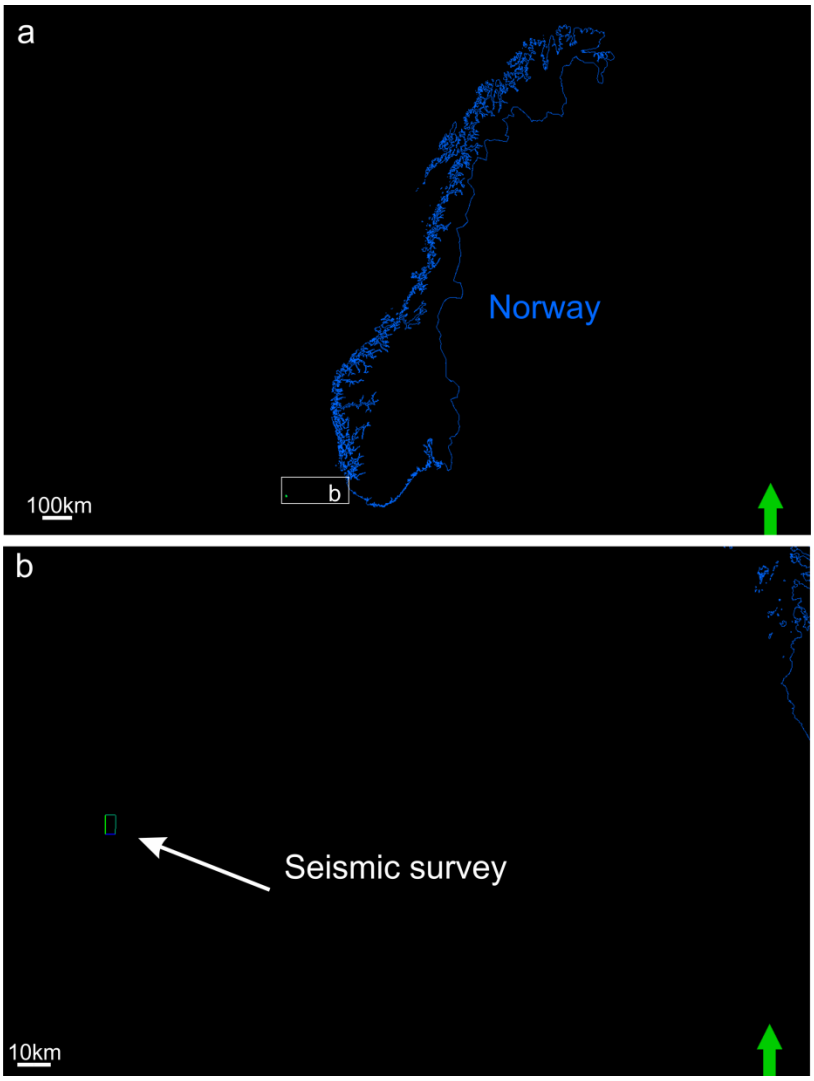

Figure 3.1: Location of the seismic datasets used in this thesis. Green arrow is pointing towards north

The key 3D acquisition parameters for the surveys used in this thesis can be seen in table 3.1 under. The baseline survey was shot in 1994, although the acquisition parameters were focused on a deeper target than the location for the CO_2 injection. The later time-lapse had acquisition geometries that were tried balancing between keeping the same as the one shot in 1994 and to try to focusing more on the injection location. The dataset obtained from 2001 and 2006 show good repeatability and, in contrast, the 2004 dataset was acquired almost perpendicular to the earlier datasets. The use of the 2004 seismic dataset have proven to be rather difficult, especially when using subtraction of datasets. Therefore, the 2004 dataset is at certain time omitted when used for comparison (especially when interpreting the leakage possibilities). Info from (Andy Chadwick et al., 2008).

Survey	ST9407	ST0106	ST0403	ST0607
Date acquired	6.8 - 10.9 1994	27.9 – 1.10 2001	13.6 - 13.8 2004	June 2006
Vessel	Seisranger	Geco Diamond	CGG Alize	Ramform Explorer
Shooting direction	0.853 degrees	0.850 degrees	90.00 degrees	0.850 degrees
Source tow depth	6m	6m	6m	6m
Source length	16m	15m	14.8m	15m
Source width	20m	10m	24m	16m
No. of subarrays	3	2	4	3
Source x-line sep.	50m	50m	n.a	50m
Source volume	3400 in^3	3390 in^3	4280 in^3	3660 in^3
No. of sources	2	2	1	2
Shotpoint interval	18.75m	12.5m	18.75m	18.75m
Streamer type	Nessie III	Nessie IV	Syntrak	PGS RD H / Teledyne
No. of cables	5	6 (on 4 str preplot)	10	8 (on 6 str preplot)
Cable separation	100m	100m	37.5m	100m
Cable length	3000m	1500m (3000m)	4500m	3600m
Near offset	195m	150m	77m	130m
Group interval	12.5m	12.5m	12.5m	12.5m
Group length	16.10m	14.86m	12.5m	12.5m
Tow depth	8m	8m	8m	8m
Bin-size acq.	6.25 x 25m	6.25 x 25m	6.25 x 18.75m	6.25 x 25m
Record length	5500 ms	4500 ms	6000 ms	6000 ms
Sample interval	2 ms	2 ms	2 ms	2 ms
Low cut filter	3.4 Hz / 18 dB/Oct	3 Hz / 18 dB/Oct	3.4 Hz / 12 dB/Oct	3 Hz / 12 dB/Oct
High cut filter	180 Hz / 70 dB/Oct	200 Hz / 406 dB/Oct	206 Hz / 276 dB/Oct	206 Hz / 276 dB/Oct

Table 3.1: Key acquisition parameters for the Sleipner time-lapse seismic datasets (1994 – baseline, 2001, 2004 and 2006. The table is modified from (Andy Chadwick et al., 2008))

3.2 Seismic reflection theory

The seismic lines illustrates the underground geophysical structures by creating seismic waves from artificial sources, where they travel down to a reflective layer and is reflected back where the arrival time can be measured. A reflective layer is defined by their acoustic properties (i.e. density and velocity (equation 3.1)) and is called acoustic impedance. The seismic wave will partially be reflected back if there are changes in the acoustic impedance at the interference between two mediums when traveling through the underground, and the amount of energy being reflected back is dependent on the weighted change of the acoustic properties from the interface of the mediums, hence reflection coefficient (equation 3.2). The seismic reflection coefficient lies in the range -1 to 1, and has a positive value if the upper medium has lower acoustic impedance compared to the lower medium, and has a negative value if the upper medium has greater acoustic impedance compared to the lower medium, and is zero if both mediums have the same acoustic impedance. It is also important to know the difference between a seismic reflection and a seismic reflector, where the seismic reflection is the actual event when the wave is being reflected back, and the seismic reflector is the boundary/interface between the two mediums where the reflection is occurring. All info from (Andreassen, 2009).

$$Z = \rho V \tag{3.1}$$

Equation 3.1: A mediums acoustic impedance (Z) equals the product of its acoustic velocity (V) and density (ρ)

$$R = \frac{(Z_2 - Z_1)}{(Z_2 + Z_1)} = \frac{(\rho_2 V_2 - \rho_1 V_1)}{(\rho_2 V_2 + \rho_1 V_1)} \tag{3.2}$$

Equation 3.2: The strength of a reflection generated at an interface between two mediums can be quantified in the terms of the boundaries reflection coefficient (R), where Z_1, ρ_1 and V_1 are respectively acoustic impedance, density and velocity in the upper medium, and Z_2, ρ_2 and V_2 are respectively acoustic impedance, density and velocity in the lower medium. From the equation it can be seen that R will take a positive value when $Z_2 > Z_1$, negative value when $Z_1 > Z_2$, or be zero if $Z_2 = Z_1$.

3.3 Seismic resolution

Seismic resolution is the ability to separate two features that are close together. The minimum separation of two bodies before their individual identities is lost on the resultant map. All info from (Andreassen, 2009).

3.3.1 Horizontal resolution

The horizontal resolution is the minimum horizontal distance between two mediums boarder, and it is given by the Fresnel Zone (equation 3.3). Because the seismic wave traveling from the energy source have a spherical waveform, it affects a considerable area of the reflector surface. The zone is generated by the fact that the portion of the reflector from which energy returns to the hydrophone (or geophone) within a half-cycle after the onset of the reflection (figure 3.2).

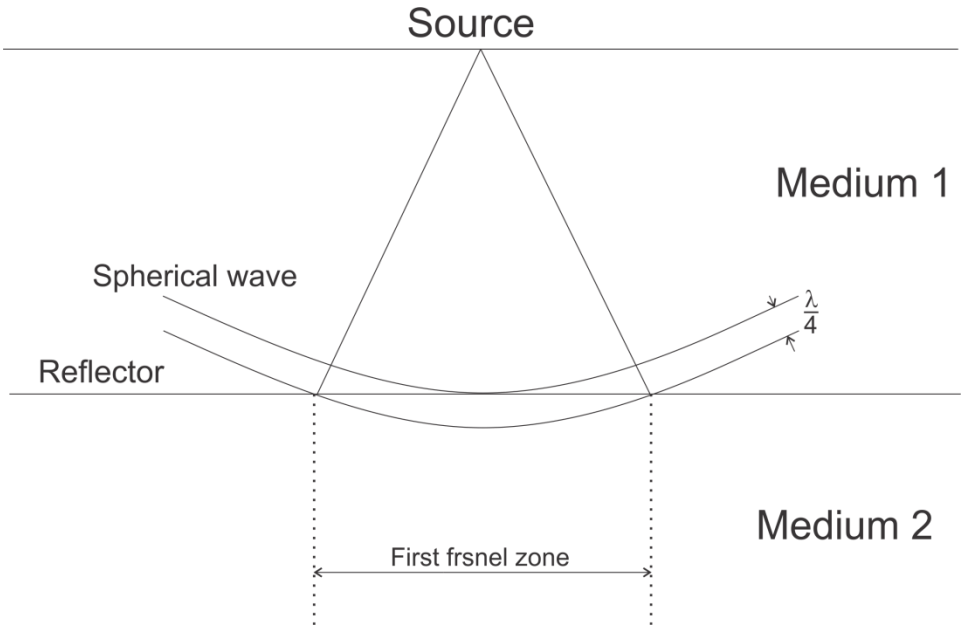

Figure 3.2: The first Fresnel Zone. The first energy to reach from a plane reflector is from the point where the reflector is first tangent to the wave front. The area of the reflector that produces the reflection is limited by the area that the wave front one-quarter wavelength later makes with the reflector.

$$rf = \frac{V}{2}\left(\frac{t}{f}\right)^{\frac{1}{2}} \tag{3.3}$$

Equation 3.3: Magnitude of the Fresnel Zone. Where rf is the radius of the Fresnel Zone, V is the average velocity, t is the two-way travel time in seconds, and f is the dominant frequency in hertz. As it can be seen from the equation, the Fresnel Zone will increase with depth, increasing velocity, and lower frequencies.

The horizontal resolution is prominent improved in the 3D seismic data compared to the 2D seismic data in two important aspects. Firstly, the grid space is reduced from kilometers in the 2D seismic profiling, to only 25m or less for 3D seismic surveys. Secondly, sampling and advanced migration algorithms allows accurately positioning of reflections in all directions, and thus collapsing the Fresnel Zone that will only be a minor circle compared to the 2D ellipse (figure 3.3).

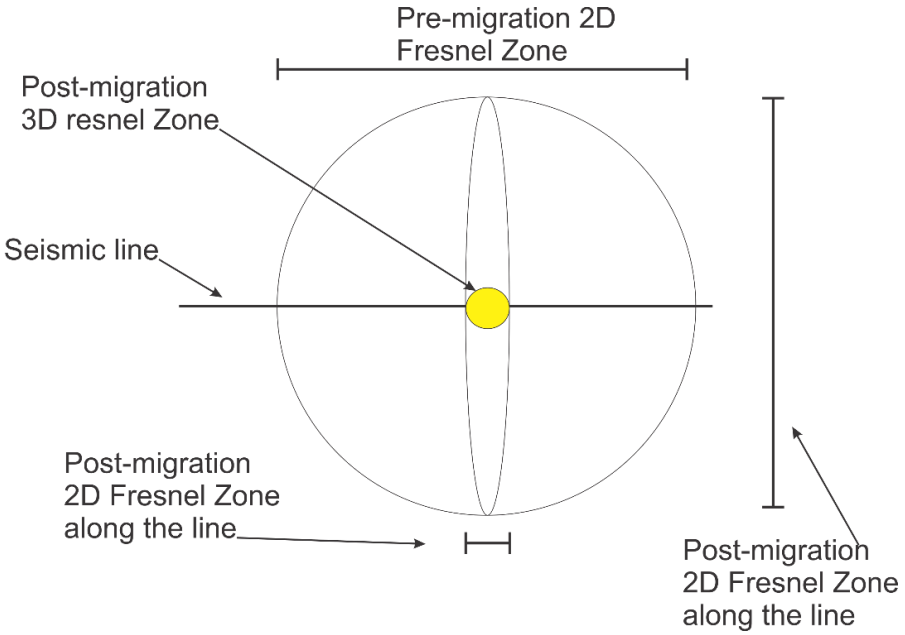

Figure 3.3: Illustrating the effect of 3D migration compared to 2D migration. The large circle represents the Fresnel Zone before migration, the ellipse represent the 2D migrated Fresnel Zone, and the yellow circle represents the 3D migrated Fresnel Zone. The figure is modified from (Andreassen, 2009).

3.3.2 Vertical resolution

This is the minimum vertical thickness of a medium in order for the seismic wave to detect the medium. It is usually taken as λ/4, where λ is the dominant wavelength of the seismic signal. In order to obtain good resolution in the subsurface geometry, it is desirable to have seismic sources that generated waves with short wavelengths (high frequency) or investigate in medium with low acoustic velocity (although the latter one cannot be mechanical changed) (equation 3.4). One should also bear in mind that high frequency seismic surveys are will not produce good quality images for deep underground structures due to the high attenuation rate experienced of the signal. It is therefore it used sources with low frequency (high wavelength) to image structure deep in the subsurface, which do not attenuate as fast but also have higher vertical resolution limits.

$$\lambda = \frac{V}{f} \tag{3.4}$$

Equation 3.4: The relationship between frequency (f), acoustic velocity (V) and wavelength (λ).

3.4 Petrel

The results in this thesis are based on the interpretation of 4D seismic data using Schlumberger's Interpretation and Visualization platform Petrel.

3.4.1 Interpretation

The use of Petrel offers good ways to work on the 3D datasets in way of navigate and visualize the subsurface. The 3D datasets can be seen as many seismic waves that are correlated with each other and making it possible to see the underground structures in a 3D view, where the reflections can be followed and interpreted. There are four basic methods for interpreting a horizon in Petrel; *Manuel interpretation* (where one need to follow the same reflection throughout the dataset), *Guided autotracking* (where one selects two points on a specific reflection, and Petrel will track the best route between these points), *Seeded 2D autotracking* (where one identifies the wanted reflection, and Petrel will track the reflection until it becomes discontinuous through the interpretation window), and *seeded 3D tracking* (where one identifies the wanted reflection, and Petrel will try to follow that reflection throughout the 3D dataset). I this thesis there was used seeded 2D autotracking on reflections which was continuous and prominent (like the seabed reflection), and manual interpretation in deeper structure where the reflections was locally discontinuous.

In order to interpret horizons one has to choose on whether to track on a seismic peak, through or zero crossing (figure 3.4), and to be consisted with ones choice. In this thesis there was chosen to track and interpreted on seismic peak and through with the best continuity, and weather the reflection coefficient (R) was expected to be positive or negative (from well-logs).

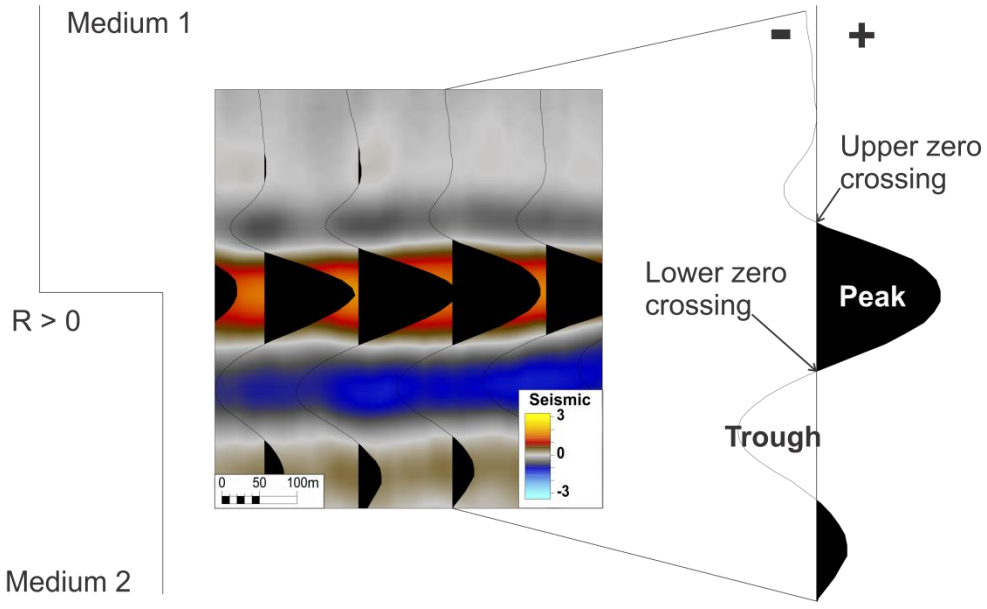

Figure 3.4: Left: Showing the acoustic impedance chance on an interface with positive reflection coefficient. Middle: Seismic trace over the interface, where it can be seen how the colors changes for impedance contrast. Right: One of the wavelets from (middle) where the different tracking options are indicated.

3.4.2 Visualization tools and functions

The horizon interpreted from the seismic survey can be further worked on in order to best visualize the areas of interest. Often the interpreted seismic horizon is made a surface of, which visualize the reflector as a continuous layer that can be displayed in both 2D and 3D view. After the surface has been generated, many different attribute options and actions can be applied. Under is a list of surface and volume attributes that have been applied in the thesis. All info from (Schlumberger, 2011).

RMS amplitude / Minimum amplitude:

Is the square root of the sum of the squared amplitudes, divided by the number of live samples as shown in equation 3.5, and can give direct indications to hydrocarbon indicators in the data and other features that have an amplitude response (RMS). Measuring the reflectivity within a time or depth window, and is the maximum negative number in the window and is used to detect negative direct hydrocarbon indicators such as bright spots (Minimum amplitude).

$$RMS = \sqrt{\frac{\sum_i^n amp^2}{k}} \tag{3.5}$$

Equation 3.5: RMS amplitude formula, where k is the number of live samples

Isochron thickness map:

Defined as the time difference between two horizons, and is measured in the units of the input horizons.

Chaos:

Maps the "chaoticness" of the local seismic signal within a 3D window, and measures how consistent the seismic reflection is. In other word the attribute will map out any discontinuity of the seismic reflections, and is especially great at mapping out faults/discontinuities, reef texture, channel infill etc.

Smoothing:

This attribute will increase the signal to noise ration by making the reflection data more continuous. It will generate seismic images more comforting to interpret, but details in the seismic data may also be lost.

Envelope:

This attribute is also known as reflection strength, instantaneous energy, and magnitude, is defined as the total energy of the seismic trace. It is of importance detecting bright spots caused by gas accumulation, detecting lithological changes that are caused by strong energy reflection and sequence boundaries.

Seismic calculator:

This is a powerful tool where it can be generated new versions of seismic either via the pre-defined standard functions or by user-defined formulas. The calculator is used for generating virtual calculation volumes based on already existing cubes or between two more existing cubes. The calculator becomes especially useful for interpreting 4D seismic data, where it makes it possible to generate cubes of the changes.

Multivolume comparison:

The Multi-volume Comparison plug-in offers a visually-rich solution for the seismic vintages comparison inside Petrel. The main objective for the plug-in is to provide an easy way of putting together one or more seismic cubes and Flip, Blend and Roll them, visualizing the comparison on intersecting lines. This plug-in will make the QC step quicker and easier for the Petrel user. (From (Schlumberger, 2014))

4. Results

The results presented in this chapter have been drawn from the interpretation of four 3D seismic datasets that have been acquired over the injection site. The seismic cubes are covering the same surface area, such that the seismic injection is occurring near the center of the seismic cubes (figure 4.1).

The figures created in this chapter are all generated in the time domain, and includes scale bars, color bars and the year of when the survey was acquired. The 2D and 3D data include a green arrow that is pointing towards north (figure 4.1)

The seismic sections shown in this chapter are mostly inlines, which have an N-S direction, with north in the right corner and south in the left corner.

For time-depth conversions there have been used a velocity of approximately 2050 m/s in the reservoir containing formation saline fluid, whereas there have been used a velocity of approximately 1450 m/s in the reservoir containing injected CO_2 (F. C. Boait et al., 2012). There will in reality be some small differences in these values when moving shallower or deeper in the reservoir, but for convenient there is only used approximately values. For the other parameters used regarding calculations and interpretations there have been used the ones presented in the paper (Akervoll et al., 2009) (table 4.1).

In the following, there will be presented the results obtained from interpretation, which includes the outline of the cube, the interpretations of the various horizons from the 1994 baseline survey, the detection of the injected CO_2, and how the CO_2 changes with time. The features observed on the seismic data that have occurred prior or during the injection are presented, and it will be presented a short assessment on the safety around the injection site.

Parameter	
Density of brine, g/l	1.019
Viscosity of brine, mPas	0.772
Solubility of CO_2 in Utsira brine, mmole fraction	20.328
Density of CO_2 saturated brine, g/l	1.028
Viscosity of CO_2 saturated brine, mPas	0.852
Formation volume factor of CO_2 saturated brine (28.2 Sm^3 CO_2/Sm^3 brine)	1.043
Density of CO_2, g/l	0.667
Viscosity of CO_2, mPas	0.051

Table 2: Properties of Utsira saline water and CO_2 at 31.5 °C and 80bar (reservoir conditions). From (Akervoll, Lindeberg, & Lackner, 2009)

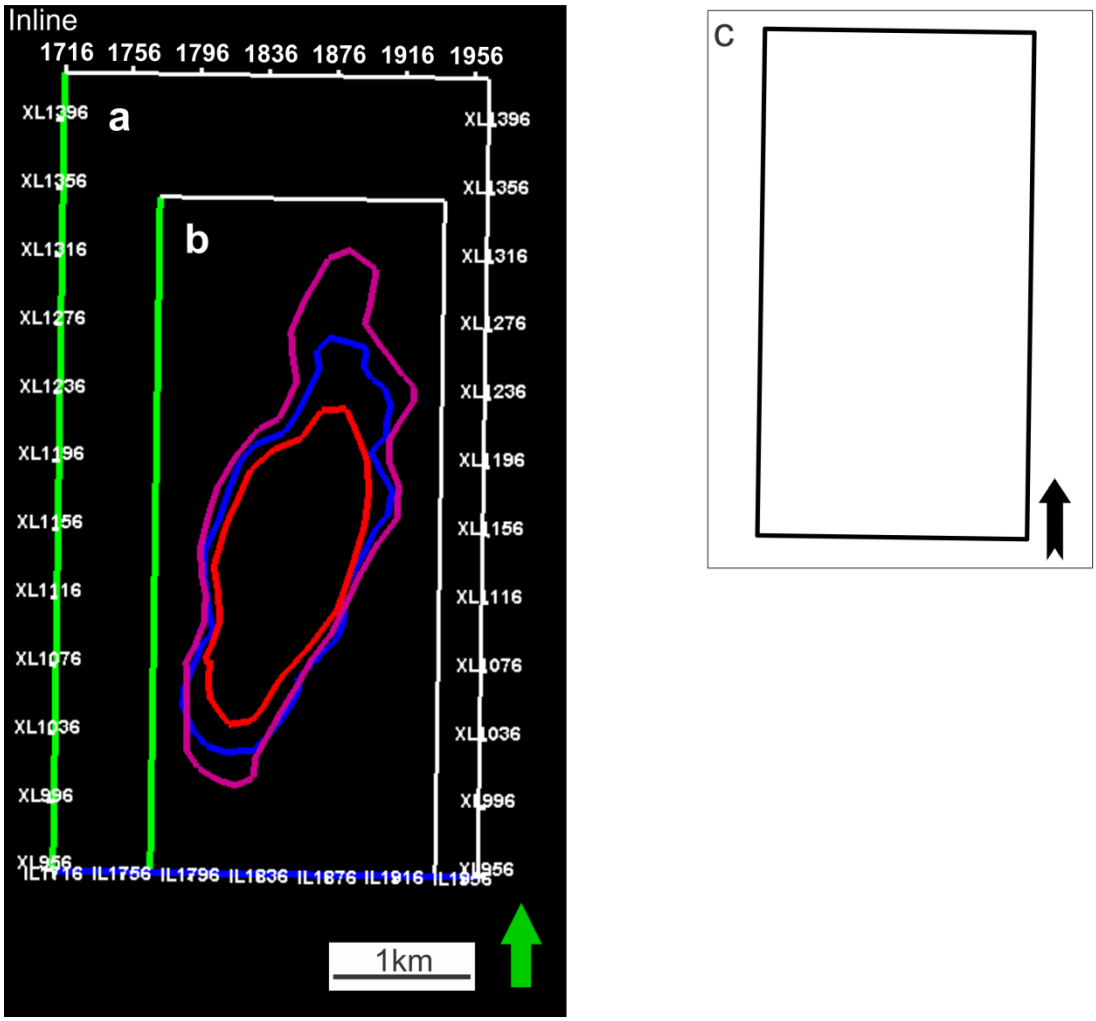

Figure 4.1: Helping figures. a) 2D overview over the whole interpreted cube with marked inlines and crosslines. 2D figures that have been interpreted using this outline are figures 4.4, 4.5, 4.6ba, 4.7, 4.14, 4.21 and 5.4c. b) In order to focus more directly on the CO_2 plume there was created a seismic cropped cube. 2D figures that have been interpreted over this outline are figures 4.10b, 4.19 and 4.22b&c. The green arrow represents north direction, and the colored polygons are taken from the lateral spread of the CO_2 plume in 2001 (red), 2004 (blue) and 2006 (purple). c) Outline of the same area as for (a), which will be used for indicating the locations of obtained seismic sections.

4.1 Outline of the 1994 pre-injection cube

The 1994 pre-injection cube was acquired two year before the CO_2 injection began, and its outline can be seen in figure 4.2. The seismic cube includes the five interpreted horizons and the four main sediment packages. The baseline survey includes all the pre-injection reservoir geometries, and is particularly important to use when interpreting changes caused by injection of CO_2.

The seismic dataset consist of four main sediment packages, which are described more detailed in chapter 2. The uppermost package, the Nordland Group, is covering the whole area from the seabed reflection and down to the top of the storage formation. The package include all the three sealing units described in chapter 2.

The next sediment package is the semi-separated sand-package or "sand wedge" representing the uppermost part of the storage formation, which is located in the vertical area between the Utsira top reflection and down approximately 10-15m to another bright reflection. This package will in the thesis be referred to as "(upper) sand package in the Utsira storage reservoir". The upper sand package is separated from the main reservoir by a relatively thick shale layer (5-6m). Several published works tend to separate the Utsira formation based on the thick shale, where the upper sand package is thought to be part of the overlying Nordland Group (Zweigel et al., 2004). The upper sand package will, however, be interpreted as part of the Utsira formation in this thesis.

The next sediment package is the rest of the storage reservoir, which is located between the thick shale and the formation base. The vertical displacement of the package is in the range 150 – 250m in the survey area, and will in this thesis be referred to as "the main Utsira (storage) reservoir". The sedimentology of the package can be found in chapter 2. The only main important aspects of this sediment package are its high permeability and porosity, and that is consists of small intra-reservoir shale layers stacked upon each other. The shales and the sand layers can be observed on the well logs where they are indicated to have thicknesses of between 10 and 40m and 1-2m, respectively (F. C. Boait et al., 2012).

The Utsira formation is in reality included in the Nordland Group, where the lower Utsira sequence boundary (sometimes referred to as mid-Miocene unconformity, as seen in chapter 2) is the litostratigraphic boundary between the Nordland Group and the underlying Hordaland Group (Galloway, 2002).

The deepest main sediment package on the seismic data is the underlying Hordaland shales from the Hordaland Group. This sediment package have a generally complex form with high local relief in the upper part close to the Utsira base reflector, but seem to have several parallel and almost flat reflectors in the shallower area.

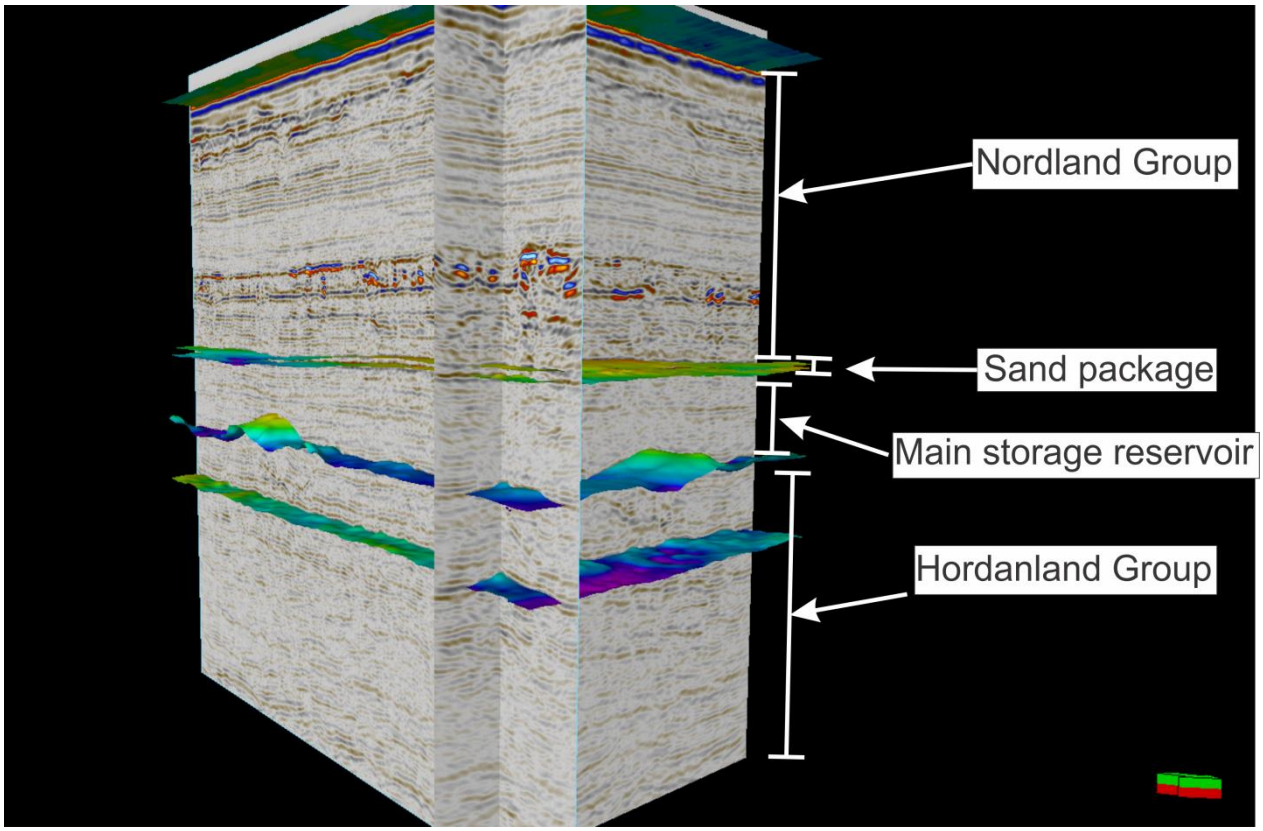

Figure 4.2: Illustrating the 1994 seismic survey with the inline 1845 and crossline 2324 meet, where the main sediment units pointed out, with the Nordland Group in the top, sand package in the upper part of the Utsira storage reservoir separated by a relatively thick shale layer, the main Utsira storage reservoir, and the underlying Hordaland Group. It also includes the five interpreted horizons.

4.2 Interpreted horizons

There have been interpreted five different horizons from the pre-injection cube that will be used in this thesis (figure 4.2). Each of the horizons serves its own purpose, and the amount each horizon will be used will differ and is explained under the interpretation of the individual ones. The five horizons that are interpreted in this thesis are the seabed, Utsira top, the thick shale, Utsira base and Intra-Hordaland.

The interpreted horizons can be seen in figure 4.3 under, where they are indicated on the seismic inline 1928 obtained from the baseline dataset. From the figure it can be observed how the horizons is situated relatively to each other (in time), and the different reflection pattern for the individual ones. In general, it can be observed that the four horizons 1, 2, 3, and 5 are quite flat, whereas horizon 4 is observed to have much more depth variations.

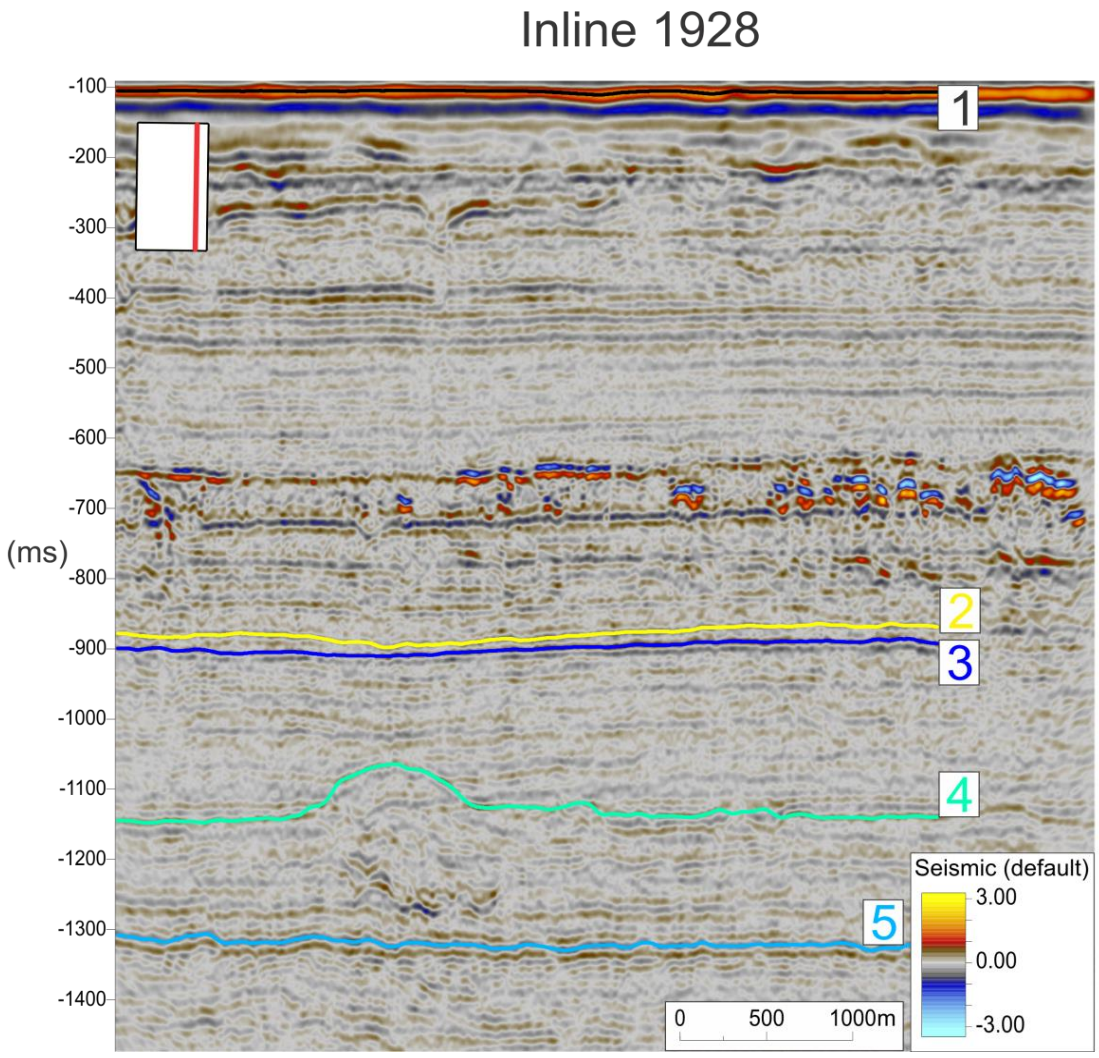

Figure 4.3: Seismic inline 1928 obtained from the 1994 seismic dataset. The figure include all the five interpreted horizons. The five interpreted horizons are the Seabed (1), Utsira top (2), Thick shale close to Utsira top (3), Utsira base (4), and Intra-Hordaland (5).

4.2.1 Utsira top horizon

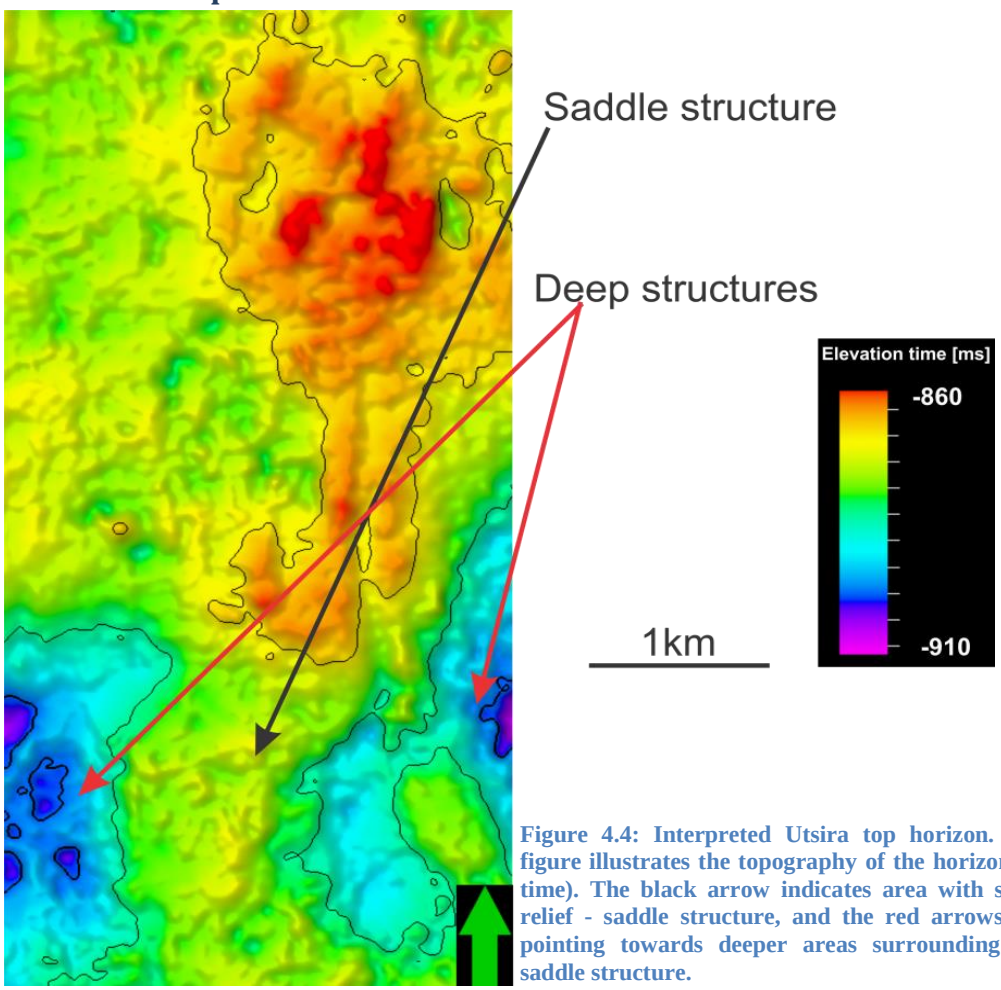

Figure 4.4: Interpreted Utsira top horizon. The figure illustrates the topography of the horizon (in time). The black arrow indicates area with short relief - saddle structure, and the red arrows are pointing towards deeper areas surrounding the saddle structure.

The top Utsira horizon was observed and chosen due to its negative peak reflection (figure 4.3), and interpreted to be the top of the storage formation based on information from well logs. The depth of the formation are ranging between approximately 860ms and 910ms in the survey area. The horizon is observed to have a ridge-like topography with its shallowest point in the northeast corner, and a saddle-like structure surrounded by deeper structures in the south. The saddle structure observed in the southern part on the horizon is approximately 1km wide.

This horizon is the shallowest part where the CO_2 is expected to migrate (Andy Chadwick et al., 2008), and it is possible that the CO_2 that reach this level will tend to accumulate under the topographical highs on the horizon. This interpretation have been done based on the assumption that the injected CO_2 will migrate upwards the formation due to buoyancy flow and hence flow towards the shallowest parts of the overlying topography. The structure of this horizon may therefore indicate migration routes. It will be widely used throughout the thesis.

4.2.2 Thick shale horizon

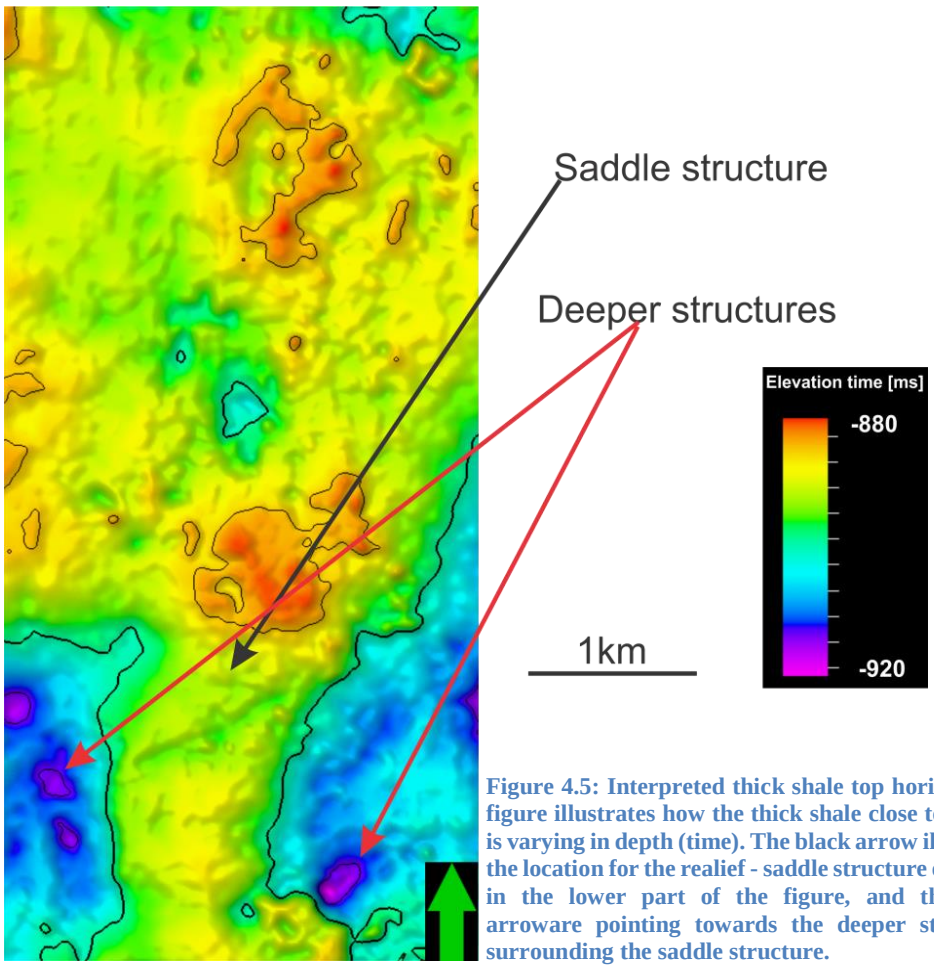

Figure 4.5: Interpreted thick shale top horizon. The figure illustrates how the thick shale close to the top is varying in depth (time). The black arrow illustrates the location for the realief - saddle structure observed in the lower part of the figure, and the black arroware pointing towards the deeper structures surrounding the saddle structure.

Approximately 15 – 20ms below the interpreted Top Utsira horizon there can be observed a positive peak amplitude reflection (figure 4.3). The reflection is interpreted to be produced by the interface between the upper sand package situated under the Utsira top, and the thick shale layer of approximately 5m. The shale layer can be seen on both the well logs from chapter 2, where it creates a section with relatively high gamma values (figure 2.7), and on the seismic dataset. On the seismic dataset, it can be followed as a continuous reflection with depth ranging between approximately 880ms and 920ms.

The horizon is very much alike the reflection at the Utsira top (figure 4.4), where it can be seen the same saddle-like structure with the deeper structures at the sides (figure 4.5). The only difference is that this saddle structure seems to be a bit narrower, and that the variation in depth between the deepest and shallowest point are not as great as it is for the Utsira top horizon.

In addition, this topography may also indicate possible migration routes for the injected CO_2 if the CO_2 accumulates under the shale. Because it is interpreted to be a continuous reflection from a 5m shale layer, it may act as a sealing unit preventing further upward migration of the injected CO_2. The horizon will be widely used throughout the thesis.

4.2.3 Utsira base horizon

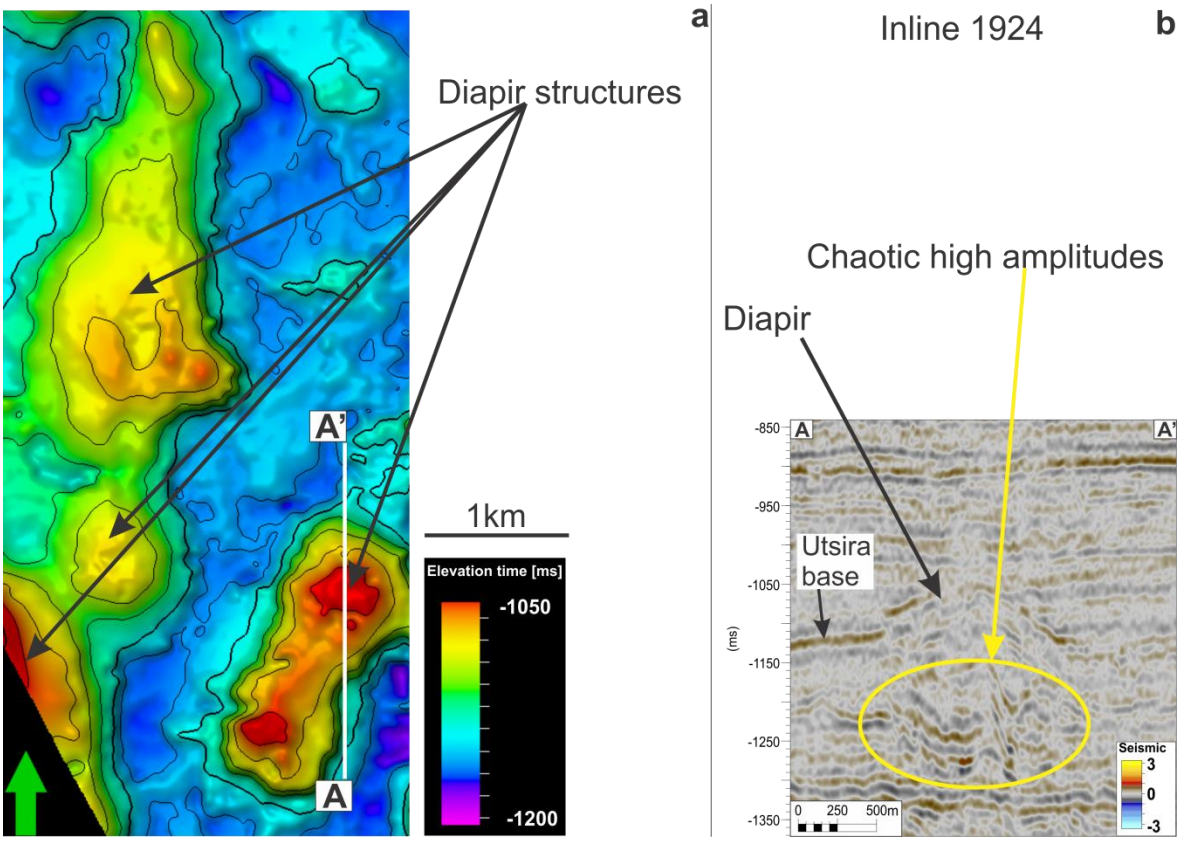

Figure 4.6: a) Interpreted Utsira base horizon. The figure illustrates the depth variations (in time) of the Utsira base horizon, where the black arrows are pointing towards observed relief – diapir structures. b) Seismic inline 1924 which are taken over the marked area shown in (a), where it can be seen a relief of approximately 100ms due to the diapir structure marked with the black arrow. The yellow arrow whit its yellow circle is indicating a chaotic reflection pattern underneath the diapir structure.

At a depth of approximately 1100ms it was observed a relatively continuous seismic reflection with a positive reflection amplitude (figure 4.3). The reflector producing this reflection was interpreted to be caused by the interface between the Utsira reservoir sandstone and the underlying Hordaland shales. This reflector is called Utsira base horizon. The interpretation was based on the observations from the well logs from chapter 2 (figure 2.7). The Utsira base horizon is observed to have a depth variation between 1050ms and 1200ms on the baseline seismic dataset (figure 4.6a).

Since the underlying Hordaland shales was interpreted to have been experiencing severe mud-mobilization at the time when the Utsira sand was deposited, the local structures observed with shallow relief was interpreted to be dome/diapir structures created by the mud mobilization (Galloway, 2002; Gregersen et al., 1997). The interpretation is supported by the observed high amplitude anomalies beneath these dome structures, which often is associated with mud mobilization (figure 4.6b) (Loseth et al., 2009). Because of these local variations in depth, the interpretation of the Utsira base reflection was locally difficult to map out. The horizon will be widely used throughout the thesis.

4.2.4 Seabed and Intra-Hordaland horizons

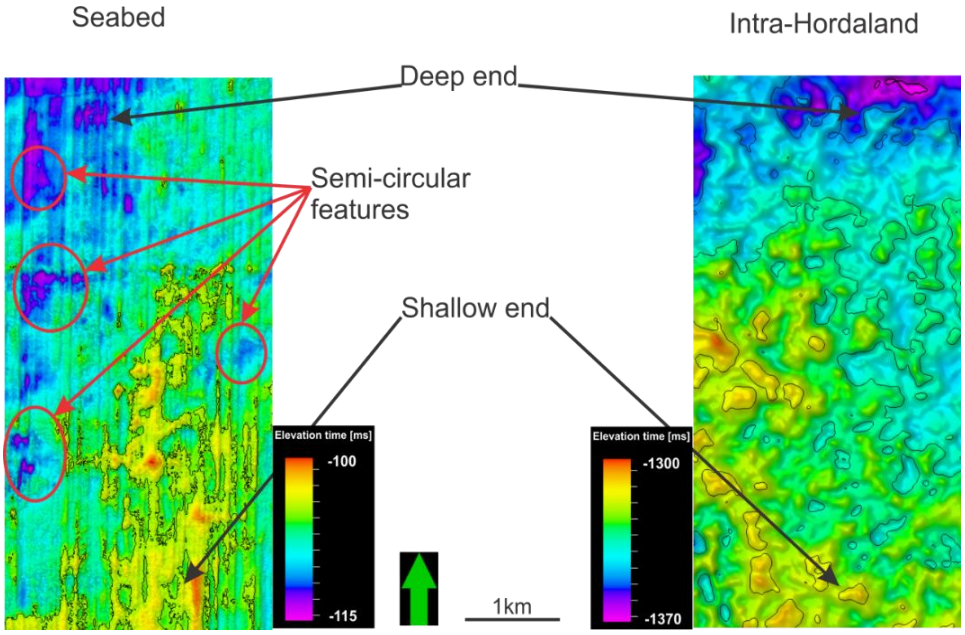

Figure 4.7: Interpreted Seabed (left) and Intra-Hordaland (right) horizons. The red arrows are pointing towards observed semi-circular features on the seabed horizon. The black arrows are pointing towards the shallow and deep end of the horizon at the south and north location, respectively

At a depth of approximately 110ms there could be observed a bright reflection with positive reflection coefficient (figure 4.3). The reflection was interpreted to be caused by the interface between the seawater and the seabed sediments, where the bright reflection is caused by the relatively large differences in acoustic impedance between the two mediums (Andreassen, 2009). The seabed is observed to have a depth variation between 100ms and 115ms over the dataset (figure 4.7 left). The Seabed horizon was chosen to be interpreted in order to detect changes at shallow areas as CO_2 is being injected in underlying strata. From the baseline dataset there can be indicated areas with semi-circular depressions on the seabed horizons. These depressions may be indication of pockmarks (Loseth et al., 2009), but due to its very short relief (in the range 5-10m) they are rather interpreted to be small displacements of the seabed surface, and may even be overestimated due to the signal noise (the lines observed in the N-S direction is interpreted to be noise caused by seismic acquisition (Andreassen, 2009)).

Within the Hordaland Group there could be observed a relatively flat and continuous negative reflection at a depth of around 1350ms (figure 4.3). This reflection is interpreted to be caused by the interface between two shale layers, as the Hordaland Group was interpreted to be a series of stacked shale layer. The reflection is named Intra-Hordaland and is observed to have a depth variation between 1300ms and 1370ms (figure 4.7 right), and was interpreted for investigation of possible changes due to CO_2 injection in overlying strata.

Both the horizon has a small dip of very short relief with the highest location at the north end and the deepest location at the south end. Neither of these horizons will be widely used in the thesis.

4.3 Seismic reflectivity of the CO_2 containing sediments

4.3.1 Observable changes due to present CO_2

From chapter 2 it could be expected that the injected CO_2 in the underground will produce seismic reflections that are possible to map on the seismic dataset. This will be caused by the different acoustic impedance contrast that the seismic wavelet encounter at the interface on top of the CO_2 column, when compared to the interface it will have on the normal formation fluid. Compared to the baseline seismic survey (figure 4.8 left), the 2006 seismic survey (figure 4.8 middle) reveals high negative amplitudes that can be interpreted to be caused by the present of injected CO_2.

The negative amplitude is caused by a negative reflection coefficient that may come from the interference between sand/shale layer with normal formation fluids and the top of the CO_2 column, due to the differences of the acoustic impedance between the formation fluids and the injected CO_2. The reflection from the top of the CO_2 column have a phase reversal compared to the reflection at the seabed (figure 4.8 right), which is expected to have a positive reflection coefficient due to the interface between seawater and the seabed sediments.

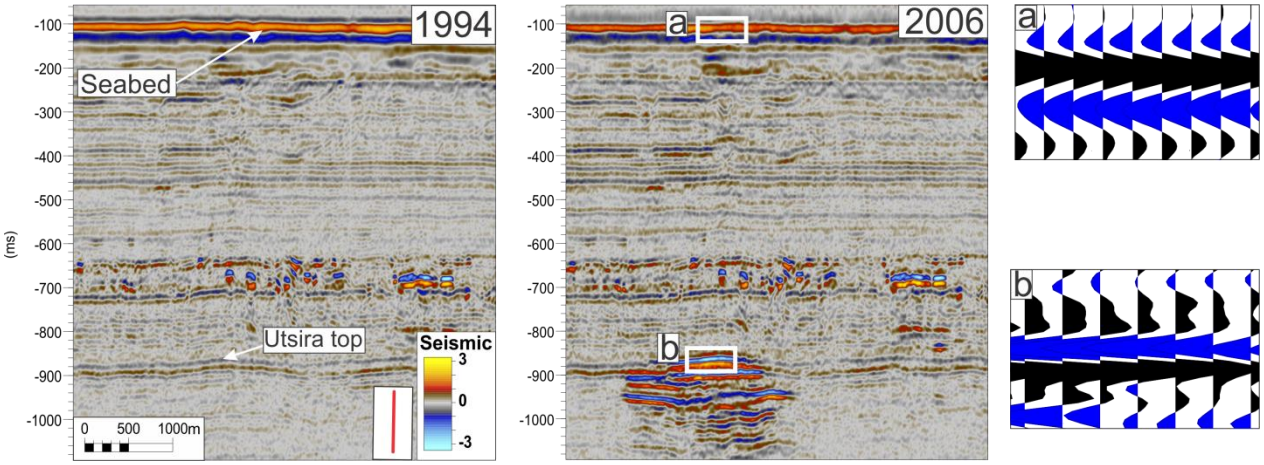

Figure 4.8: Showing the inline 1845 obtained for both the pre-injection seismic data (left) and the post injection data (middle). The seabed and Utsira top reflections are pointed out on the pre injection dataset, and the wiggle trace over the seabed reflection and over the interface of the CO2 accumulated layer from the post-injection layer is shown (right). The location of where the wiggle-traces of the seabed and CO_2 reflections are indicated on the 2006 dataset, with boxes named (a) and (b), respectively.

4.3.2 Seismic resolution over CO_2 filled sediments

From the last figure (figure 4.8), it could be observed what impact the CO_2 have on the seismic dataset, where the CO_2 is presented as observable negative amplitude anomalies on the seismic signal. To interpret the CO_2 layer thickness, saturation etc. it have to be established a baseline for the CO_2 and reflection amplitude.

A CO_2 thickness of approximately ¼ of the wavelength of the seismic signal will produce an overlap of the reflection from the top and base of the CO_2 accumulating layers, resulting in an interference and possible exaggeration of reflection (Andreassen, 2009), as seen in chapter 3. Seismic modeling (Rob Arts et al., 2004a) has shown that the tuning thickness for a sandstone filled with CO_2 is acquired by a CO_2 thickness of approximately 8m. However, the CO_2 may be detected on the seismic dataset with thicknesses of only 1m (S. Holloway, 2004). Since the CO_2 is accumulating under thin (approximately 1m) intra-reservoir shales, the easily detectable reflections over the CO_2 plume is caused by interference between the small intra-reservoir shales and the underlying accumulation of CO_2, giving the reflectivity of the CO_2 thickness to be estimated directly from the reflection (Bickle et al., 2007; Andy Chadwick et al., 2008; Delepine, Clochard, Labat, & Ricarte, 2011) (figure 4.9).

It has also been studied the tendency on how the reflection amplitude is changing as more CO_2 is accumulating under a capping layer. The objective was to detect the amount of CO_2 needed for producing the largest amplitude. This was observed to rather complex, where the reflection amplitude was affected by the tuning thickness of the CO_2, saturation of CO_2 and also dependent on the thickness of the capping layer, where the seismic response from the capping layer and the CO_2 column may produce both negative and positive interference with each other (Bickle et al., 2007; F. C. Boait et al., 2012). It is therefore a very complex matter when relating the amplitude anomaly with CO_2 thickness and saturation.

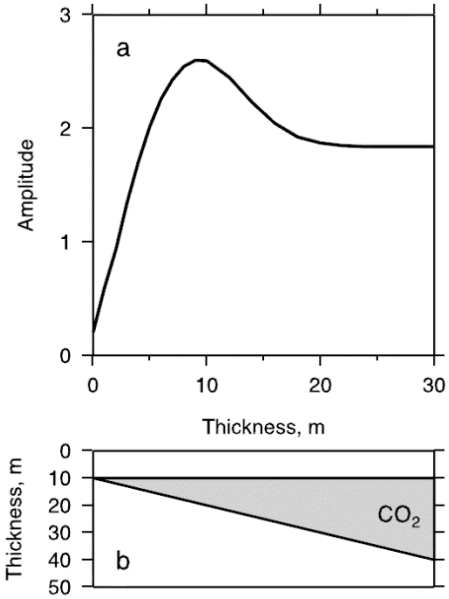

Figure 4.9: a) Amplitude value as a function of CO_2 accumulation thickness located within brine-saturated sandstone. b) Altering thickness of a CO_2 saturation corresponding to the amplitude change in (a). From (F. C. Boait et al., 2012)

4.4 Mapping of the CO_2 plume from time-lapse seismic data

4.4.1 Overview of the CO_2 plume

As explained in previous chapters, the use of repeated seismic surveys are the main monitoring tool for the CO_2 injection occurring at the Sleipner facility. By acquiring new sets of seismic data over the injection site, there are possible to follow the injection of CO_2 and its behavior over a period (since the seismic response of the seismic signal is as good as it is for the Sleipner case (figure 4.8)).

The baseline survey was acquired over the storage site two years before the injection started, where it provided crucial insight on the details for the storage formation that could be used for planning the location of the injection well (Andy Chadwick et al., 2008; Zweigel et al., 2004). There are several reasons why it is important to acquire a seismic baseline survey over the planned injection area. Firstly, as mentioned over, a detailed baseline survey is very convenient to use when choosing the location of the injection well. The injection well must be situated such that the injected CO_2 can encounter the maximum formation fluids that may trap it solubility, and that the CO_2 will migrate under a capping layer that prohibit it from escaping into the ocean. Secondly, interpretation of geological features on a baseline survey is important when injection CO_2 into a formation. This is because the monitored flow of the CO_2 can be tied up with these geological features, and to be certain on changes in the formation is caused by the injected CO_2 or not.

The monitoring data in this thesis have been constrained to include the surveys from 1994, 2001, 2004 and 2006. In figure 4.10a, the seismic inline 1873 is mapped from all the interpreted surveys, where the high negative amplitude anomalies are observed on the latter surveys. The figure clearly shows how the high negative amplitudes (i.e. CO_2) are growing with time. The CO_2 gives very detectable amplitudes that can easily be seen as something different from the 1994 baseline reflection in the Utsira reservoir interior. The strong seismic signals are seen from almost the bottom of the reservoir (from the injection point) and all the way up to the reservoir top, which is interpreted to be approximately 200m vertically distributed CO_2. The pre-injection survey from 1994 has few high amplitude anomalies, with some moderate reflections continuous throughout the survey. The Utsira storage formation, which is defined to be between the Utsira top and the Utsira base horizons, can be observed to only contain one reflection amplitude that it traceable on the pre-injection dataset (figure 4.3). The storage formation is stacked with thin (1m) instar-reservoir shales that was interpreted form the well-logs (figure 2.7), which does not produce enough reflection energy to be traced on the pre injection baseline. The thick shale has, in contrast, enough thickness (6-7m) to produce a continuous seismic signal. The seismic response from this layer can be traced over the entire baseline dataset such that is could be mapped, as seen in figure 4.5.

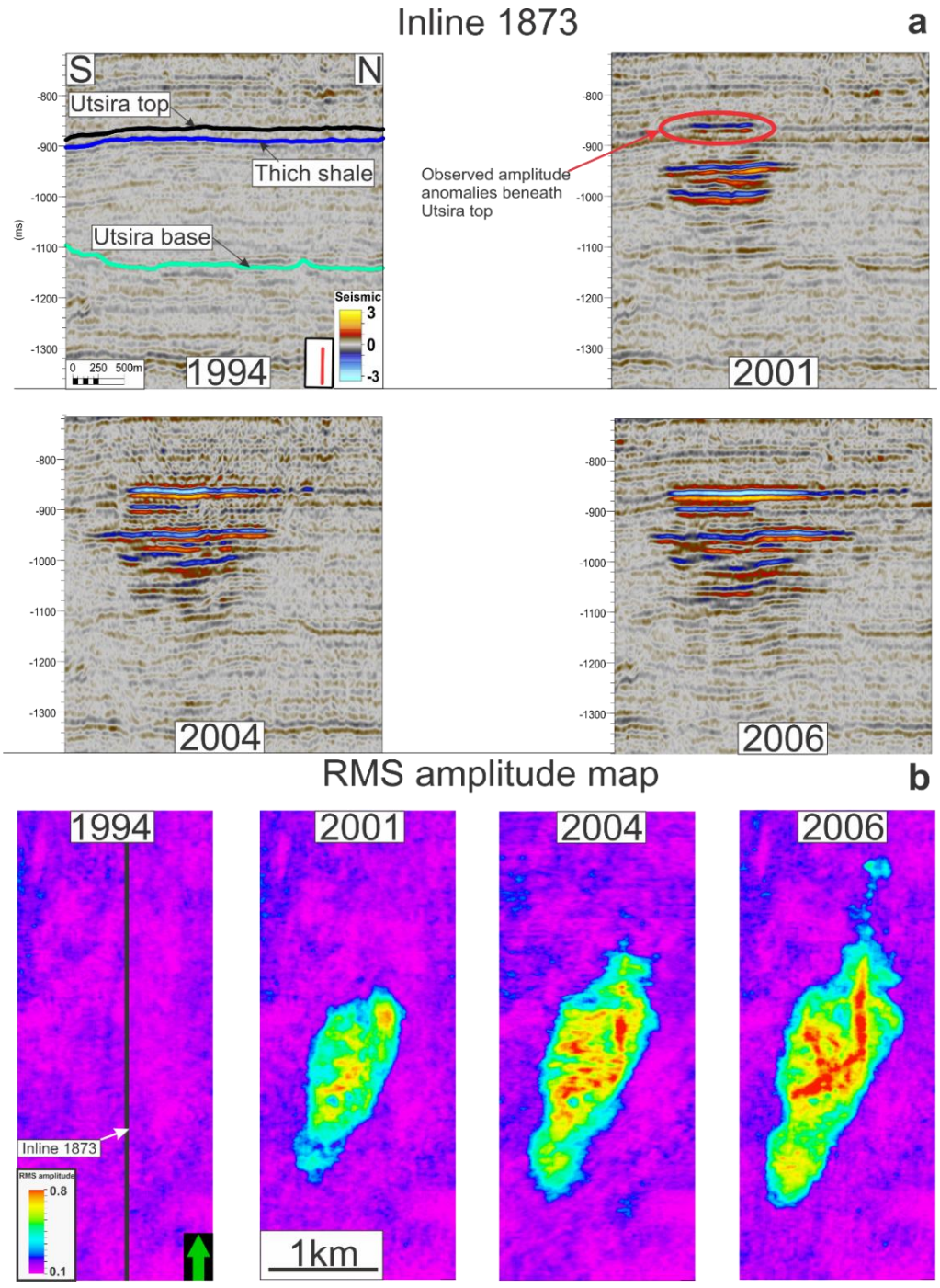

Figure 4.10: a) Seismic inline 1873 obtained over all the four interpreted seismic datasets. The baseline dataset indicates the three interpreted horizon within the storage formation, with Utsira top (black line), thick shale layers (blue line) and Utsira base (green line). The high amplitude anomalies observed in the storage reservoir on the latter datasets is interpreted to be seismic response form CO_2 filled layers. The red arrow with the red square on the 2001 dataset is indicating amplitude anomalies underneath Utsira top reflection, which indicate CO_2 migration under the top reservoir seal. It can be observed that the high amplitudes on the latter datasets are growing in vertical and horizontal distances as well as in amplitude, especially just below the reservoir seal. b) RMS amplitude map taken over the whole reservoir (from Utsira top and down to Utsira base), where the changes in amplitude is interpreted to be caused by injected CO_2. Inline 1873 from (a) is indicated on the 1994 RMS map. It can be observed a growth of high colors in the later dataset interpreted as CO_2 growth, and can be correlated with the seismic inline in (a).

The time-lapse seismic result from figure 4.10a indicate presence of a high negative amplitude in the topmost part of the storage formation by 2001 (indicated by red arrow and circle on the 2001 survey). This is interpreted to be CO_2 accumulating under the Utsira top reflector, indicating that the CO_2 have migrated laterally up from the injection well and accumulating under the reservoir top seal by 2001 – five years into injection. On the same inline, it can be seen how the bright negative reflections are growing in both vertical and lateral directions, as well as in amplitude on the later datasets.

Because the CO_2 presents high (negative) amplitude anomalies on the seismic datasets, the use of RMS (minimum) amplitude is exceptional a good tool for mapping the lateral spread of the CO_2 plume (figure 4.10b). The RMS amplitude map obtained over the whole reservoir can be seen in figure 4.10b, where it can be tied together with the seismic section to monitor how the total CO_2 plume is growing in both the lateral extent and the strength of the signal. The RMS amplitude map obtained over the baseline (1994) dataset has none or few amplitudes in the reservoir, whereas the RMS amplitude maps obtained over the later datasets have clearly colored regions, which with correlation of the seismic sections, can be interpreted as the location of the injected CO_2. Due to the lack of high amplitudes on the RMS amplitude map obtained from the 1994 dataset, the colored regions on the three latest dataset is supported to be caused by the presence of injected CO_2 in the storage formation.

From RMS map obtained over the first post-injection dataset in 2001, the colored regions are observed to have a main spread in the NE-SW direction. On the later RMS maps obtained for the 2004 and 2006 dataset revealed that the orientation of the colored regions are staying in approximately the directions as first observed from the 2001 dataset. The spread of the whole CO_2 plume can be seen as an elliptical shape with the long axis in the NNE-SSW direction, and the short axis in the WNW-ESE direction. The length of these axis have been calculated for the three post-injection dataset, with use of the eye-fitted ellipses obtained over the RMS amplitude maps from figure 4.10b (table 4.2).

Survey	1994	2001	2004	2006
Extent long axis (NNE-SSW)	N/A	2000m	2500m	3600m
Extent short axis (WNW-ESE)	N/A	800m	900m	950m
Eccentricity	N/A	2.5	2.78	3.6
Area	N/A	1.25km^2	1.77km^2	2.83km^2

Table 4.2: Showing the calculated values obtained from the colored regions, interpreted as lateral distribution of injected CO_2, from the RMS amplitude map in figure 4.10b. The general observations is the relatively large differences between the long and short axis, and that the long axis is experiencing more growth over time. The values are only approximately, as they are obtained from ellipses fitted by eye.

From the calculated values in table 4.2 it can be observed that the lateral spread of the injected CO_2 has grown more rapidly for each year, where it have increased in areal size of approximately 40% from 2001 to 2004 and 60% from 2004 to 2006. It is obviously a bit incorrect to say anything etailed about the annual growth of the plume, since there are different periods between the datasets, and the annual amount of CO_2 in the storage formation can only be roughly estimated. An important observation is the relatively large lateral increase for the long axis for the CO_2 plume. From the first observation in 2001 the long axis has grown to a value of approximately 2000m, whereas it have grown to a value of 2500m by 2004, and a value of 3600m by 2006. This give an approximately increase of 500m and 1100m between 2001 to 2004 and 2004 to 2006, respectively. By keeping in mind that there is only a two years difference between 2004 and 2006, whereas a three years difference between 2001 and 2004, it can be interpreted that the lateral growth of the long axis is increasing with time. The relative large lateral growth in the timespan 2004 to 2006 is interpreted to be mainly caused by the observed CO_2 reflections situated furthest north on the 2006 amplitude map (figure 4.10b), which seem to be the largest difference compared to the earlier amplitude maps.

The lateral spread of the short axis of CO_2 ellipses are in contrast indicating a rather slower increase. The short axis have only increased from approximately 800m in 2001, to 900m in 2004, and to 950m in 2004. This indicates a limited lateral increase for the plumes short axis, where (considering the period between the datasets) it have a negative growth flux. It is therefore reasonable to interpret that the main lateral growth is occurring in the long axis of the elliptical shape, whereas the short axis seem to have reached some sort of equilibrium, or is close to reaching it.

The plume has been observed to grow steadily in its lateral extent, with primarily growth in the NNE-SSW direction, but can also be seen to have amplitude growth in the central part of the plume as well (figure 4.10b). The central part of the plume are going from a more-or-less yellow color in 2001 into a much more red color by 2006, which imply more high amplitude anomalies within the volume of the RMS map, which is interpreted as more CO_2 is being accumulating within the central part of the plume. This is also evident from the seismic inline 1873 (figure 4.10a). The general interpretation for the whole storage formation is therefor that the injected CO_2 are migrating within the center of the plume as well as being spreading laterally in the NE-SW direction.

4.4.2 Internal growth of the CO_2 plume

In the last subsection, it was observed how the reflectivity from the entire storage reservoir changes due to the injected CO_2. In this subsection, it will be looked more in detail on how the injected CO_2 is behaving within the storage reservoir, and if there can be observed any trends.

If the CO_2 had been injected into a storage formation with the same reservoir properties as for the Utsira storage formation, under the assumption that it was a homogenous sandstone package, it could be expected that most of the CO_2 would migrate and accumulate at the shallowest part on the reservoir top. This is, in contrast, not the result from CO_2 being injected into the Utsira storage formation. The CO_2 is observed to be accumulating at different vertical locations throughout the formation (figure 4.10a). On the first post-injection dataset from 2001 it could be observed how the CO_2 was accumulating at nine different vertical locations. The CO_2 is observed to be accumulating at approximately the same nine location in the two latest datasets as well. Since the CO_2 seems to be accumulating at these nine horizons for each dataset, the changes of these locations with time could be followed. The accumulation of CO_2 at these specific nine location was interpreted to be CO_2 accumulated beneath layers that inhibits some capping properties (R. Arts et al., 2004b; Bickle et al., 2007).

From the description of the storage formation given in chapter 2 and in the beginning of this chapter, it was explained that the formation consisted of several intra-reservoir shales. The small shales was interpreted to be rather discontinuous and not expected to have any good sealing effectiveness. The nine observed CO_2 accumulations is therefore interpreted to be CO_2 accumulated beneath these intra-reservoir shales, which only becomes visible on the seismic datasets when CO_2 is captured beneath. The CO_2 is expected to be concentrated in the upper parts of the sand packages separating the shales because the density of the injected CO_2 is less than the density of the original formation fluids (R. Arts et al., 2004b), which generate a greater change in acoustic impedance when going from the shale layer into the CO_2-filled sandstone. The large shale close to the top Utsira is as mentioned earlier expected to have more effective sealing capacity. Whether it could seal the CO_2 for a long time or be migrated through early was difficult to estimate, although most studies tends to give the injection a few years before migrating through it (Rob Arts et al., 2004a; Zweigel et al., 2004). It can be observed negative amplitude anomalies just beneath the Utsira top horizon already on the first post-injection dataset, indicating CO_2 accumulating inside the upper sand package and thus the thick shale have been migrated through (figure 4.10a).

The nine specific location with accumulating CO_2 have been interpreted and mapped out from the seismic time-lapse datasets (figure 4.11), with the lowest observable CO_2 layer referred to as layer 1 and the upmost observable CO_2 layer referred to as layer 9. The layers were carefully picked on all seismic inlines and crosslines, and was locally terminated as soon as the reflection was similar to the background anomalies from the 1994 survey. The use of the Multivolume attribute was particularly suitable for this interpretation.

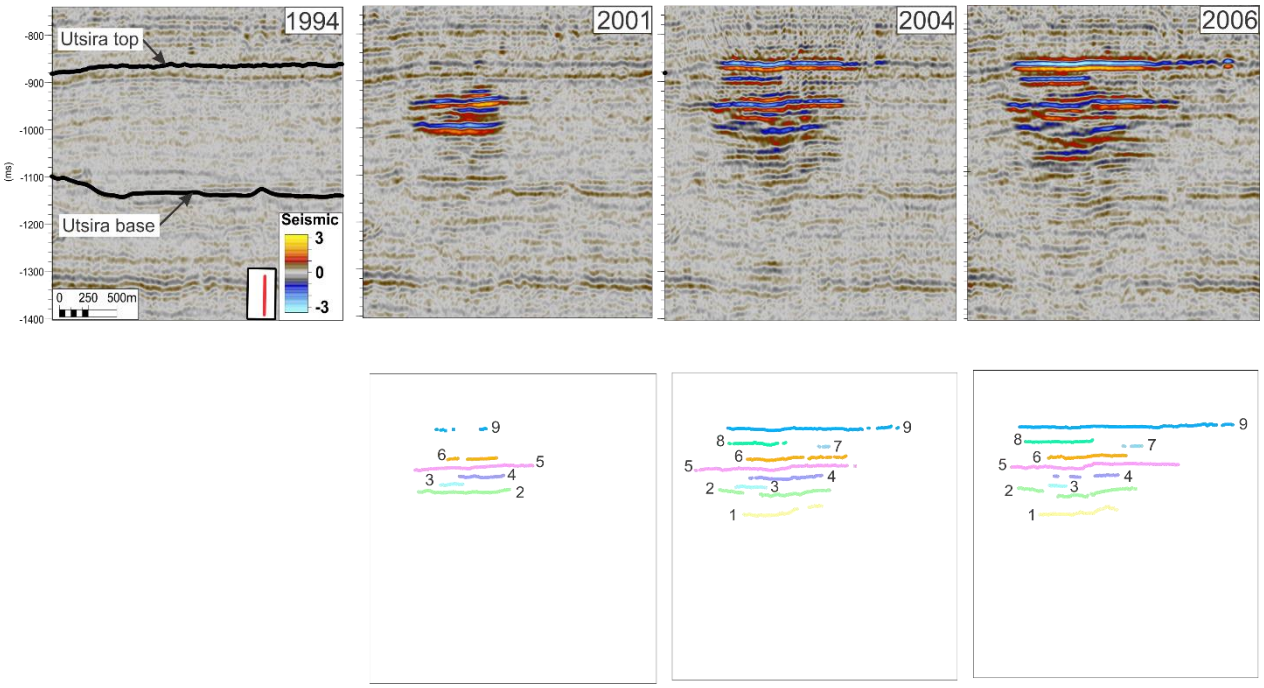

Figure 4.11: Showing the location for the internal CO_2 accumulation. a) Seismic inline 1870 obtained over all the interpreted dataset, with indicated location for Utsira top and Utsira base reflector on the 1994 dataset. b) Same seismic inline as (a), only for the post-injection survey with white background. The nine internal CO_2 accumulations have been indicated, with CO_2 layer 1 referred to as the lowermost accumulation, and CO_2 layer 9 referred to as the uppermost accumulation.

From figure 4.11, the CO_2 accumulations at the different layers can be followed in time, where they seem to be located at approximately the same locations on all the post-injection datasets. To investigate how these nine layers are changing with time in detail, there were created horizons over the interpreted CO_2 layers. Furthermore, to examine how the reflectivity over the amplitude anomalies changes with time, there was created Minimum amplitude maps over each of the mapped CO_2 horizons (figure 4.12). These 24 minimum amplitude maps was created to examine how the reflection amplitude anomalies changes with time and location, and to possible be correlated with the observed amplitude obtained over the whole storage reservoir (figure 4.10b).

The nine layers are observed to be within the storage formation, and have the same general form as the total plume. Approximately all of them are elliptical in shape with the longest axis stretching in a NNE-SSW direction, and have eccentricities ranging between 1.5 to 4.5 (figure 4.12).

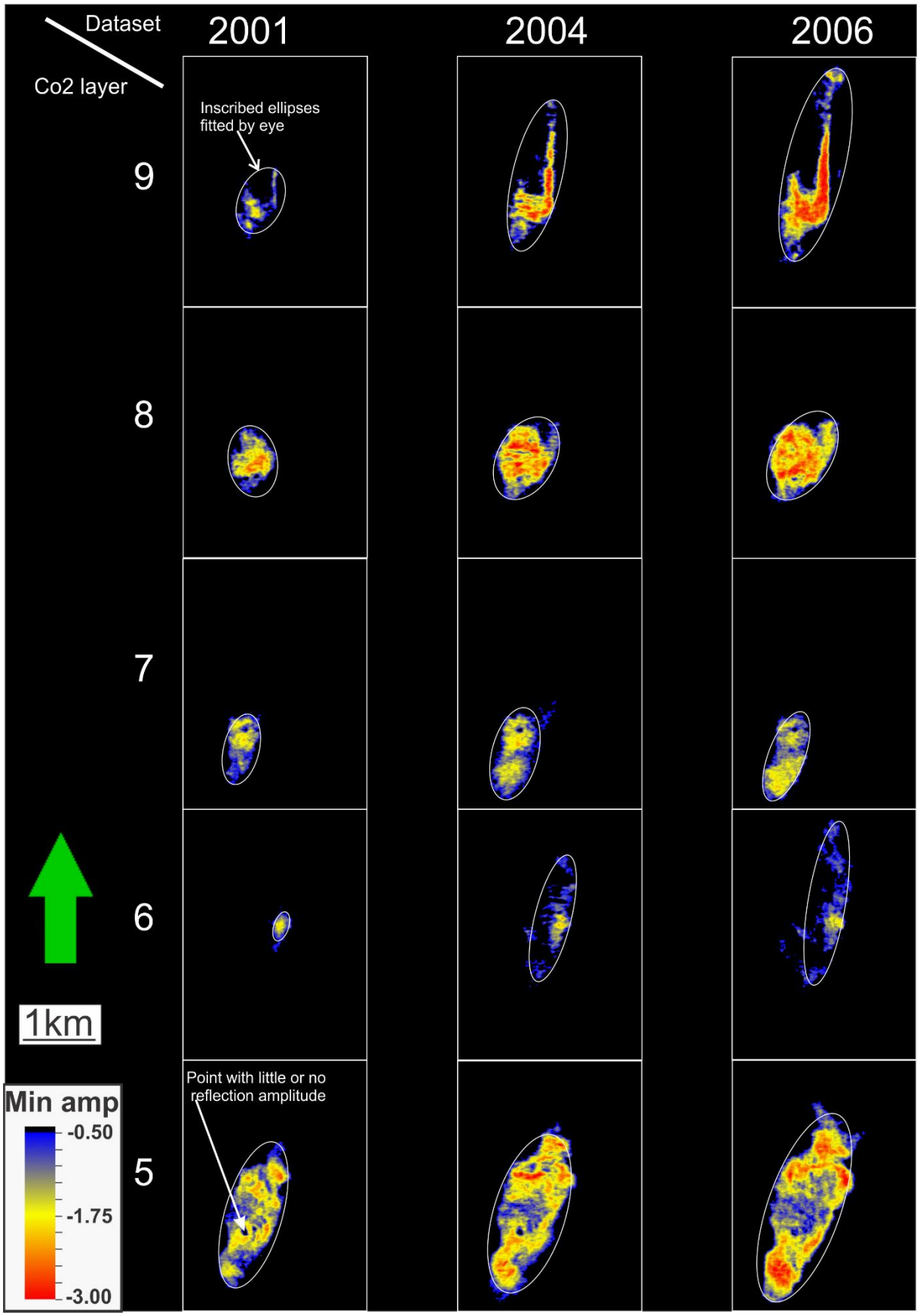
Dataset
Co2 layer
2001
2004
2006
Inscribed ellipses fitted by eye
9
8
7
6
5
1km
Min amp
-0.50
-1.75
-3.00
Point with little or no reflection amplitude

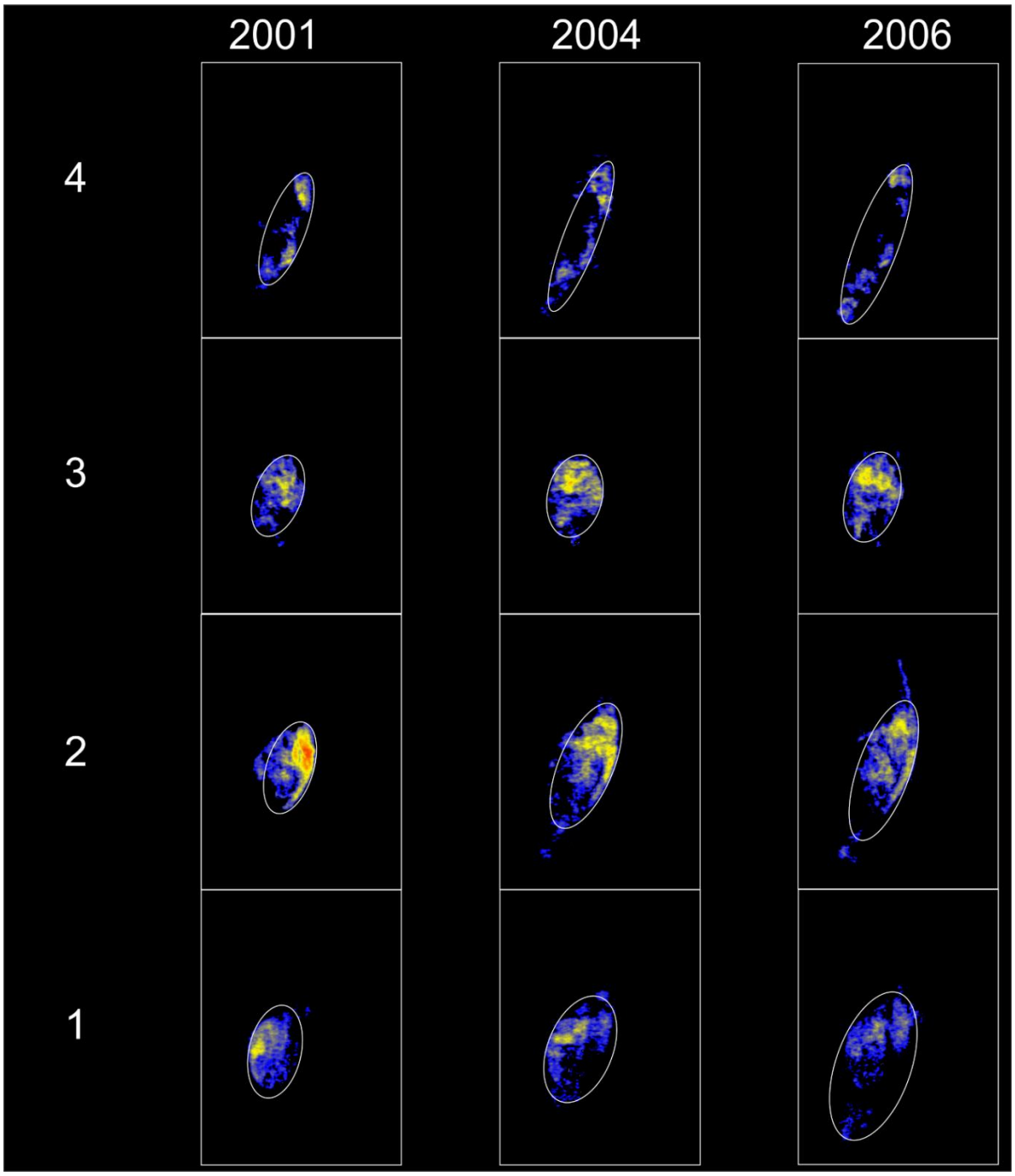

Figure 4.12: Minimum amplitude maps obtained from the interpreted horizon over the 27 (9x3) CO_2 accumulated layers within the storage formation. Layer 1 is referred to the lowermost observed CO_2 accumulation, and layer 9 is referred to the uppermost observed CO_2 accumulation (see figure 4.11 for layer positioning). Warmer and colder colors indicate stronger and weaker reflection amplitudes, respectively. The minimum amplitude maps are obtained over the mapped negative amplitude reflection observed on the seismic datasets, which has an average vertical thickness of approximately 10ms. The minimum amplitude maps are presented such that they are situated relatively to each other (i.e. a point (x, y) in one of the white boxes will be the same point in the other white boxes). The white ellipses that are drawn over every amplitude anomaly is an eye-fitted ellipse that covers most of the reflection. The white arrow on the CO_2 layer 5 for 2001 indicate an area/circle without strong reflection amplitude. This point can also be seen on other anomalies that covers that point. It can be observed that the general form of the fitted ellipses having a long axis in the NNE-SSW direction and a short axis in the WNW-ESE direction,

From the minimum amplitude maps presented in figure 4.12, one can be observe how the reflection amplitude anomalies is changing with time. Some of the internal CO_2 layers are observed to be growing in time (especially layer 5, 6, 8 and 9), some layers are observed to be stop growing in time (layer 3 and 7), whereas some layers is observed to be reducing in reflection amplitude (layer 1, 2, 4 and 6). The growth of each individual internal layer can be seen as a three-stage growth model (Bickle et al., 2007; F. Boait, White, Chadwick, Noy, & Bickle, 2011; F. C. Boait et al., 2012). The first stage of the sequence is the growth in lateral direction of the layer, which happens at a relatively high speed, and induces a bright reflection as the wavelet is reflected by the CO_2 instead of the normal formation fluids. The second part of the sequence is characterized by a more slowly growth of the layer, and the reflection in the center are dimming while the amplitude at the sides may continue to brighten. This is followed by the third part where the growth of the layer seems to be stopping and, in some instance, it shrinks and the overall amplitudes dims.

Most of the layers seems to have reached its maximum growth in the short elliptical axis direction (i.e. the length of the short axis is not observed to be growing as fast as the long axis). This has also been seen on the total growth of the plume, where the growth in the short axis seems to stop, and having the major lateral growth only in the long axis direction.

Under is a figure (figure 4.13) where it shows how the internal plume horizons from the 2006 seismic dataset are situated relatively to the Utsira base.

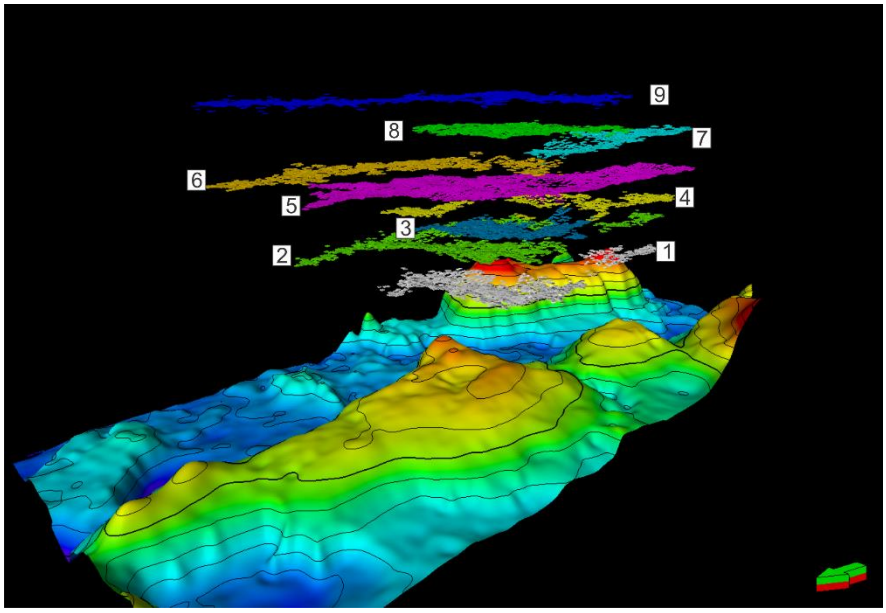

Figure 4.13: 3D overview of the interpreted internal CO_2 horizons from the 2006 seismic dataset. All the nine horizons are numbered with number 1 to number 9, representing the shallowest to the upper CO_2 accumulations respectively. Also included in the figure is the Utsira base horizon interpreted from the 1994 dataset, which is used for scale and location. The Utsira top horizon is not included due to interference, and will be situated at the same location as the topmost CO_2 accumulation (layer 9).

From figure 4.12 it can be observed that the upper layers are experiencing an increase of reflection amplitudes, whereas the lower layers seems to lose reflectivity and are experiencing dimming of amplitude reflection with time. By 2004, the lowermost layers (layer 1 – 4) seems to have reached the place where its reflection amplitude in the central part is dimming as well as some layers experience lower reflection amplitude also at the edges, whereas the middle layers (layer 5 and 6) are beginning to lose reflection amplitude in the central part by 2006. The two uppermost layers (layer 8 and 9) have no sign of amplitude reduction in neither the central nor the outer parts by 2006, and is rather experiencing a reflection amplitude growth.

It is also interesting to see how the continuity of the plume reflection differ over time. It can be seen that the layers 1, 2, 4 and 6 are going from a continuous reflection into a more patchy reflection, and that the layers 3, 5, 7 – 9 are highly coherent and seem to stay at one piece for all the interpreted datasets. This, along with the observed reflection amplitude dimming in most of the lower CO_2 layers, is making it quite tempting to interpret that the lower CO_2 accumulation is leaking more CO_2 to the overlying layers than experience influx. Although this may be true, but has to be treated with considerable caution, since there can be several reasons why the reflection amplitude in the lower levels can lose its reflectivity (Bickle et al., 2007; F. Boait et al., 2011; F. C. Boait et al., 2012).This will be discussed more closely in the discussion chapter (chapter 5).

Another interesting feature that can be observed from the individual CO_2 plume layers is that they all fit into an elliptical planform in one way or another (white ellipses drawn around each amplitude anomalies in figure 4.12). The overall trend for the CO_2 layers is that they follow the same lateral distribution as is observed for the whole plume (figure 4.10), with the long axis in the NNE-SSW direction and the short axis in the WNW-ESE direction. The relationship between the short and the long axis (eccentricity) was calculated to be in the range between approximately 1.5 and 4.5 for all the layers. The general trend for the CO_2 layer eccentricities is that the values increase over time (as for layer 1, 2, 4 – 6 and 9), which indicate that the layer is experiencing either more lateral growth in the long axis direction or more lateral decrease in the short axis direction, or a combination of these. Although a few layers are experiencing the opposite, with a reduction in eccentricities (as for layer 3 and 8), and the rest of the layers have quite constant values with time. The general interpretation for this trend is that the lateral spread of the injected CO_2 is being confined in the NE-SW direction for the CO_2 layers. The lateral spread in the short axis is happening at a slower rate. The CO_2 spread in this direction can furthermore be interpreted ta have stopped. The same interpretation was also made for the entire plume, which may indicate that the total plume behavior is dependent on every CO_2 accumulation, and is not expressed by the behavior of only a few.

4.4.2.1 Growth of the two topmost CO_2 accumulations (layer 8 and 9)

The two topmost CO_2 accumulation observed in the time-lapse datasets (layer 8 and 9) are interpreted to be CO_2 accumulation under the two topmost horizons; "thick shale" and "Utsira top", respectively. Because these horizons can be identified and interpreted on the baseline dataset prior to possible disturbances caused by injected CO_2 (figure 4.4 and 4.5), they provide insight on how the injected CO_2 behaves when reaching a capping topography. To examine the CO_2 behavior underneath the capping topographies, there were generated polygons that indicates the lateral distribution of the two CO_2 layers obtained from each post-injection dataset, which can be seen as a rough growth model. The polygons were placed on the associate capping horizon to see where the CO_2 was accumulating (figure 4.14).

From figure 4.14, it can be observed that the CO_2 is following the topography of the overlying capping layer, and is accumulating at the location with the shallowest relief in the closest area of where it was first observed. From these results, it is interpreted that the storage formation have a relatively normal pressure gradient, and the CO_2 is flowing to areas with lowest pressures.

From figures 4.12 and 4.14, it can be observed that the injected CO_2 that is accumulating under the thick shale (CO_2 layer 8) are keeping a rather steady lateral orientation. The areal increases have been calculated to be of approximately $1km^2$ from 2001 to 2004 and an even smaller increase of approximately $0.74km^2$ from 2004 to 2006, and seem to have reached more-or-less an equilibrium in its lateral spread. However, it can be seen from figure 4.12 that the reflection amplitude over the layer is still showing tendency to increase in strength by 2006. This may indicate that the layer is still experiencing a growth of CO_2 that is capped by the thick shale, although caution needs to be made as the amplitude strength does not have a certain causality with increase of CO_2 amount, as explained in the beginning of the chapter.

The topmost CO_2 layer in the plume is of special interest for two main reasons (Andy Chadwick et al., 2006a; R. A. Chadwick, Noy, Arts, & Eiken, 2009). The first reason is that it is the topmost accumulation of the CO_2 in the formation (in the upper sand package situated between the thick shale and Utsira top), and thus making it the best option regarding to volume estimation since it is not affected by the velocity pushdown from CO_2 saturated levels above. The second reason is that the growth in this level will represent the total upward flux of CO_2 through the reservoir and it is possible to examine whether the CO_2 flux upward is changing with time, or if the top layer is experience the same amount of CO_2 flux each year.

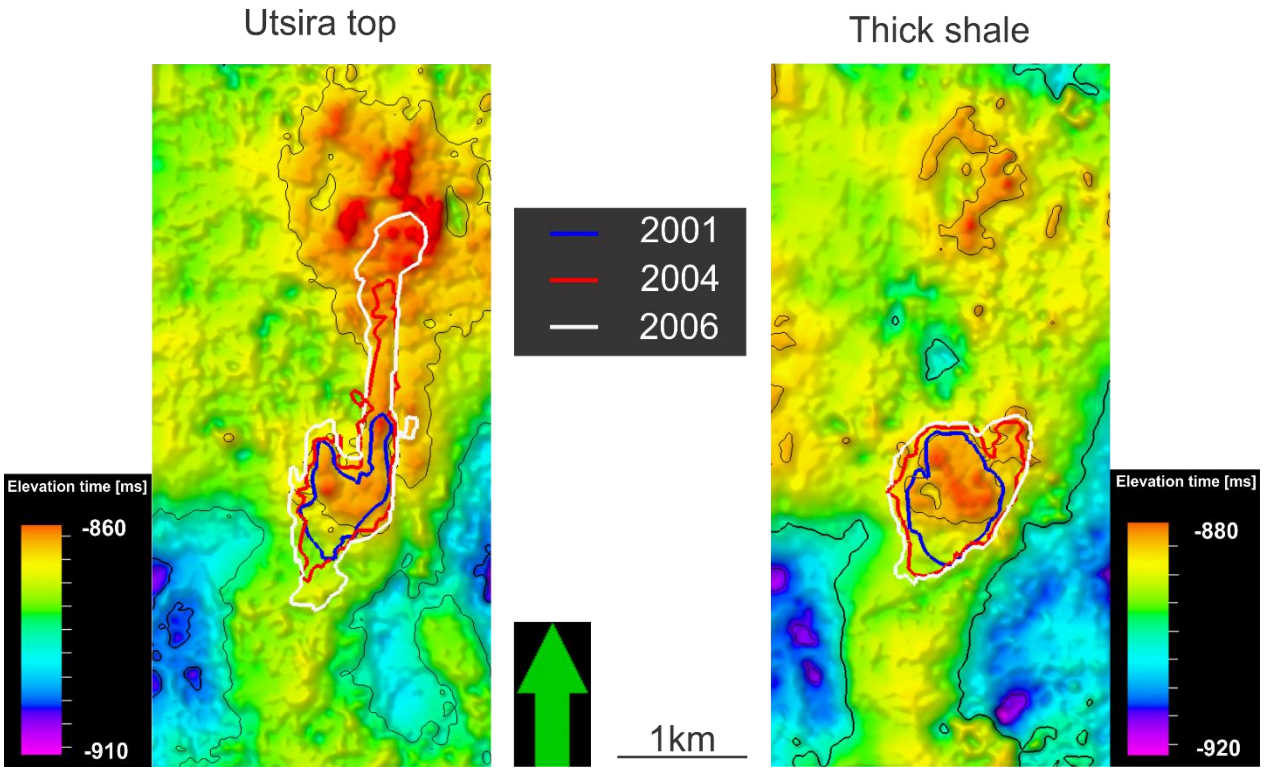

Figure 4.14: Showing the interpreted horizons from reflections at the Utsira top (left) and the thick shale (right), as seen in figure 4.4 and figure 4.5 respectively. The interpreted horizons have here three polygons each. The polygons indicated in the figure corresponds to the maximum lateral spread of the CO_2 layer that is accumulating under the specified horizon at the different years, with 2001 (blue), 2004 (red) and 2006 (white).

The accumulation of CO_2 in the upper sand package (CO_2 layer 9) was observed to be evident on the first post-injection dataset from 2001 (figure 4.10a). This layer is observed to be one of the internal CO_2 layers that have experienced both the largest lateral spread and the most increase of reflection amplitude (figure 4.12), accompanied with CO_2 layer 5. The layer is observed to be growing mostly in the NNE-SSW direction, and because of its good reflection amplitude it is interpreted to play a major part in the mapping of the whole plumes spread done by amplitude maps (figure 4.10b). To map out the growth of the topmost layer reflection there were created subtraction cubes between the datasets. Since the topmost reflection is not affected by pushdown from overlying CO_2 layers, the results from the subtracted cubes are of relatively good qualities (figure 4.15). The inlines over the subtracted cubes (figure 4.15a) reveal very good results from the 2006-2001 dataset, where the difference in reflection amplitude for the topmost layers is showing prominent growth (figure 4.15b). The subtracted cubes containing the dataset from 2004 are observed to have some amount of noise, which is interpreted to be caused by the differences of the acquisition parameters (Andy Chadwick et al., 2008).

From the created horizons obtained from CO_2 layer 9, there was calculated approximately values for the covered areas for the three post-injection datasets. With a furthermore assumption of CO_2 layer thickness and densities (Akervoll et al., 2009; A. Chadwick et al., 2006b; R. A. Chadwick et

al., 2009), the amount of CO_2 trapped in the upper sand package beneath the Utsira top could be calculated. The approximately amount of CO_2 being stored in the upper sand package was interpreted to be 40000 tons CO_2 by 2001, 140000 tons CO_2 by 2004, and 350000 tons by 2006. From these numbers there can be observed a steady increase of input flux of CO_2 in the upper sand package with time, and, by keeping in mind that there is a smaller time span between the two latter datasets, the growth of the CO_2 layer 9 is relatively enormous. The increase of CO_2 in the top sand package can be calculated to be 250% from 2001 to 2004, 150% between 2004 and 2006, and 775% between 2001 and 2006. This is supported by the observed amplitude growth of the top CO_2 layer seen in figure 4.15b.

From chapter 2 it was presented the accumulatively CO_2 mass injected into the Utsira formation per year (approximately 0.95Mt CO_2), which gives a stored amount of CO_2 to be approximately 4.75Mt CO_2 by 2001, 7.6Mt CO_2 by 2004, and 9.5Mt CO_2 by 2006. From these values, it can be calculated that the topmost CO_2 layer is approximately containing 0.8% of the total injected CO_2 by 2001, 1.85% by 2004, and 3.7% by 2006. In other words, there is an increase of CO_2 being observed in the top layer relatively to the total amount of injected CO_2 with time.

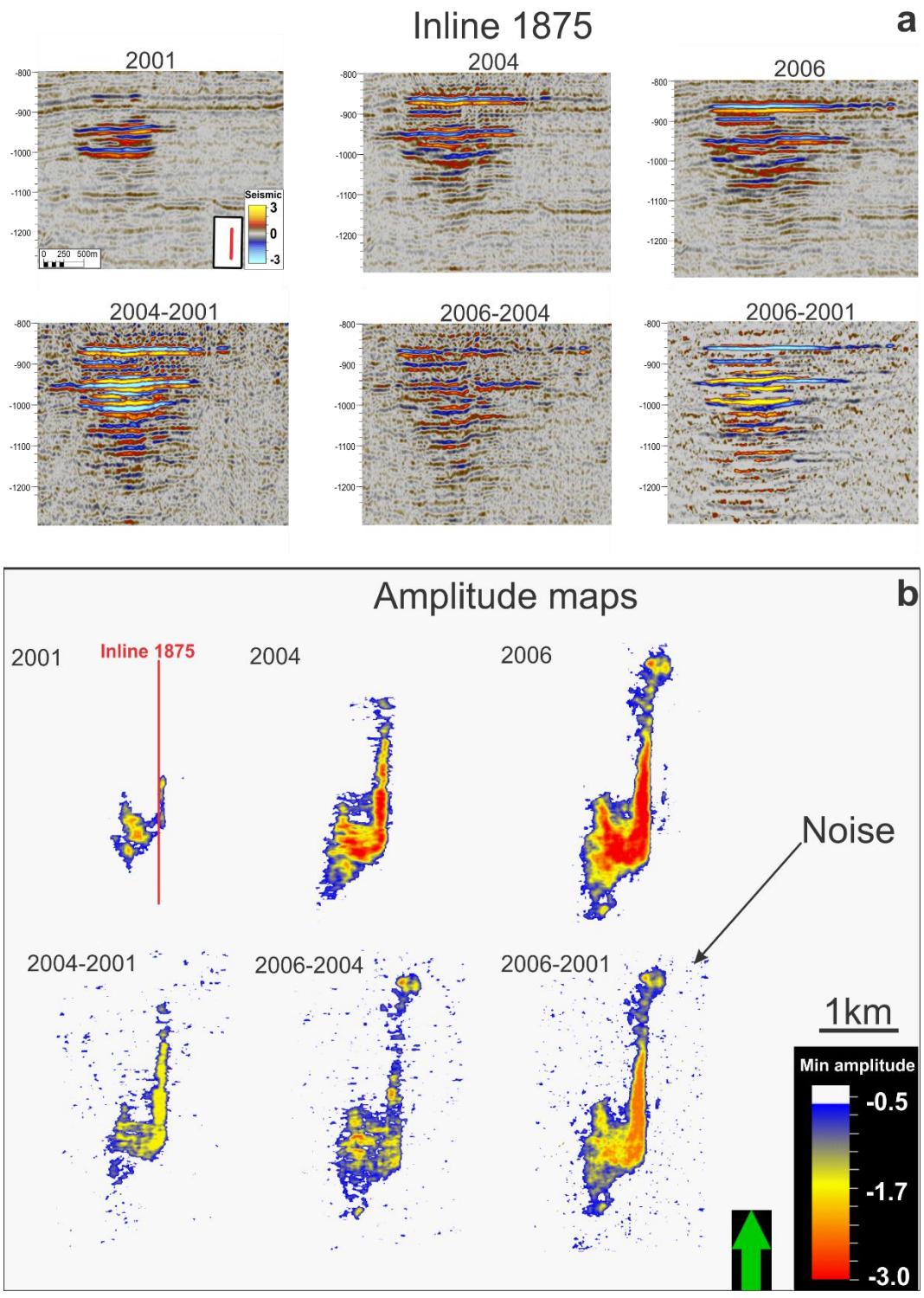

Figure 4.15: Growth of the topmost CO_2 layer. a) Seismic inline 1875. Seismic inline obtained over the original post-injection seismic datasets (top), and the same seismic inline obtained over the subtracted datasets (under), as indicated. The latter inlines can give an indication of the high amplitude increase over the storage formation, although the pushdown beneath a CO_2 layer will affect the subtracted cubes. The only CO_2 layer that is not affected by the pushdown of overlying CO_2 accumulations is the topmost layer (layer 9). b) Minimum amplitude map obtained from the original seismic datasets (top), and from the subtracted datasets (under). Due to different acquisition parameter from the seismic datasets, there is some noise indicated by the black arrow.

4.4.3 Vertical migration through the storage formation

The CO_2 is being injected close to the base of the Utsira storage formation, in order to give it the most possible lateral spread as it migrates upward the formation (R.A. Chadwick, 2004b). It have been observed that the CO_2 have migrated from the injection well and all the way (approximately 200m) up to the top of the formation by 2001 (figure 4.10a). It has also been evident for CO_2 accumulation in this layer already by 1999, where observations of small amplitude anomalies has been made only three years into injection (Andy Chadwick et al., 2008; R.A. Chadwick, 2004b). The migration of CO_2 from the injection well and up to the caprock is interpreted to be driven by the buoyant force due to the relatively light CO_2 compared to the denser formation fluid (R. Arts et al., 2004b; F. C. Boait et al., 2012). The accumulation in the topmost structure of the storage formation (CO_2 layer 9) is an evidence of the lack of sealing capacity for both the small intra-reservoir shales and the thick shale close to the reservoir top. In other words, the injected CO_2 have migrated from the injection well and upwards the storage formation, penetrating through the shale layers. Furthermore, the CO_2 have reached the formation top and started to accumulate at this location with a relatively high flux as was shown in the previous subsection.

From the interpreted seismic datasets one can observe a near-vertical feature that seem to origin close to the lowest levels of CO_2 detection and terminate close to the topmost CO_2 detection (figure 4.16), and is characterized with a relatively low reflection amplitude. The feature is situated close to the center of the plume, and have an internally u/v – shaped pushdown where the reflection amplitude is low (figure 4.16a). The features lateral extent is measured to be in the range 50 – 150m. The vertical length of the feature is measured to be approximately 150m. This was measured by correlating with the pre-injection seismic because the vertical distance in the post-injection survey is affected by the velocity pushdown from the injected CO_2 (will be presented more clearly in chapter 4.4.4). The time-slices through the 2006 dataset (figure 4.16b) shows how the feature is behaving in the storage formation, where it can be observed that the intra-reservoir shales seem to be broken at almost the same location. The feature is interpreted to be one of the migrating channels that the CO_2 is following upward the formation, and may be acting as a chimney (Andreassen, 2009; A. Chadwick et al., 2006b; Loseth et al., 2009).

The chimney structure is located near the injection point for the CO_2, though not perfectly, but at the outer limit of the 95% confidence ellipse of the well position (R. Arts et al., 2004b; R.A. Chadwick, 2004b). It must be considered whether the chimney structure is a result of the injected CO_2, or that it have been developed prior to the injection. From figure 4.16a it can be followed the same inline through all the datasets, and there cannot be observed such feature on the pre-injection baseline. It is therefore natural to assume that the injected CO_2 have created a flow path through the intra-reservoir shales (as they was interpreted to not have fully sealing effects). From figure 4.12 we observed a small circle in the SW area of the amplitude anomalies (pointed out with the white arrow on layer 5 for the 2001 seismic dataset), which is situated exactly over the interpretation of the chimney structure. Since the mapped amplitude anomalies in figure 4.14 is

situated relatively to each other, the small circle (chimney) can be seen on other of the anomalies that cover this area.

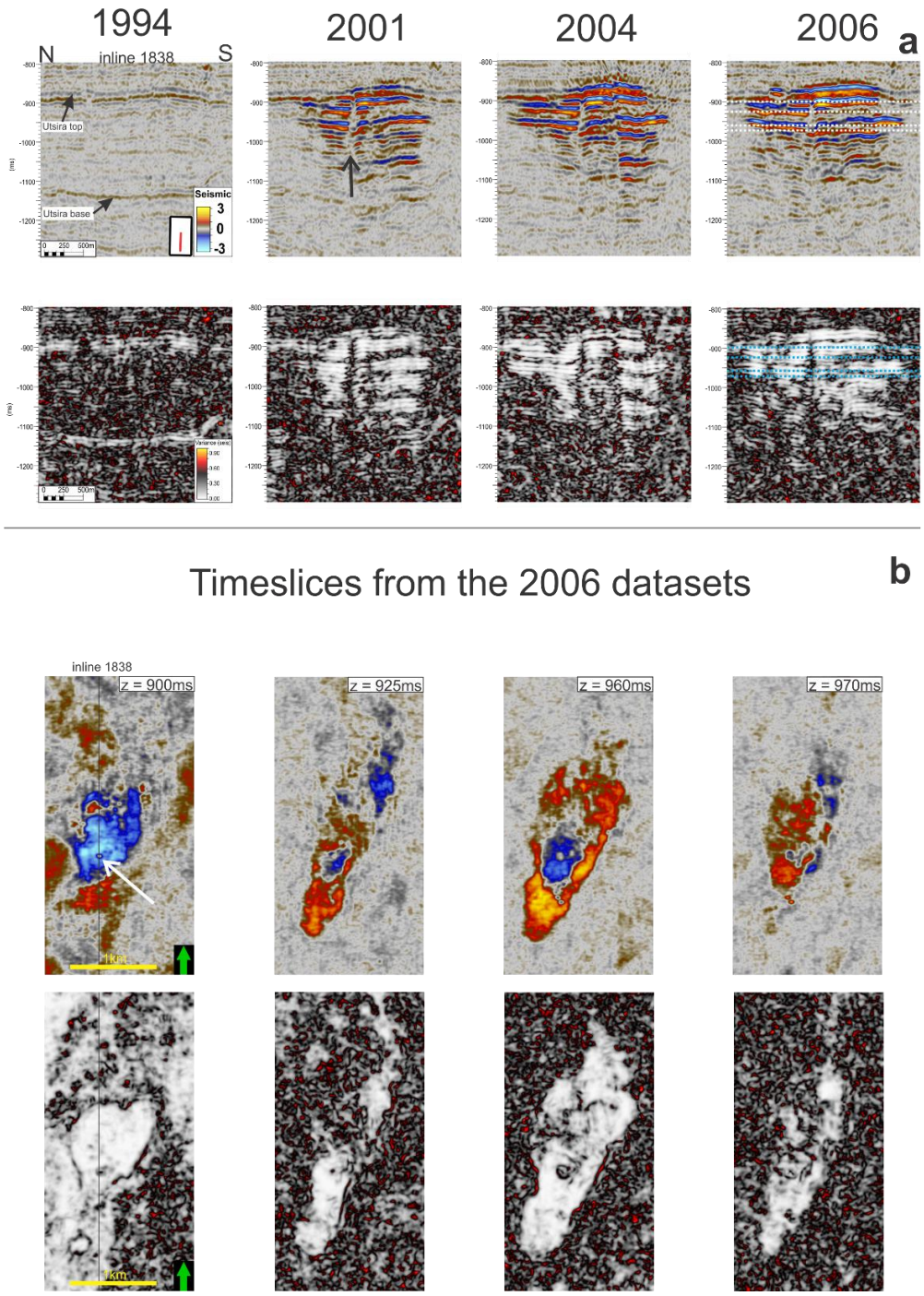

Figure 4.16: Mapping of the chimney feature. a) Seismic inline 1838 obtained over all the interpreted datasets, both original seismic and chaos. The vertical area with little or no reflection amplitude can be observed on the post-injection surveys. Location is indicated with black arrow on the 2001 dataset. b) Timeslices obtained from the 2006 dataset for both the original and the chaos seen in (a). White arrow on the 900ms timeslice indicate the location of the chimney structure, which can be followed on the deeper slices as well.

In order to map more of the areas between the CO_2 layers, and to see if there are any changes in time, there was applied RMS amplitude maps obtained between the layers (figure 4.17). The maps was generated from when the negative reflection ended at one layer, and down the when the negative reflection of the underlying layer started. The figure is only used between layers with relatively good continuity (meaning that layer 1, 4 and 6 is not evaluated). However, several factors are constraining the results. Firstly, the CO_2 accumulated layers are CO_2 capped by the thin intra-reservoir shales that could not be mapped prior to the injection, making the position of the RMS boundaries very locked. Secondly, the CO_2 layers are not situated perfectly on top of each other, which results in mapped areas only when the two layers overlap. Due to these constrains, the figures does not reveals as much information as hoped.

From the figure 4.17, it can be observed that the RMS is able to map out the interpreted chimney feature between the layers, but seem to be limited to the area from layer 8 to layer 5. Beneath layer 5, the CO_2 layers are situated somewhat just aside from the chimney structure. This can be caused by that the chimney is migrating CO_2 in only small thicknesses, and thus cannot be revealed on the seismic data. Another explanation is that other sources or chimneys are migrating into these layers. From CO_2 layer 5 and up to layer 8 there can be observed high amplitudes in areas close to the chimney structure, which may indicate larger CO_2 accumulations at these locations.

Another possibility for migration of CO_2 upward the formation rather than being concentrated in the chimney structures, is that it migrates through the formation more laterally, where large amount of CO_2 is slowly migrating uniformly through the capping shale layers. To map out such possibilities there was obtained volume maps from the chaos datasets in the upper and lower part of the plume layers (i.e. volume taken from the middle of the negative reflections and up/down toward the reflection edges). This was obtained for the 2001 and 2006 datasets (figure 4.18). The maps were obtained over layer 2, 5 and 8 in order to see if there are any trends fixed to the lower, middle or upper part of the plume, and that these layers are of generally good continuity over the datasets. The figure reveals that the chimney can be observed on layer 5 and 8, but it falls out of the lateral extent of layer 2. There can generally be observed several areas with the same characteristics as for the chimney structure, where the layer boundaries are experiencing reflection terminations. This is interpreted as possible migration pathways for the CO_2. Another general trend observed is that the reflection termination is increasing with time, where there are several more areas in the 2006 dataset compared to the 2001, and that there are more reflection terminations in the upper boundary compared to the lower boundary of the layers. From these observations there was interpreted that the CO_2 is migrating more through the top of the layers with time, both through the existing chimney structures and through newly formed migration pathways.

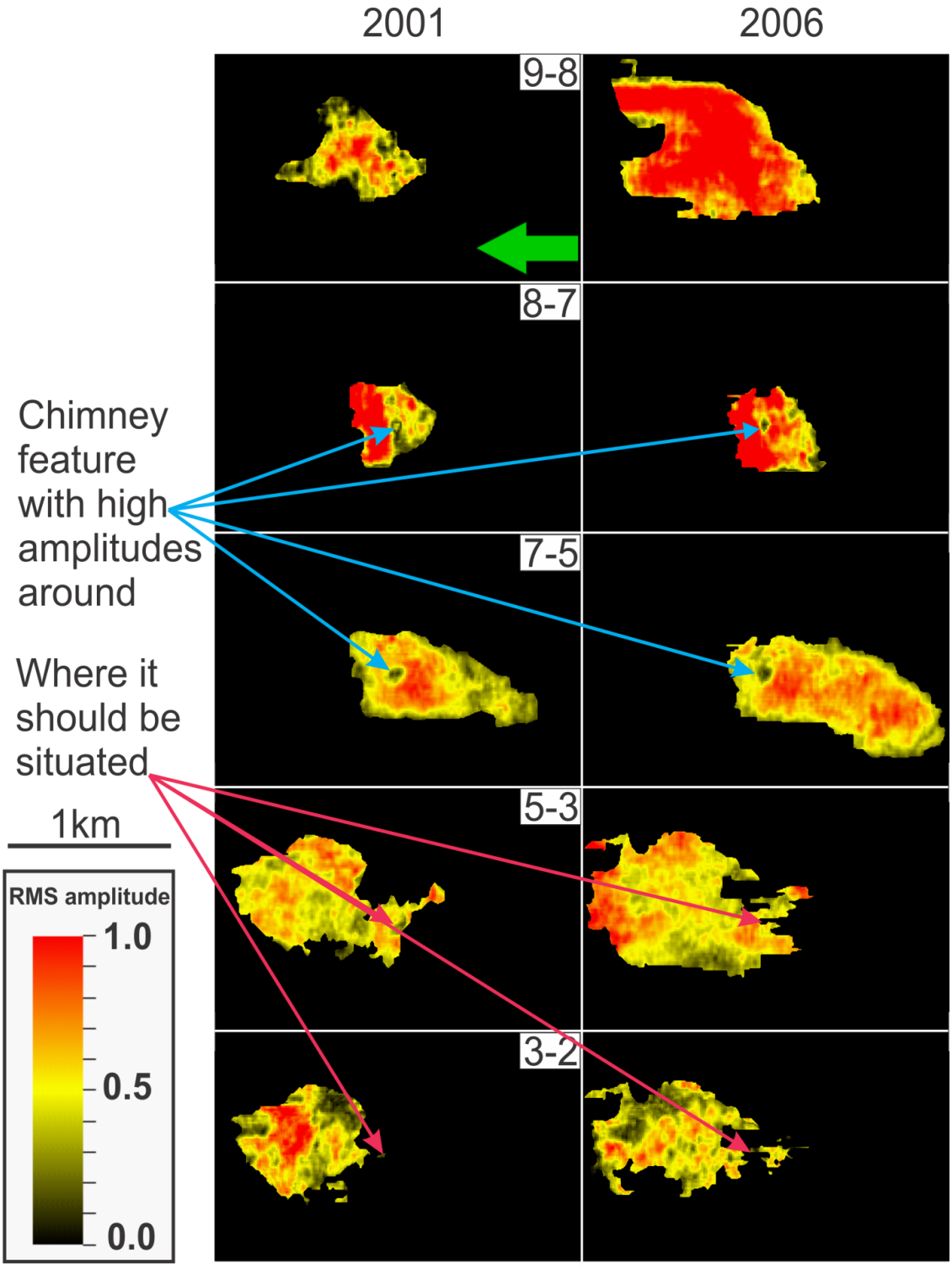

Figure 4.17: RMS amplitude map obtained between the mapped CO_2 layers for the 2001 and 2006 datasets. Because the layers are not situated perfectly over each other, it is constrained to the area where the two layers are overlapping. The blue arrows is indicating the area with little or no amplitude anomalies that are correlated with the chimney structure interpreted above. The red arrows are indicating the location of where the chimney structure should be situated, but seem to only be visible between the layers from layer 5 and up to layer 8.

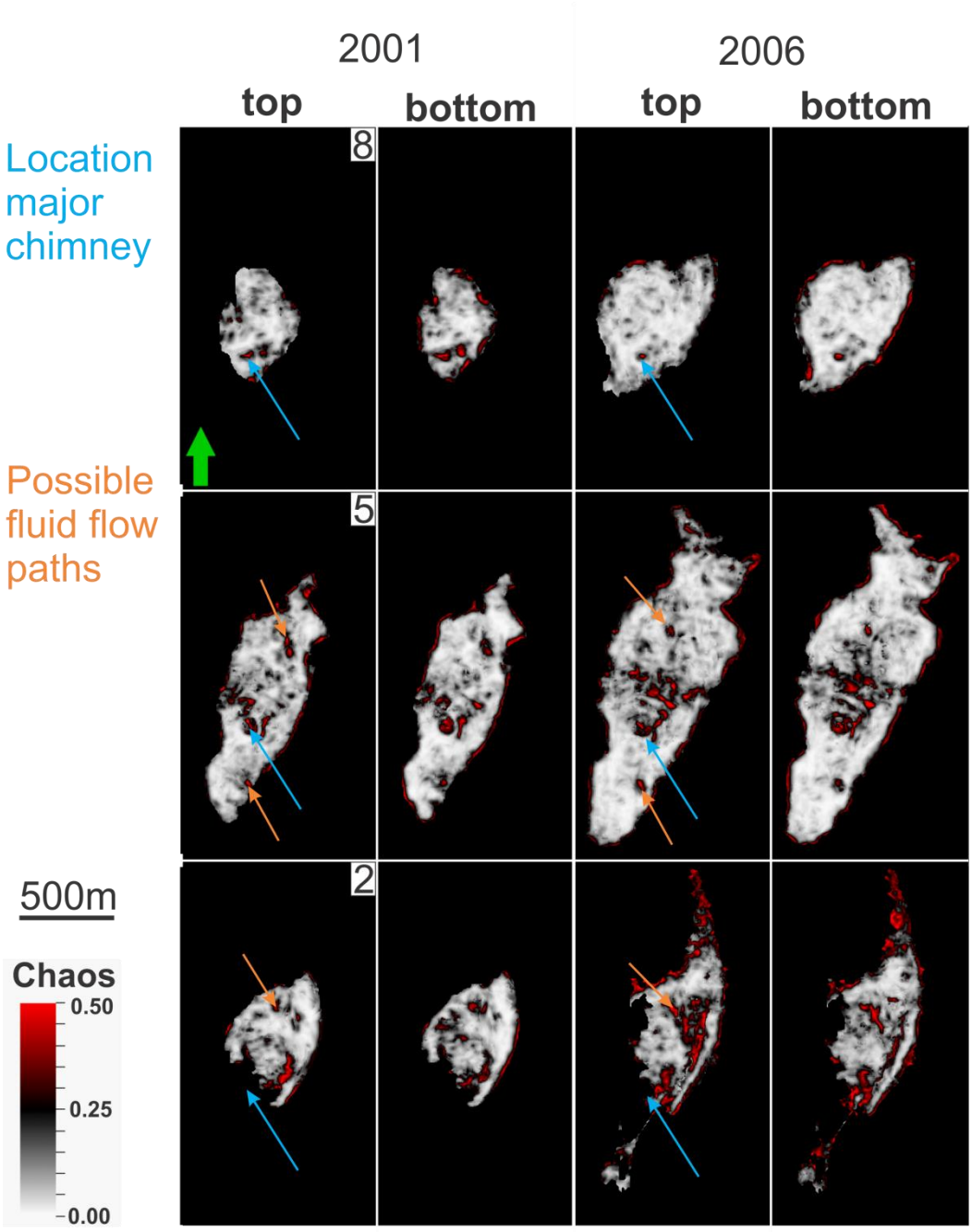

Figure 4.18: Chaos mapping of the upper and lower boundaries for layer 8, 5 and 2 obtained from the 2001 and 2006 datasets. Figure created in order to see if there are any changes on the chaos reflection pattern between the upper and lower boundaries of the CO_2 layers, and over time. The blue arrow is indicating refection termination caused by the chimney structure interpreted earlier. The orange arrow is indicating other areas where the reflection pattern is interrupted, which may be interpreted as fluid flow passages. The arrows are only been mapped on the top boundaries.

4.4.4 Velocity pushdown observed beneath the plume

Throughout the seismic post-injection datasets, there can be observed deformations and pushdown effects on the reflectors and boundaries situated beneath the CO_2 plume (figure 4.19). The deformations of the reflections are interpreted to be caused by the lower seismic velocities of the CO_2 saturated sandstones compared to the formation-fluid saturation, which will cause the seismic wave to spend more time traveling through the CO_2 column compared to the surrounding medium (Rob Arts et al., 2004a; F. C. Boait et al., 2012; Zweigel et al., 2004). Due to deformation of the seismic signal caused by the overlying CO_2 the horizons beneath was locally difficult to map, where there were more chaotic reflection patterns rather than good reflection patterns to follow.

There have been mapped out the pushdown on two horizons beneath the CO_2 plume, which are the Utsira base horizon and the Intra-Hordaland horizon (figure 4.19). Due to the different acquisition parameters, the interpretation of the two horizons beneath the plume was done by eliminating the baseline interpretation of the horizons inside a rough estimate of the lateral extent of the plume.

Since the pushdown of the underlying boundaries are interpreted to be a result from the presence of the injected CO_2 above, it was further interpreted that the amount of pushdown observed can be correlated in some way with the amount and distribution of the injected CO_2 located above. Combined changes in seismic amplitude and extent of each CO_2 accumulation horizons in the storage formation, as well as pushdown of sub-reservoir horizons, constrain the amount and distribution of CO_2 within the reservoir (F. C. Boait et al., 2012). On which the pushdown can be correlated with the amount of CO_2 is very dependent on how the CO_2 is distributed above, and are thus making calculations very complex (F. C. Boait et al., 2012; R.A. Chadwick, 2004b).

The pushdown are observed to be greatest at the center of the plume, where the pushdown value it calculated to be exceeding 30ms. Towards the edges of the plume, the pushdown values decreases. The pushdown values at the center of the plume is interpreted to be caused by either that the internal plume layers have CO_2 with greatest thickness in the center region, or that there is more free CO_2 between the layers around the center of the plume, or that it may be a combination of these two. From figure 4.12 one can observe that there are more CO_2 layers stacked on top of each other around the center, as well as the injection well is situated in the center region, which indicate that it probably will be a combination of more accumulated and free CO_2 around the center of the plume (F. C. Boait et al., 2012). This is also supported by the increase of reflection terminations of the internal CO_2 layers seen in figure 4.18. It can be observed that the lateral spread of the measured pushdown is very similar to the amplitude map generated for the whole storage reservoir, where it takes an elliptical shape with the longest axis in the NNE-SSW direction. The observed pushdown has a greater value interpreted over the Utsira base horizon compared to over the Intra-Hordaland reflector. This is interpreted to be a result of the processing work done on the datasets bringing the reflections up in areas beneath the CO_2 plume.

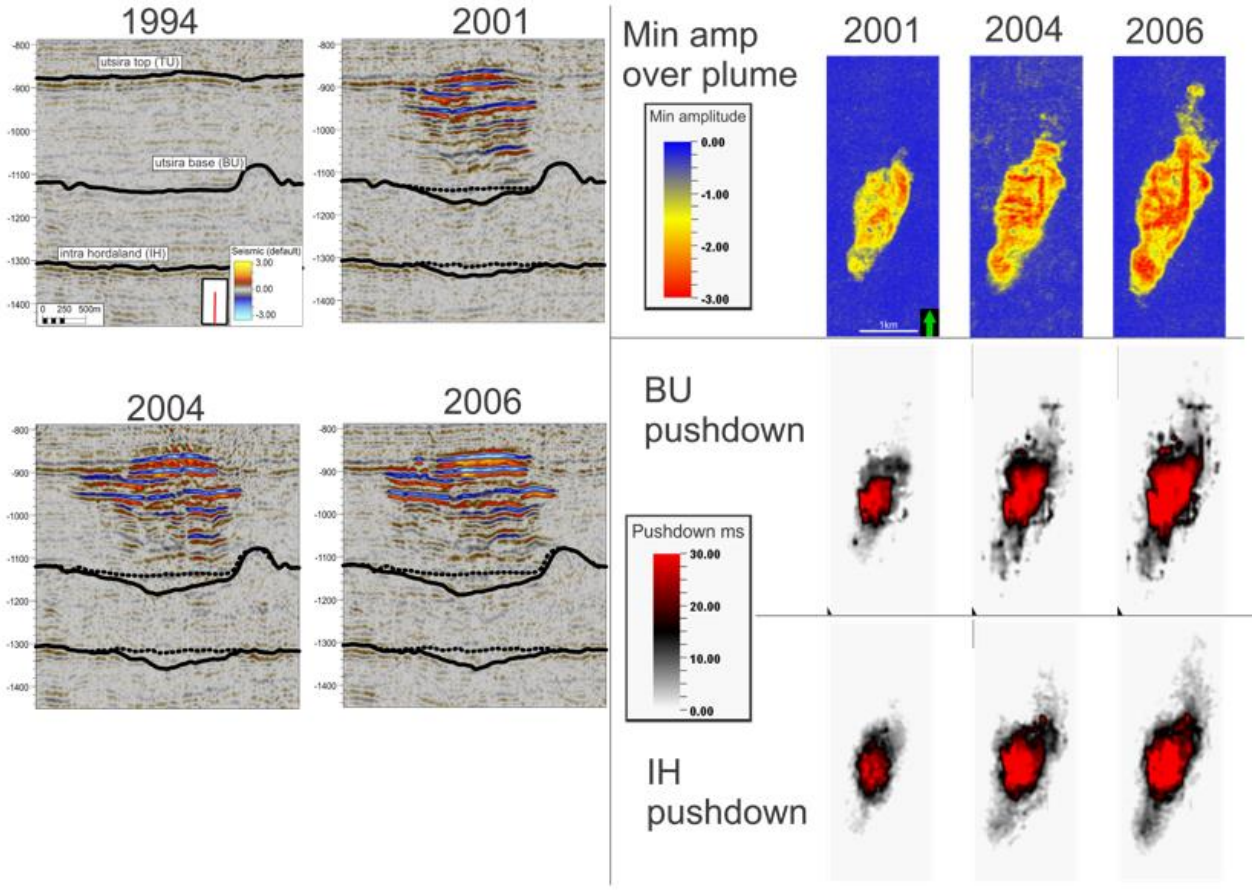

Figure 4.19: Observed pushdown beneath CO_2 plume. a) Seismic inline 1841 obtained from all the interpreted datasets. The 1994 dataset includes the interpreted horizons Utsira top (TU), Utsira base (BU) and Intra-Hordaland (IH). On the post-injection datasets there are interpreted new horizons for the underlying reflectors (solid line), with the 1994 interpretation included (dotted line). It can be observed that the solid lines are situated beneath the dotted line on the post-injection dataset, as a cause from velocity pushdown created by the injected CO_2. b) Minimum amplitude map obtained over the CO_2 plume within the storage reservoir (top). Pushdown observed on the Utsira base (middle) and Intra-Hordaland (bottom) horizons, where it can be observed the pushdown amount and correlation to the amplitude map from the injected CO_2. Figure is inspired of the work form (F. C. Boait et al., 2012)

4.4.5.1 Pushdown observed internally in the CO_2 plume

The pushdown effect observed beneath the CO_2 plume can also be seen internally inside the CO_2 plume accumulation, where the CO_2 layers mapped out from the 2001 dataset are situated above the same CO_2 layers mapped out on later surveys (figure 4.20a). This feature is responsible for making it rather difficult to do very detailed investigations within the datasets, as the layer is shifting position as more CO_2 is situated above. E.g., the subtracted cube taken from two post-injection datasets will experience noise obtained from both the differences in the acquisition parameters and the vertical pushdown caused by injected CO_2 in the formation.

The mapping of the internal velocity pushdown effect can only be best carried out by interpreting the thick shale each year, to see how the overlying CO_2 layer (layer 9) is pushing it down, since it is the only internal reflection that can be mapped on the pre-injection dataset. This is done, along with the thick CO_2 layer 5 in the middle of the plume (it is not possible to interpret this layer on the pre-injection dataset, but it is of relatively large lateral size and continuity on the post-injection datasets). The pushdown of layer 5 (figure 4.20b) is therefore taken over the post-injection datasets, whereas the pushdown of the thick shale (figure 4.20c) is taken with subtraction of the pre-injection dataset. The mapping of the pushdown on layer 5 are laterally constrained to the area of where the two comparative layers overlap (i.e. when comparing layer 5 from the 2006 dataset with layer 5 from the 2001 dataset, the only comparable surface is where the two layers overlap, which will usually be defined by the layer obtained from the earliest dataset). The figure that illustrate the pushdown of the thick shale have polygons for the overlying CO_2 to see how the layer is pushed down due to overlying CO_2.

The pushdown of CO_2 layer 5 is clearly seen, especially from the subtraction dataset 2006-2001, where the colored areas is indicating the amount of pushdown, and is exceeding 15ms of pushdown amount towards the edges. The pushdown obtained from the subtraction between the 2006 and 2004 dataset reveal, in contrast, few areas of pushdown. This is also observed on the seismic section (figure 4.20a), where the greatest vertical displacement is observed between the layers from 2001 to 2004, and the displacement between the layers from 2004 to 2006 is relatively short.

The pushdown of the thick shale layer can also be seen clearly in figure 4.20c. The pushdown is observed to be located in the central part and in the northbound thin “channel” of the included polygon, as well as outside the included polygon, where the pushdown value is exceeding 5ms. Pushdown may also be located outside the boundaries of layer 5, but because of the mentioned constrains, there is no reference point for comparable basis.

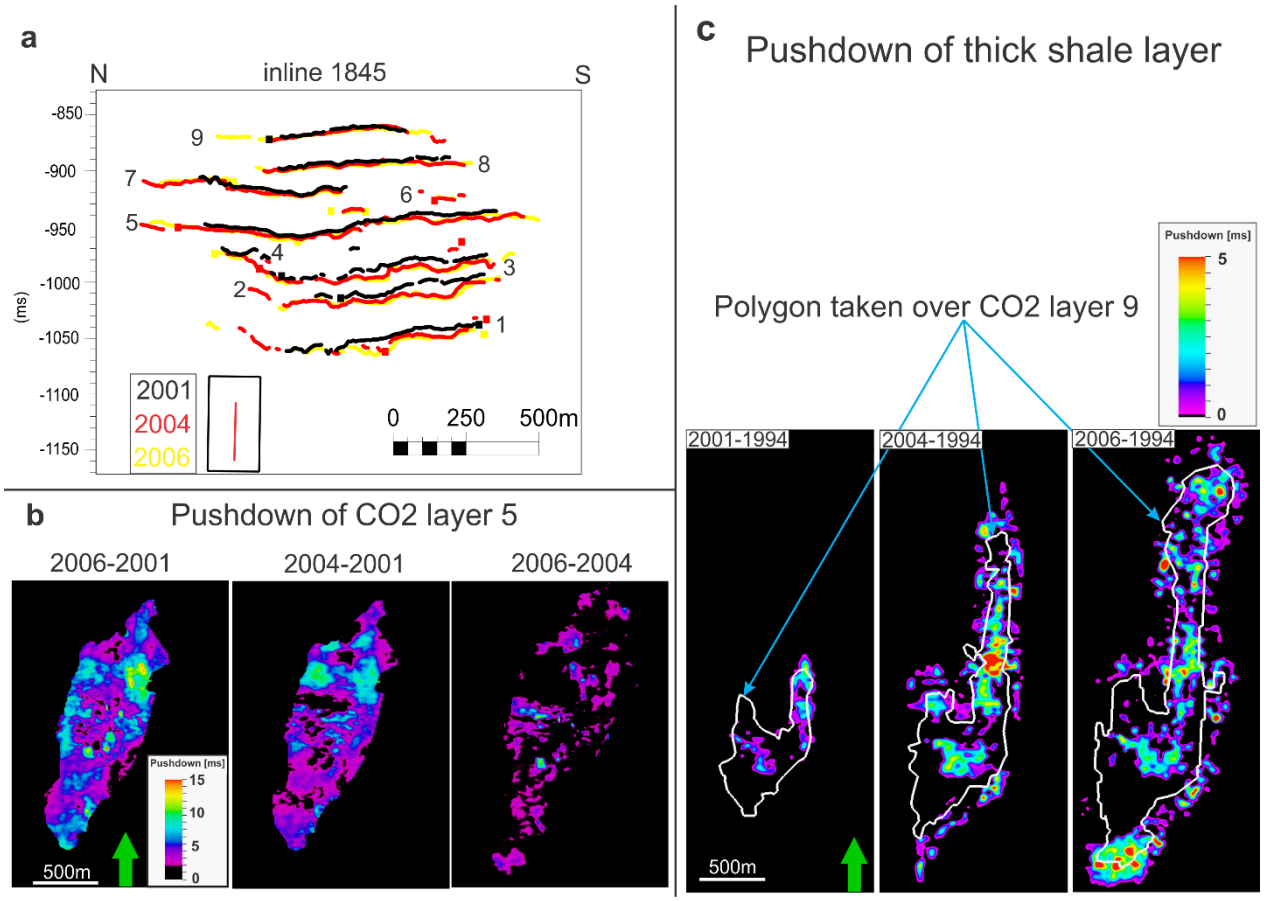

Figure 4.20: Mapping of the formations internal pushdown. a) Seismic inline 1845 with the interpreted internal CO_2 plume layers from the post-injection datasets, with the black lines referring to 2001, red lines referring to 2004 and yellow lines referring to 2006. b) Pushdown of layer 5 (position found in (a)), where it is mapped over the area where the two indicated datasets are overlapping. Pushdown measured to reach a value of up to 15ms. c) Pushdown of the thick shale horizon, situated below the topmost CO_2 layer (layer 9), where the polygon for the respectively years is indicated. Pushdown is observed to be found in the center of the polygon, northwards along the spread of the polygon and at the end of the polygon, with a measured pushdown value up to 5ms.

4.5 Observation concerning storage integrity

Some of the main reasons for having a good monitoring program for CCS projects is to observe how the injected CO_2 is behaving in the subsurface, and to make sure it will remain in the modelled and planned storage formation (Andy Chadwick et al., 2008). The use of time-lapse seismic is a good tool when we are supposed to map out the CO_2 in the subsurface, as the CO_2 has been shown to be highly visible on the seismic data, and any accumulation of CO_2 above the storage formation is expected to be detected. Previous in the chapter there was presented the importance of a good baseline survey for safety reasons, where features existing before the injection starts can be mapped out and ruled out whether it is developed as a consequence of CO_2 injection or not.

4.5.1 High amplitude anomalies observed in the caprock from the baseline data

Right above the Utsira storage formation it was observed high amplitude anomalies on the baseline dataset. The location of these anomalies was mapped out (figure 4.21). These amplitudes have a phase reversal wavelet compared to the seabed reflection, and was mapped out with the use of RMS amplitude maps as seen in figure 4.21 left. The high amplitudes is mainly observed at two locations on the survey, where they are found at the south side of the survey and at the north side, and are situated at approximately 40 – 50m above the Utsira top with a lateral extent in the range of 150 – 500m. Due to their phase reversal compared to the seabed reflection (figure 4.7), these high (negative) amplitudes are interpreted as bright spots. Bright spots may indicate presence of natural gas in the subsurface, since the natural gas has lower acoustic impedances compared with the original saline formation fluids (Andreassen, 2009; Loseth et al., 2009).

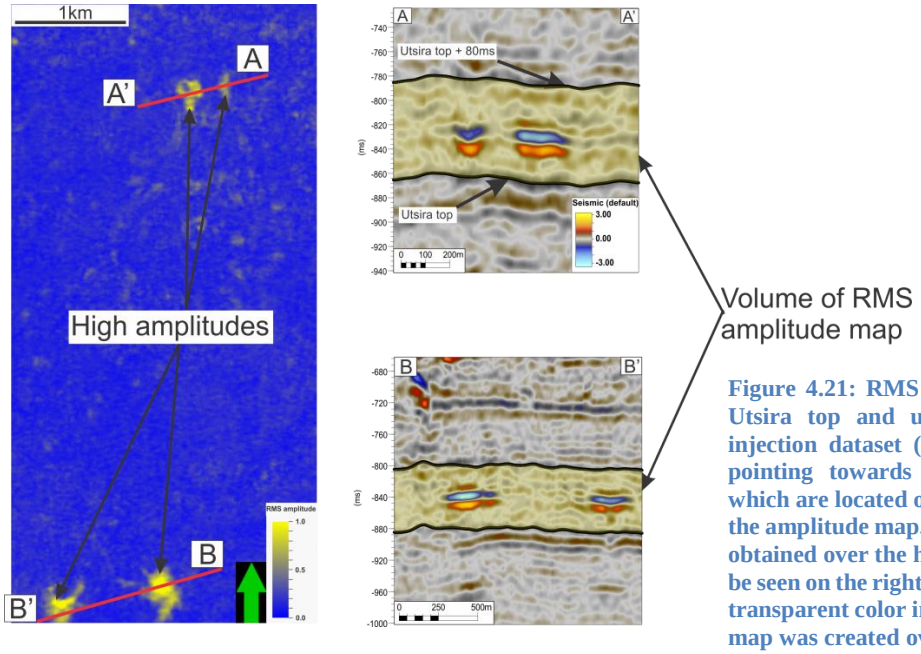

Figure 4.21: RMS amplitude map taken from Utsira top and up 80ms on the 1994 pre-injection dataset (left). The black arrows are pointing towards observed high amplitudes, which are located on the north and south end of the amplitude map. Seismic arbitrary lines were obtained over the high amplitude areas and can be seen on the right side of the figure. The yellow transparent color indicates the volume the RMS map was created over.

4.5.2 Interpretation of storage security based on observations from caprock and seabed changes

The high amplitudes interpreted as shallow gas in the last subsection are observed relatively close to the Utsira top. In order to examine this area more closely, there has been applied RMS amplitude maps over the subtracted seismic datasets to detect any changes of the high amplitudes. From these RMS amplitude maps (figure 22b) there can be observed signs of amplitude anomalies throughout the maps, which are interpreted to be noise caused be the different acquisition parameters from the seismic datasets that have been subtracted. The subtracted datasets are displayed in figure 4.22c, where it can be observed some reflection noise. Included in the figure is also the polygons indicating the maximum lateral spread of the plume in the respectively year, and there are no indication for more amplitude anomalies within these polygons compared to outside. It is interpreted that the seal is still intact, and is supported by (Eiken et al., 2011) where it has not been found any indications for CO_2 migrating upward through the caprock seal. The high amplitudes mapped in figure 4.21 cannot be observed in figure 4.22b, indicating that they are not growing with time such that they disappear when the later cubes are subtracted with the baseline.

When storing CO_2 subsurface formation there is important to monitor the seabed surface, especially for shallow storage formations as Utsira formation, in order to detect eventually disturbances as soon as possible (Andy Chadwick et al., 2008). Disturbances on the seabed can be caused by migration of CO_2 that have leaked from the storage formation and are flowing into the ocean, and the flow path through the caprock seal will not necessary be detected (discussed more in chapter 5). The seabed from the baseline dataset have already been interpreted (figure 4.7), and the seabed from the 2001 and 2006 dataset is included in the figure under (figure 4.22a). The later seabeds are observed to have several semi-circular depression spread out on the surface, which might indicate fluid flow (Loseth et al., 2009). The depressions are relatively small, with diameters of in the range 20-40m and depth in the range 8-10m. Considering the results from the pre-injection dataset, and keeping in mind that there is some differences on the acquisition parameters and the presence of seismic artefacts, the observed depressions were interpreted to not be showing any clear sign of growing, and is interpreted not to be caused by CO_2 leakage from the storage formation. The depressions also fall outside the polygon from the lateral spread of the CO_2 lying underneath.

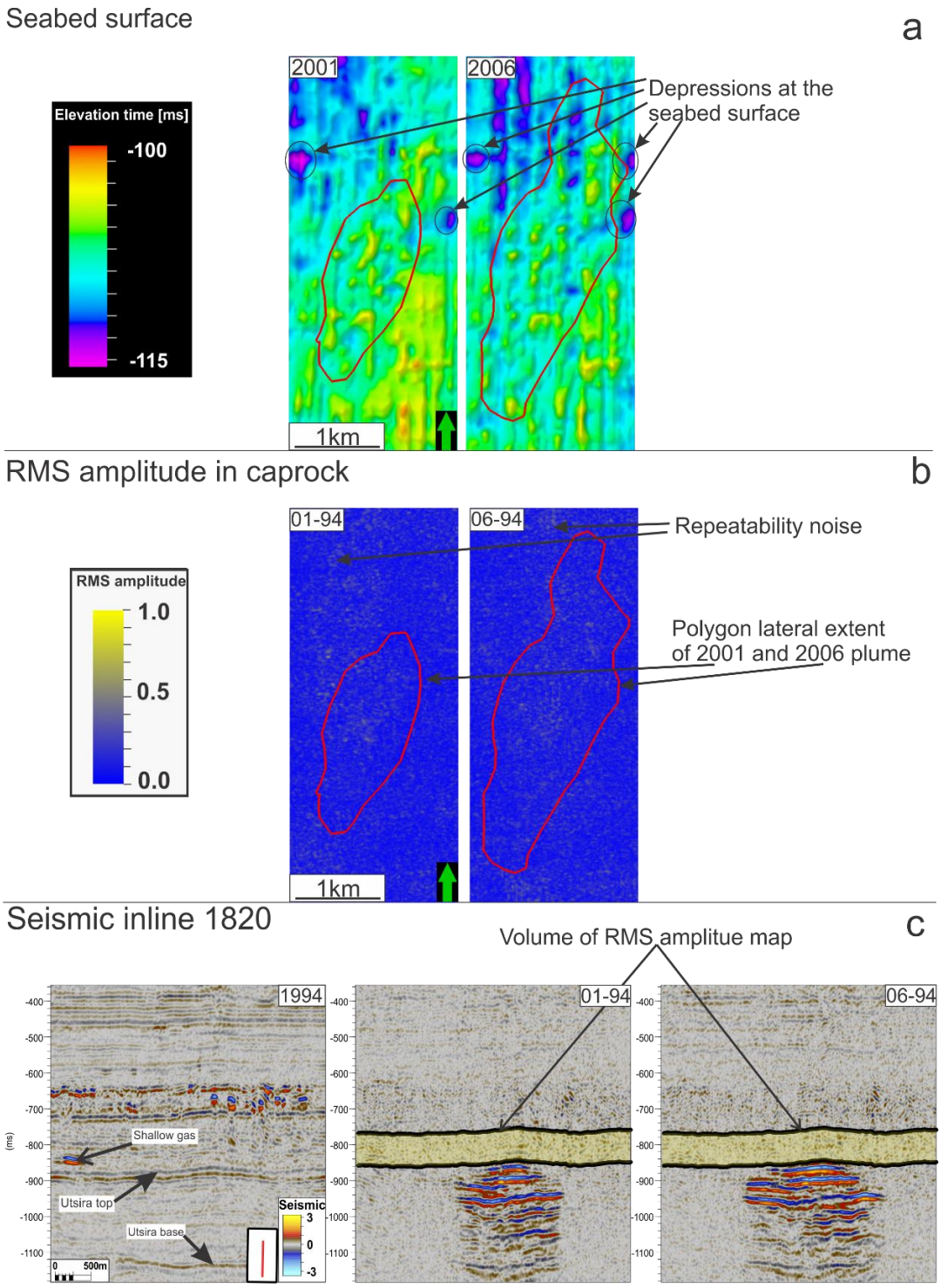

Figure 4.22: a) interpreted horizons obtained from dataset 2001 and 2006. Black arrows and circles are indicating observed depressions at the horizons. b) RMS maps created over the subtracted datasets. It can be observed small amplitude variation, interpreted as noise generated when the datasets was subtracted. The red polygons in (a) and (b) are the lateral extent of the plume at the respective years, which can be used to see if there is observed any differences within and outside. c) Seismic inline 1820 over the 1994 pre-injection dataset and subtracted datasets where the reflections from 1994 are removed. The yellow transparent color on the later datasets indicates the volume the RMS was obtained over. It can be observed some reflections caused by the different acquisition parameter, which are generating small amplitudes in (b)

5. Discussion

From the results in the previous chapter, it was observed that the injected CO_2 into the Utsira storage formation could be clearly seen on the seismic time-lapse data as relatively bright negative amplitude anomalies (illustration 1.1). The injected CO_2 was observed to be accumulating at nine distinct locations that could be followed in time, and was interpreted to be CO_2 accumulating under thin intra-reservoir shales (figure 5.1).

In this discussion there will be looked more closely on how, and why, the reflection amplitude anomalies obtained over each CO_2 layer differ over the years, and why the deeper parts of the storage formation is experiencing more reflection dimming compared to the shallower parts. An explanation for the elliptical spreading of the whole plume and the plume layers will be presented. In addition, there will also be discussed more on the storage security, and there will be presented a short outlook for the injection project.

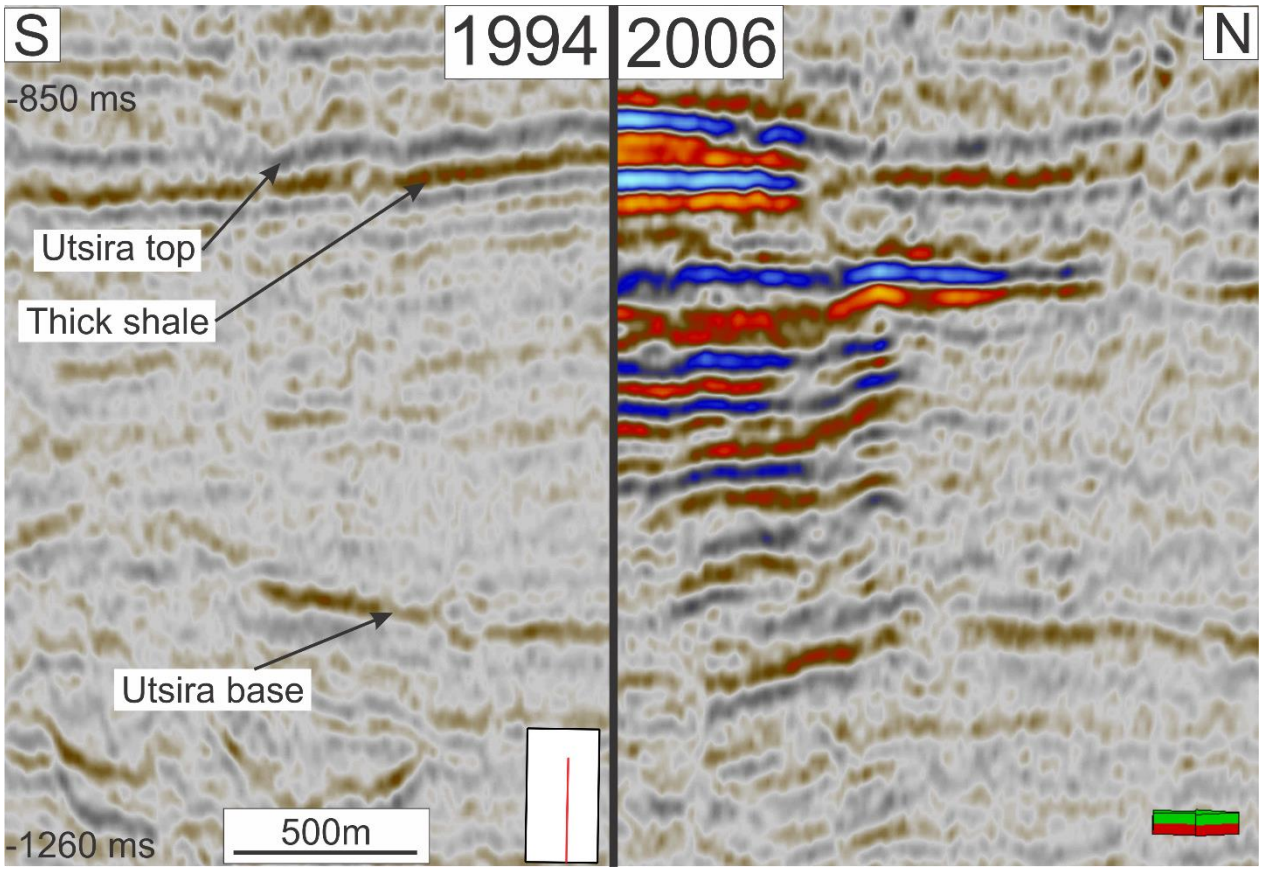

Illustration 5.1: Showing seismic inline 1857 over the storage reservoir. The figure is obtained from the Multivolume seismic attribute, where the left half is from the pre-injection dataset and the right half is from the 2006 dataset. It is possible to observe how the CO_2 is affecting the reflectivity inside the reservoir, where the bright amplitude is CO_2 accumulating throughout the right side of the transmission zone.

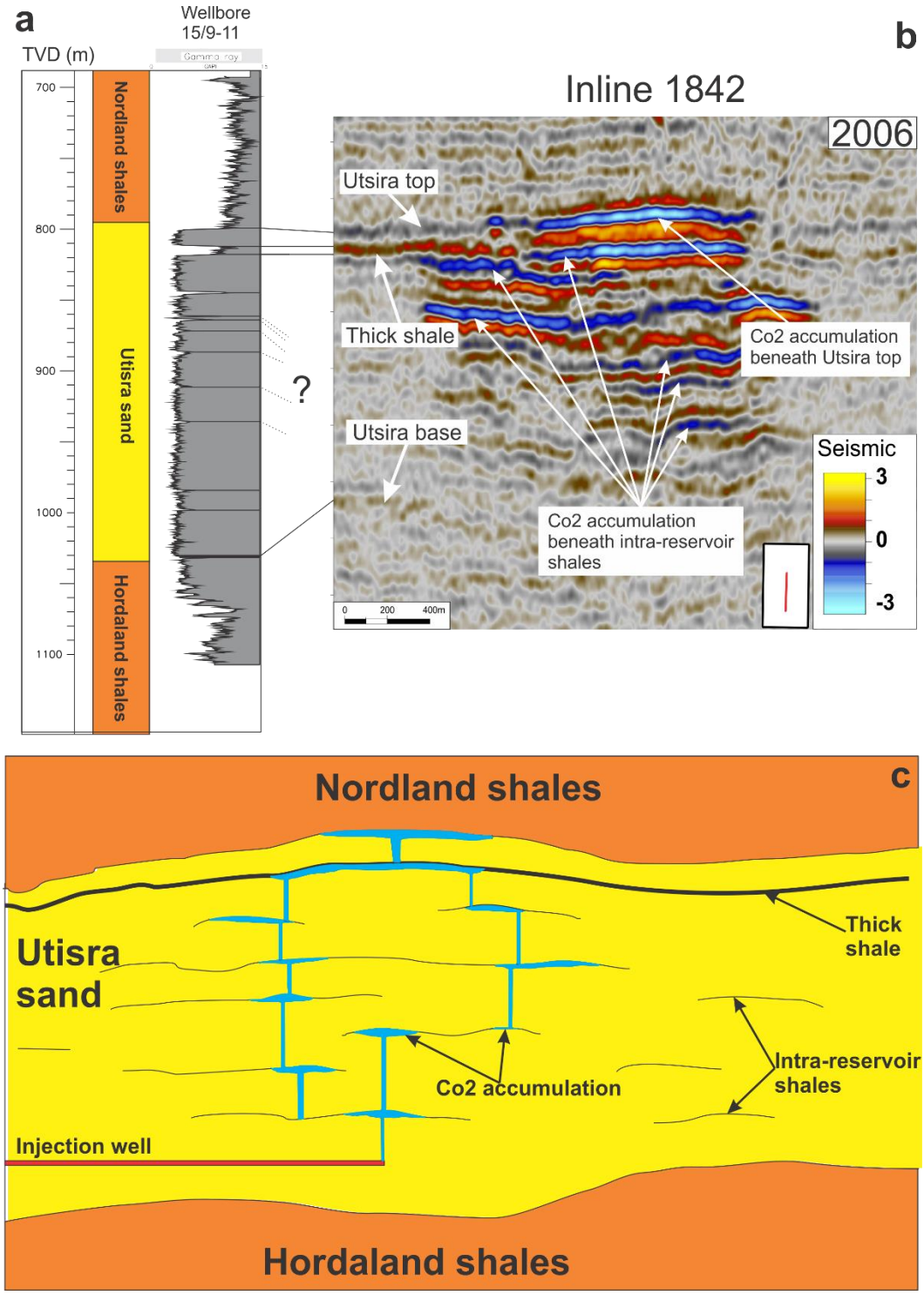

Figure 5.1: Overview figure of the injection of CO_2 in the Utsira storage formation. a) Well log from wellbore 15/9-11 penetrating the Utsira storage formation. The well log is modified from (NPD, 2014a), where the top, base and internal shale layers within the storage formation is indicated. b) Seismic inline 1842 obtained over the 2006 dataset, where the CO_2 accumulation and horizons are indicated. The seismic section is correlated with the well log from (a). c) Schematic drawing of the storage reservoir, where the injected CO_2 is seen migrating upwards from the injection well and accumulating under the intra-reservoir shale layers and at Utsira top. The figure is only to be used as an approximated overview and the actual situation is far more complex.

5.1 Distribution of CO_2 in the storage formation

5.1.1 CO_2 plume growth and reflection amplitude variations

From the results in chapter 4 the injected CO_2 was easily seen on the post-injection seismic datasets (figure 4.10a), where the CO_2 was mapped out as bright negative amplitude anomalies that differed from the baseline seismic dataset. The injected CO_2 was observed to both be laterally spreading within the reservoir and be accumulating in the central parts. The amplitude maps generated over the entire storage formation for each interpreted datasets, which indicated an amplitude increase both over the central part of the plume and an amplitude-spreading (figure 4.10b), supported this observation. There could be observed a general trend of the plume from the RMS amplitude map, where the first post-injection dataset indicating an elliptical form of the CO_2 plume with the long axis in the NNE-SSW direction and the short axis in the WNW-SES direction. This elliptical form of the plume became even more prominent on the next datasets. The eccentricity (relationship between the long and short axis) over the elliptical shape of the entire plume grew from 2.5 in 2001 to over 5.5 in 2006. Most of the growth of the long axis in the latest dataset was interpreted to be caused by the major growth of the topmost reflection, which had spread northwards with a relative large amount of CO_2.

Internally in the storage reservoir, the CO_2 was observed to be accumulating at certain location that remained approximately constant with the time. The CO_2 was observed to be accumulating at nine distinct layers, with the two topmost accumulations are CO_2 that were trapped beneath the Utsira top, and the thick shale (thickness of approximately 5-6m) located 15-20ms below the Utsira top, which is referred to as layer 9 and 8 respectively. The seven other accumulations were interpreted to be CO_2 trapped beneath small intra-reservoir shale layer (thickness of approximately 1m). These shale layers could not be mapped from the seismic datasets, but could be observed on the well logs (chapter 2 and figure 5.1). Several others support this interpretation (R.A. Chadwick, 2004b; Zweigel et al., 2004). The internal CO_2 plume layers are referred with number 1 as the shallowest observed accumulation of CO_2, to number 9 as the topmost observed accumulation of CO_2 beneath Utsira top. All the 27 (9x3) CO_2 layers from the three post-injection dataset were mapped using the minimum amplitude attribute (figure 4.12), where the evolution of the reflection amplitudes could be followed in time.

The reflection amplitude from the 2001 dataset was made as a reference point, and the changes in reflection pattern was correlated with that reference point. The first general trend that could be observed was the difference between the layer growth for the upper layers (layer 5-9) and for the lower layers (layer 1-4). This was mapped out (figure 5.2) where it clearly shows how the upper layers are growing in both reflection amplitude and in lateral spreading, whereas the lower layers are showing clear signs of reduction in both the reflection amplitude and continuity.

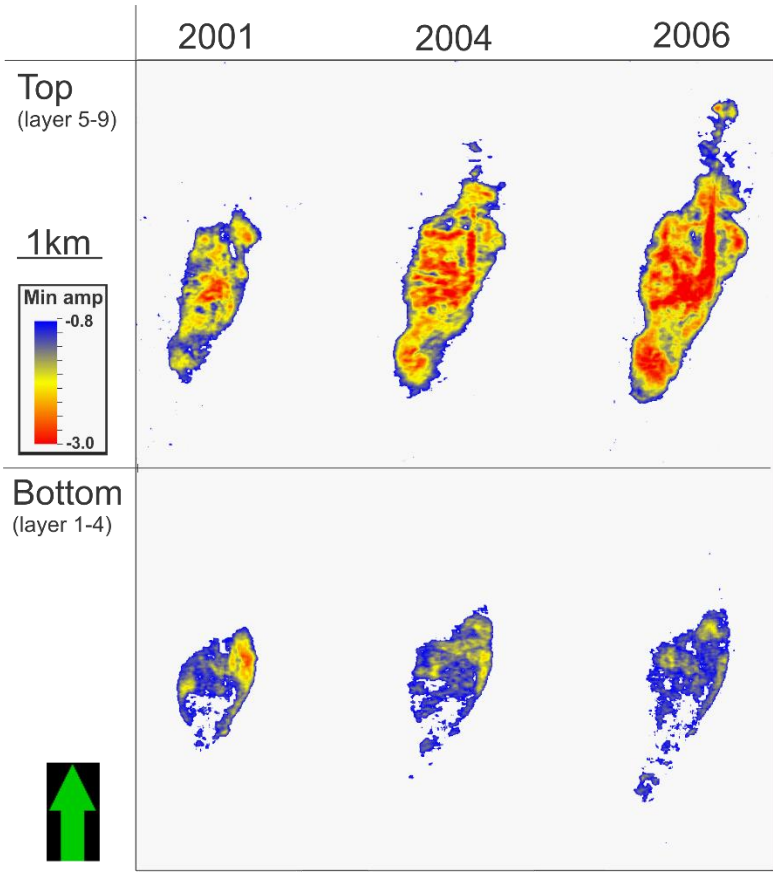

Figure 5.2: Minimum amplitude maps obtained over all three post-injection surveys, and separated into the top part and the bottom part of the plume. The top maps are including all the layers 5-9, whereas the bottom maps are including all layer 1-4. Warmer and colder colors indicate stronger and weaker reflection amplitudes, respectively. The top layers have a trend of increasing in wormer colors, and the bottom layers have a trend of colder colors and loss of reflection continuity.

The internal CO_2 layers from figure 4.12 shows that there are several changes on the reflection amplitudes, reflection continuity, and lateral reflection spread. Some of the internal CO_2 layers are observed to be growing in time (especially layer 5, 6, 8 and 9), some layers are observed to be stopping to grow (layer 3 and 7), whereas some layers is observed to be reducing in reflection amplitude (layer 1, 2, 4 and 6). The growth of each individual internal layer can be seen as a three-stage growth model (Bickle et al., 2007; F. Boait et al., 2011; F. C. Boait et al., 2012). The first stage of the sequence is the growth in lateral direction of the layer, which happens at a relatively high speed, and induces a bright reflection as the wavelet is reflected by the CO_2 instead of the normal formation fluids. The second part of the sequence is characterized by a more slowly growth of the layer, and the reflection in the center are dimming while the amplitude at the sides may continue to brighten. This is followed by the third part, where the growth of the layer seems to be stopping and, in some instance, it shrinks and overall amplitudes dims.

The behavior of the internal CO_2 layers and the change of amplitude strength can be explained in several different ways, but all the explanations must cause a change in either reflection coefficient or signal strength (F. Boait et al., 2011; F. C. Boait et al., 2012). The first explanation, and perhaps the most obvious, is that the indicated decrease in reflection amplitude in the lower layers are simply that these layers are leaking CO_2 into the overlying layers due to more permeable migration zones created by the continuous injected CO_2 (Bickle et al., 2007). This will cause the accumulated CO_2 layers beneath the intra-reservoir shales to experience a shrinkage of thickness and therefore induce a lower reflection amplitude.

The signal strength reduction (i.e. reduction of transmitting energy for the reflection wave) can be caused by that the migration of fluids within the storage formation is altering in time, where perhaps more CO_2 is migrating upward in the center of the plume through several small chimney structures that cannot be indicated on the seismic datasets (F. Boait et al., 2011; F. C. Boait et al., 2012). This migration of fluids (which can be migration of the injected CO_2 or migration of the formation fluids that are pushed by the injected CO_2) can be encountered by the seismic wave, which causes a drop in its acoustic transmission energy, and thus leaving the seismic energies to be reduced as it reaches the lower levels of the plume. The amplitude loss in the central parts of the CO_2 layers, as seen in figure 4.12 (especially seen on layer 5), might be caused by this effect. As the migration of CO_2 is interpreted to take place around the middle of the plume, where the pressure caused by the injection well is expected to be greatest, support the possibility of more free CO_2 in this region (F. C. Boait et al., 2012). The migration of CO_2 in the storage formation and its possible effect of the CO_2 dimming will be discussed more in detail in subsection 5.1.3.

Furthermore, the loss of signal strength on the lower layers may also be caused by the increase of high amplitudes in the top CO_2 layers within the storage formation (F. C. Boait et al., 2012). From figures 4.12, 4.14 and 4.15 it is evident that the two topmost layers (layer 8 and 9) are experiencing a growth in lateral extent (mostly for layer 9) and in reflection amplitude. This increase of reflection amplitudes will take up more energy from the penetrating seismic waves, and thus leaving less energy for the shallower CO_2 layers. In order to see more clearly on the effect the two topmost layers have on the shallower layers, it was mapped out layer 5 with indicated polygons of the two topmost layers (figure 5.3). It can be observed that layer 5 have weaker reflection amplitudes when the two upper reflections is situated right above (figure 5.3a). This is even better seen from the minimum amplitude maps, where the reflection of layer 5 is seen to be experiencing dimming at the area where the two topmost CO_2 layers are overlapping (figure 5.3b).

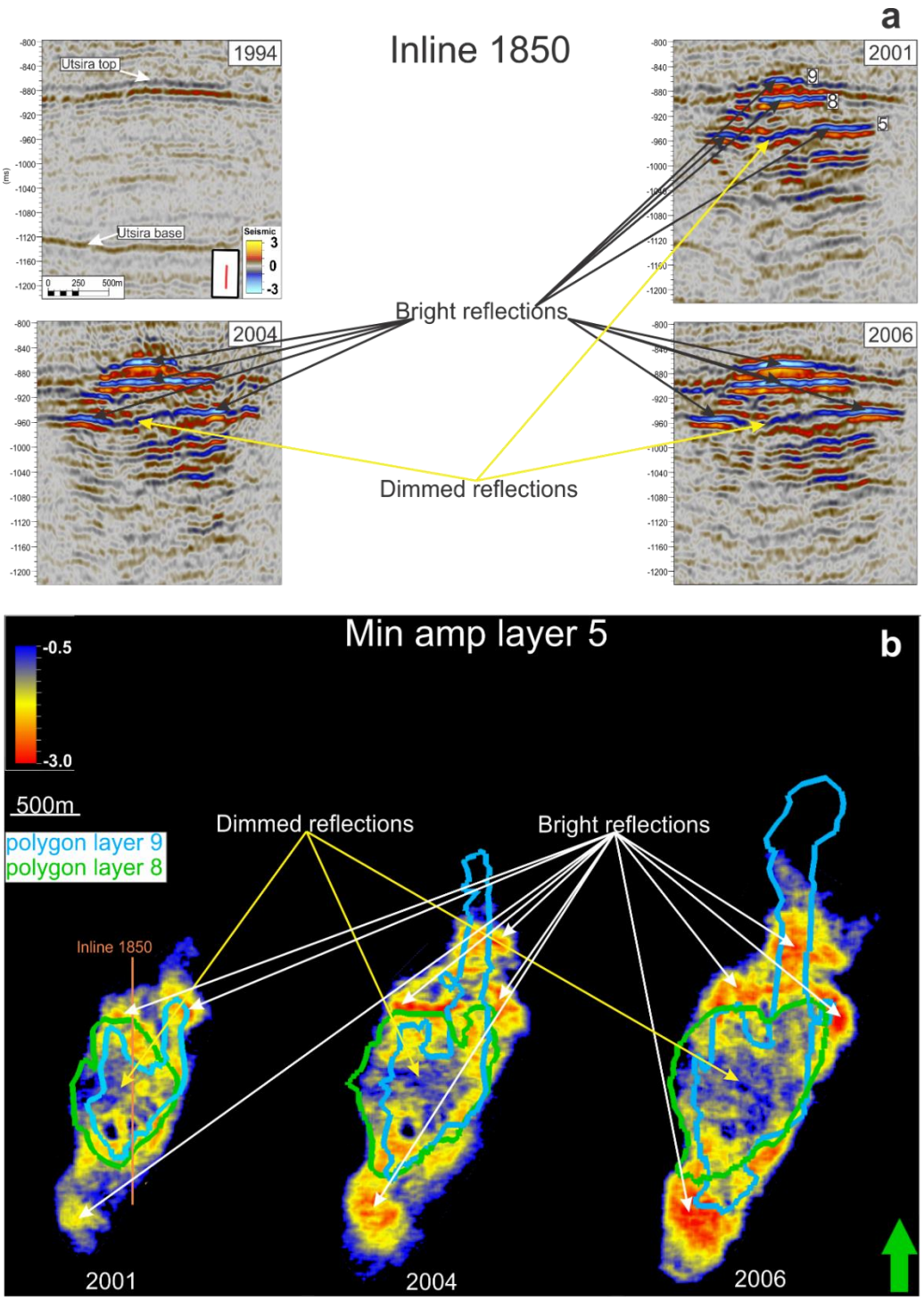

Figure 5.3: Showing a possible explanation for the dimming effect on the amplitude anomaly seen at the center of layer 5. a) Seismic inline 1850 obtained over all the interpreted time-lapse datasets, where bright and dimmed reflections are indicated with black and yellow arrows on the post-injection datasets, respectively. Location of the Utsira top and Utsira base reflection is indicated on the pre-injection baseline. b) Minimum amplitude map obtained over the CO_2 layer 5, with indicated lateral spread of the two topmost CO_2 layers (layer 8 and 9). Bright and dimmed reflections are indicated with white and yellow arrows respectively, and where it can be observed that the dimmed reflection is situated approximately where the polygons for layer 8 and 9 overlaps.

Since the reflection amplitude generated from the accumulation of CO_2 is affected by the amount and thickness of both the CO_2 layer and the capping layer (as explained in chapter 4.3.2), the dimming of the lower layers may be caused by changes in CO_2 thickness and saturation. The instinct effect is mainly caused by the change in fluid composition in the Utsira reservoir, where the acoustic impedance is strongly sensitive to CO_2 saturation of <30% or so (F. Boait et al., 2011). The reflection coefficient can be changing into a lower value by either an increase or decrease in CO_2 thickness and saturation, away from the tuning thickness. Although the reflection amplitude increase of the topmost layer was interpreted to be caused by increase in CO_2 accumulation (section 4.4.2.1), leaving it rather unlikely that the dimming of the lower CO_2 is caused by an increase of CO_2 saturation or thickness.

The dimming in amplitude anomalies for the lower CO_2 layers can also be caused from changes in the saturation and pressure of the pore-space as the injected fluid displaces the original formation fluid (Dudfield & Woods, 2013). Higher pressures in a local region can cause the seismic signal to lose energy and scattering of the waves, and thereby leaving less energy to be transmitted and used for mapping of the lower levels. However, the high permeable sandstones and discontinuous shale layers in the Utsira storage reservoir are not expected to have a drastic increase in pressure caused by the CO_2 injection (Andy Chadwick et al., 2008; Dudfield & Woods, 2013; Eiken et al., 2011).

The continuity of the CO_2 have also been observed to be different, where the layers 3, 5, 7-9 are observed to be highly coherent and seem to stay as continuous amplitude anomalies, whereas the layers 1, 2, 4 and 6 are observed to evolve into more patchy amplitude anomalies. This can be caused by two main effect. The first effect is that the CO_2 have migrated into or through the capping layers at the area where it loses reflection amplitude, and can only be mapped on the areas where there still is accumulated CO_2 beneath a capping layer. The second effect is that the CO_2 is experiencing a different pressure regime with time, where maybe the developing of migration routes and chimneys reduces some of the pressures around the lower CO_2 layers. The possible lower pressures in the layers will induce more topographical flow of the CO_2, which will flow to the nearest topographical heights, and thus lose reflectivity over areas with the topographical lows.

5.1.2 Origin of the elliptical shape observed for the CO_2 plume

From the mapping of the plume in chapter 4 there could be observed a trend for it lateral distribution, both on the whole plume (figure 4.10b) and for the internal CO_2 layers (figure 4.12). The CO_2 plume was observed to be spreading in an elliptical shape with its long axis in the NNE-SSW direction and the short axis in the WNW-ESE direction with eccentricities for the internal layers observed to be between 2.5 and 4.5.

The trend of the CO_2 being spreading in an elliptical shape can be controlled by a number of geological controls (Bickle et al., 2007), which may reflect either layer seal topography or anisotropic reservoir permeabilities in form of faults or sedimentary channels separating local permeability differences.

Since there have not been observed any faults or sedimentary channels within the storage unit (Zweigel et al., 2004), the most probable explanation for the elliptical trend for the injected CO_2 is that they are following the topography of the capping intra-reservoir layers. Because the actual shape of the intra-reservoir shales is not accurately known, the mechanism that provide trapping of CO_2 underneath will neither be certain known (Hermanrud et al., 2009). The shape of the shale layers were determined by the underlying sands, and the deposition of these sand layers would differ, which indicate different topography of each shale layer (Hermanrud et al., 2009).

The two horizons in the storage formation that can be mapped on the pre-injection dataset are the Utsira top and the thick shale right underneath. They seem to have almost the same topography (figure 4.4 & 4.5), which can be correlated with the Utsira base. From chapter 2 it was mentioned that the underlying Hordaland shales probably was affected by soft-sediment mobilization that created dome/diapir structures on the Utsira base (figure 4.6) (Gregersen et al., 1997; Zweigel et al., 2004). When the Utsira storage formation was overlain with sediments during burial, it experienced compaction due to the overlying weight, and it may be expected more compaction over the regions with the diapir structures due to its more muddy content, which may have been the explanation for the domal trap formation at the Utsira top (Gregersen et al., 1997; Zweigel et al., 2004) (figure 5.4b). If it is assumed that all the intra-reservoir shale layers have approximately the same topography as the two topmost horizons (that the dominant mechanism for determining the topography for the intra-reservoir shales are the relatively larger compaction of the underlying dome structures), the lateral spreading of the CO_2 can be explained.

In order to map this possibility, the horizons from the two largest CO_2 layers (layer 5 and 9) were mapped (figure 5.4a). Polygons were drawn from the lateral extent of the layers and applied to the topographies of the Utsira base (layer 5) and Utsira top (layer9) (figure 5.4c). Layer 5 is used since it is situated in the middle of the plume, and that it have the largest lateral extent of the internal CO_2 layers. The layer is situated such that the other layers are overlapping (except for layer 9, which is mapped separately). As observed in figure 5.4c, the polygons from the lateral extent of CO_2 layer 5 seems to be concentrated where the Utsira base have its shallowest topography, and seems to avoid spreading over the relatively high dome structures. Layer 9 is observed to follow

the capping topography, where it is accumulating under the shallowest part of the Utsira top. It may therefore be assumed that the internal CO_2 layers also will follow the capping topographies, which may have been formed due to the local compressions of the underlying Hordaland shales. From figure 5.4c (right), it can be observed how the lateral spread of layer 5 is dominant in the NE-SW direction, and seem to be following the troughs of the base horizon. The lateral spreading in the NW-SE direction seems to be stopping due to encountering the relatively high dome structures, which might be the explanation for the reduction in the observed amplitude anomalies for the whole CO_2 plume and the internal CO_2 layers in this direction.

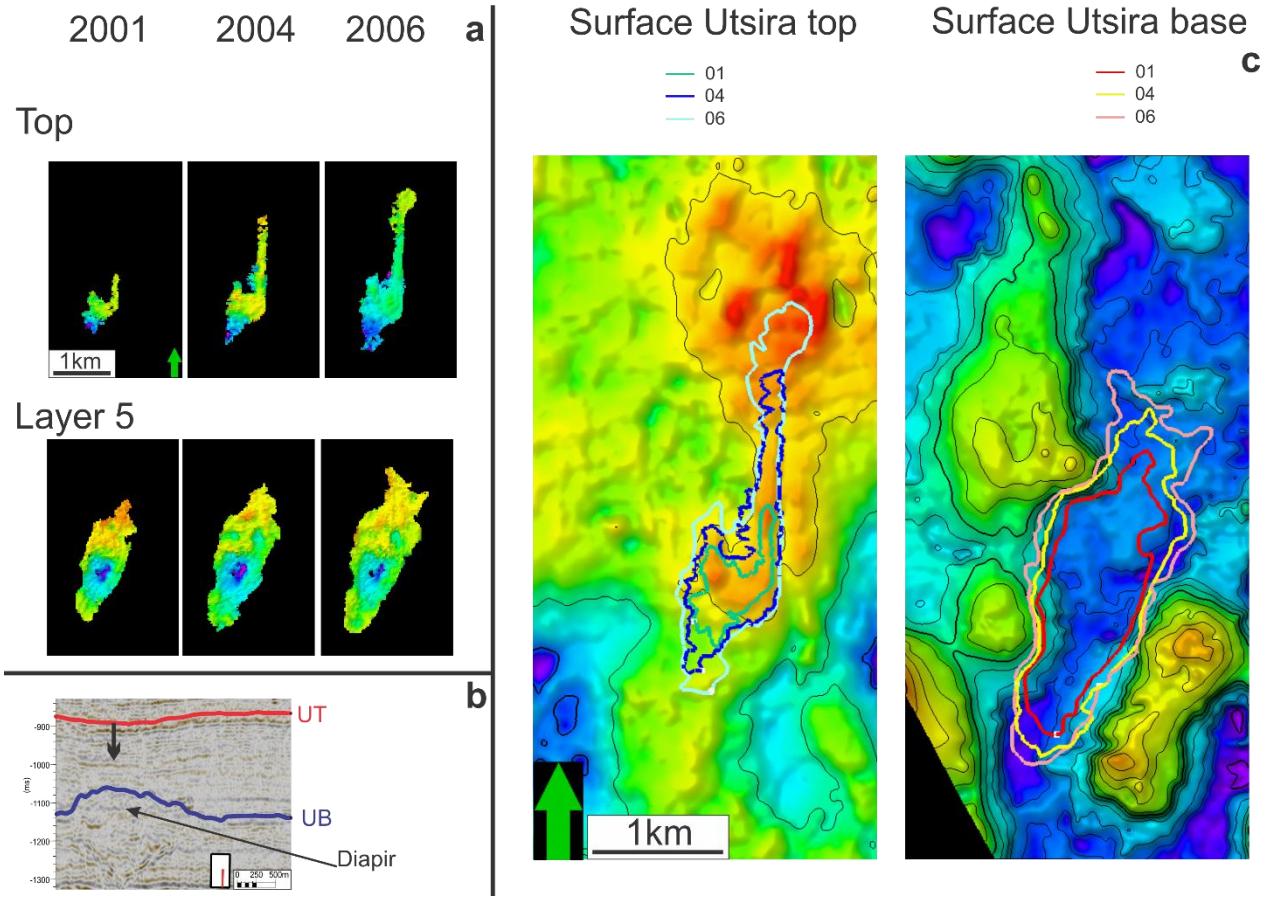

Figure 5.4: Illustration of the possible correlation between the Utsira top and base, with the plume distribution. a) Interpreted horizons of the topmost (layer 9) and middle (layer5) internal CO_2 layers for all the post-injection dataset. b) Seismic inline 1875 obtained from the pre-injection dataset. Utsira top and base is indicated, as well as the diapir feature at the base, with indicated downshifted reflectors above. c) Surfaces for the Utsira top horizon (left) with indicated lateral distribution of CO_2 layer 9, where it can be observed that the CO_2 is accumulating in the shallowest areas. Surface from the Utsira base horizons (right) with indicated lateral distribution of CO_2 layer 5, where it can be observed how the spreading is concentrated in the NE-SW direction and it does not seem to be CO_2 accumulating over the relatively high locations of the base structure.

5.1.3 Vertical CO_2 migration

From the seismic time-lapse data, the CO_2 was observed to have reached the Utsira top seal already by the first post-injection dataset in 2001 (figure 4.10a). The injection well is situated close to the Utsira base, in order to have the best migration options as possible (R. A. Chadwick et al., 2004a), which indicate that the CO_2 have migrated upward from the formation base to the Utsira top. The reservoir itself consists of an interbedded stack of sandstone and shale layers, which have thicknesses of between 10 and 40m and 1-2m, respectively (F. C. Boait et al., 2012). The CO_2 have, in other words, migrated through all the internal sand packages and the shale layers. Lighter fluids in the subsurface has long been known to penetrate the relatively permeable layers, using only pressure created by density differences (Rafaelsen, 2013; Selley, 1998).

From the post-injection seismic time-lapse data, it could be observed a vertical feature situated close to the center of the CO_2 plume (figure 4.16), which was interpreted to be a chimney that transporting CO_2 upward the formation. This single main feeder chimney has been proposed as responsible for most the upward flux of CO_2 through the reservoir (Andy Chadwick et al., 2006a). Since the feature could not be observed on the pre-injection dataset, and that it was located close to the injection well, it was interpreted to be formed as an effect of injected CO_2. This chimney suggest that the intra-reservoir shale layers all are broken almost at the same area (Hermanrud et al., 2009). Two phenomena act to retard the rate of CO_2 penetrating through the thin mudstones (F. C. Boait et al., 2012). Where the first phenomenon is the pressure caused by underlying, and pounding, CO_2 accumulation that is acting on the thin intra-reservoir shale layer. This pressure is relative to the amount of underlying CO_2 column and the pressure regime. The second phenomenon is the rate of formation fluid push-through rate of the shale layer (i.e. capillary force) and thickness of the relatively shale layer. This will determine how much the pressure beneath the shale layer have to be before the formation fluid is pushed out and replaced by CO_2. It can be interpreted that the chimney have been formed due to the presence of the injected CO_2, possible because of mechanical instabilities (liquefaction and fluidization) as a response of concentrated CO_2 accumulating at certain local areas, and where it can probably have dissolute some of the carbonate matrix in the shales due to high CO_2 consecrations (R.A. Chadwick, 2004b; Hermanrud et al., 2009; Selley, 1998). There is also, however, possible that this chimney is formed by small faults or fractures within the reservoir, with just enough vertical displacement for fluids to flow through. These small faults or fractions may not be observed on the seismic data due to sizes lower than the resolution limit (R.A. Chadwick, 2004b). Alternatively, it may be a combination of the mentioned possibilities. The Pliocene depositional environment of the Utsira formation, which are of relatively high frequencies, may support possibilities of small fractions or faults within the formation (Gregersen et al., 1997).

The relatively enormous increase in CO_2 flux at the topmost CO_2 layer (layer 9) (from 40000 tons CO_2 by 2001, to 140000 tons CO_2 by 2004 and to 350000 tons CO_2 by 2006) indicate that the injected CO_2 are finding a more a direct way upwards the storage formation (R. A. Chadwick et al., 2009). This increase in net input may come from that vertical migration pathways are increasing

in sizes and number, giving a more permeable migration routes for the injected CO_2 to migrate from the injection well.

Since the mapped vertical chimney does not seem to be included in all the internal CO_2 layers (especially layer 6), it is therefore not very realistic that the major chimney is solely responsible for vertical migration of CO_2 upward the formation. Some of the plume layers were mapped in their top and bottom part (figure 4.18), which indicated several other possible migration pathways for the CO_2, as reflection amplitudes were observed to have the same characteristics as the major chimney. These characteristics were seen growing larger in both numbers and sizes, indicating that more CO_2 might be migrating through the layers from several more locations with time.

Another observation made was in the areas between the internal CO_2 layers (figure 4.17), where the major chimney could be observed from layer 5 and up to layer 8. The mapping of the layers below have indicated amplitude anomalies right beside where the chimney structure should be located. This feature can also be seen from the minimum amplitude anomalies taken over the internal CO_2 layers (figure 4.12), where the chimney structure is marked on the CO_2 layer 5, and can be correlated with other layers that covers that area. This can indicate that the intra-reservoir shales in the lower part of the storage formation is dipping (figure 5.5), and that the flow of CO_2 from the chimney are not thick enough to produce a seismic reflection close to the chimney. There can be observed a general trend of high amplitude anomalies at the north side of the major chimney structure for the deeper layers, which may indicate a general southward dip of the intra-reservoir shales. It can also be explained, as mentioned over, that the layers situated at the sides of the chimneys pathway are fed with CO_2 from other sources. From layer 5 and up to layer 8 there could be observed high amplitudes situated around the chimney structures with no general orientation. This can also be explained by the original topography of the shale layers, or it may be created by the CO_2 transported by the chimney that in mechanically or chemical way altered the shale layer around.

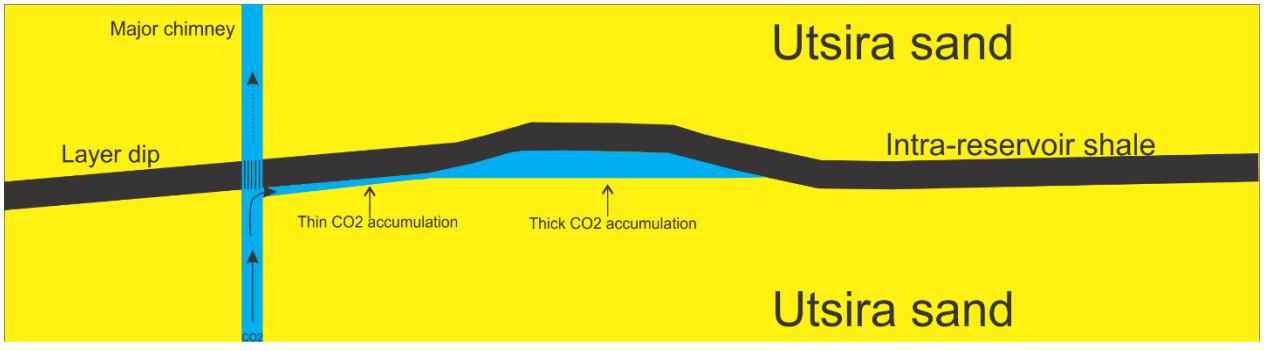

Figure 5.5: Schematic illustration for an explanation of the observed amplitude anomalies situated beside the major chimney structure

5.1.4 Pushdown observed for reflectors within and underneath the CO_2 plume

From the results in chapter 4 it was observed how the seismic structures beneath the CO_2 were shifted down. This was interpreted to be caused by the presence of CO_2 in the formation instead of normal saline fluid, and thus induce a longer travel time for the seismic wave (Rob Arts et al., 2004a; F. C. Boait et al., 2012; Zweigel et al., 2004). The pushdown was observed both beneath the CO_2 plume (figure 4.19) and internally in the plume (figure 4.20).

The pushdown beneath the whole plume show that the pushdown is greatest, with pushdown values over 30ms, at the central part of the plume and decreasing towards the edges. This may be caused by two ways (F. C. Boait et al., 2012): First, as the overview figure (figure 4.19) show is that there are more overlapping CO_2 layers around the center of the plume, giving more layers of CO_2 accumulation from top to base. Secondly, since the injection well is situated close to the center of the mapped out plume (R. Arts et al., 2004b) one should expect more (free) CO_2 in the areas between the small shales as the pressure from the injection well is greatest at that point. This gives more CO_2 that may be disseminated between the reflective horizons at the center of the plume.

Internally in the plume there were mapped out pushdown of the thick shale close to the top, which have the topmost CO_2 layer situated above (layer 9) (figure 4.20c), and over the middle CO_2 layer with best continuity and lateral extent (layer 5) (figure 4.20b). The shale layer was excellent for mapping of pushdown due to its continuity and visibility on the pre-injection baseline, whereas the CO_2 layer 5 could only be mapped on the post-injection datasets. The pushdown of layer 5 showed pushdown values up to 15ms when comparing the 2006 dataset with the 2001 dataset. The comparison between the 2004 and 2006 datasets indicated, in contrast, only few areas with pushdown. From figure 4.20a, it could be observed that the largest pushdown is observed between the 2001 and 2004 datasets, and that the interpreted plume horizons from 2004 and 2006 are situated at almost the same positions.

Since the thick shale could be interpreted prior to the injection, it was possible to look in detail on how this horizon was affected by CO_2 injection. The thick shale was expected to be pushed down due to the presence of CO_2 in the layer above (layer 9), and there were mapped pushdown with values up to 5ms on the 2004-1994 and 2006-1994 subtraction datasets. There was, in contrast, also observed areas on the thick shale that was not pushed down, even though there was CO_2 situated above. This is illustrated by the black areas inside the polygon of layer 9 on figure 4.20c. A closer look at these areas was done, which revealed that these areas were not pushed down due to underlying CO_2 accumulations from CO_2 layer 8 (figure 5.6). The presence of CO_2 accumulation at layer 8 will cause the interpreted horizon of the thick shale to be pulled up, and thus the total pushdown obtained from the overlying layer 9 will not be perfectly mapped. In order to see the effect of the under-pounding CO_2 on the thick shale layer, there have been mapped out the pushdown of the horizon and the topography of the horizon (figure 5.7). The polygon of the lateral extent of the underlying CO_2 layer is included in the figure.

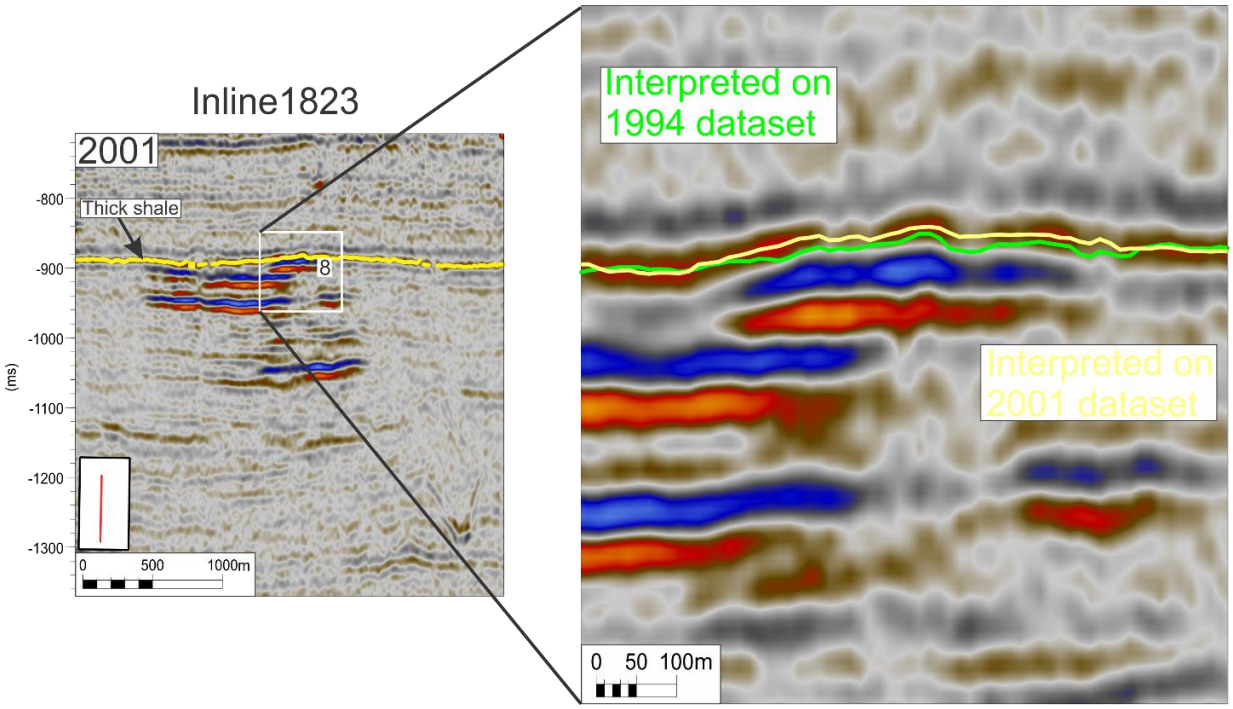

Figure 5.6: Seismic inline 1823obtained over the 2001 dataset. Indicated with the yellow color is the interpreted thick shale. The zoomed-in image reveals that the reflector from the thick shale is being pushed up due to presence of CO_2 accumulating beneath, where the green line represent the thick shale interpreted from the pre-injection dataset. The pullup feature is observed to be concentrated only at the area where CO_2 is situated beneath, which can disprove that the effect is obtained from differences of the acquisition parameters.

From figure 5.7a, it can be observed that the interpreted pushdown of the thick shale is mapped to be located just outside of the polygon that indicates the lateral extent of the underlying CO_2 layer. This supports the theory of layers being pulled up due to CO_2 pounding underneath. The pushdown of the shale can be clearly seen in the northward trending spread of the overlying CO_2 layer, because it is not underlain by CO_2. There can also be observed some pushdown mapped in the middle of the polygon, and it may be caused by that the effect of pushdown of the overlaying layer is greater than the pullup effect from the underlying layer. If we follow the topography of the thick shale with time (figure 5.7b), it can be observed how the horizon have a tendency to be pushed up within the lateral extent of the underlying CO_2 layer. The maximum values at the center seem to be lowering with time, but around the edges (and especially in the south) the horizon is pulled up a small distance, which supports the theory. This has also been observed on the top reflection and is likely to be an artefact, in part of the tuning effect and possible also due to unresolved stratigraphical complexity at the reservoir top (Rob Arts et al., 2004a), and is described as an apparent uplift produced by a local, shallow high-velocity region from (Loseth et al., 2009).

Because of these features, where the seismic signal is so affected by the injected CO_2 (pushdown + pullup), and that there cannot be 100% correlations between the datasets since they all have been acquired with slightly different acquisition parameters, the detail investigation of the injected CO_2 behavior in the storage formation becomes rather complicated.

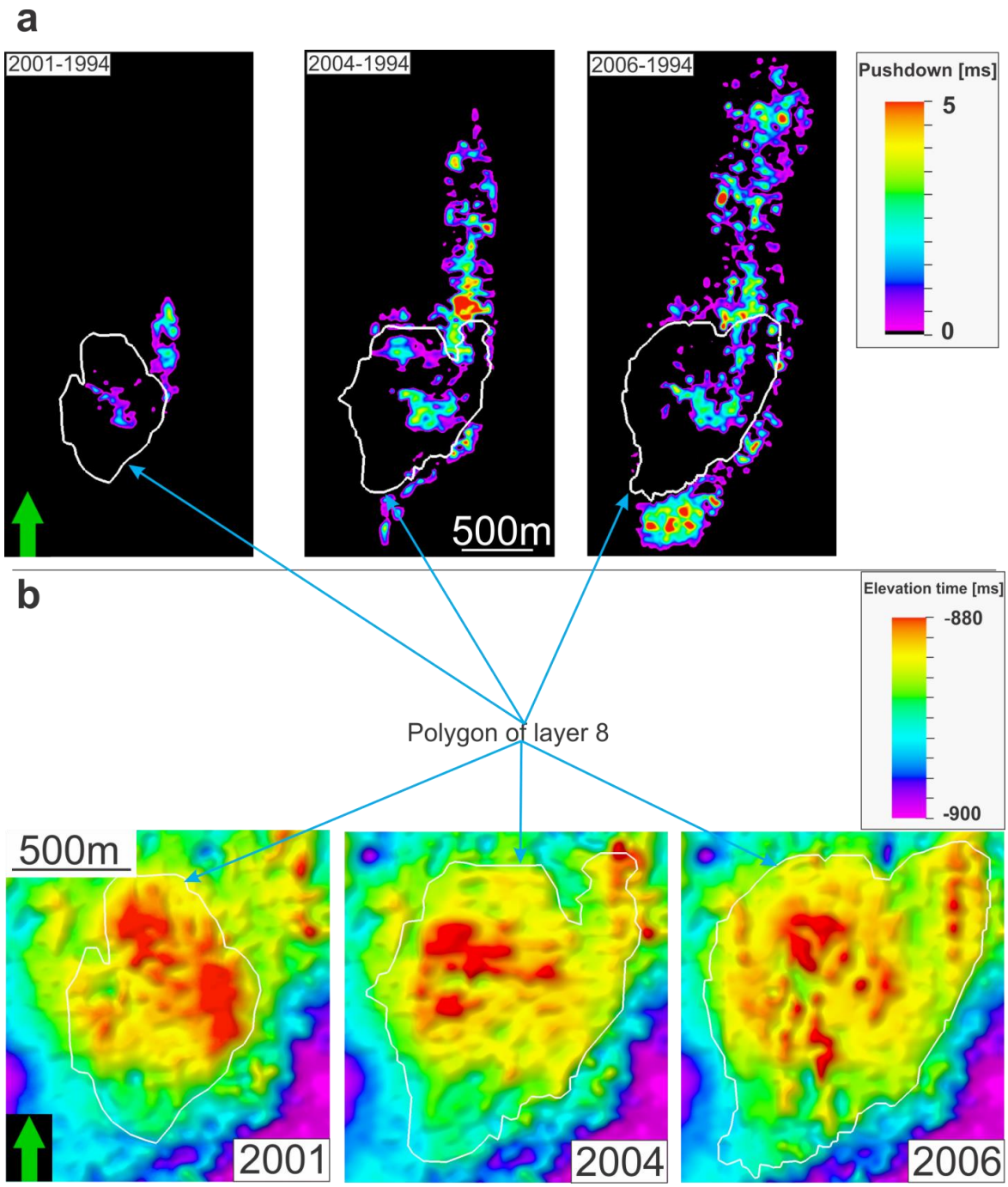

Figure 5.7: Effects of underlying CO_2 accumulations. a) Mapping of interpreted pushdown on the thick shale due to overlying CO_2 in layer 9 (same as seen in figure 4.20) within indicated lateral extent of underlying CO_2 layer 8. The pushdown is seen to be located just outside the layer extent (and in the middle). b) Map of thick shale horizon for each post-injection dataset. The topography can be seen to be affected by the location of the underlying CO_2 layer 5 (and it will also be affected by the overlying CO_2 layer 9). Rather than being pushed down from the overlying CO_2, it indicates to be pushed up a little bit due to the underlying CO_2.

5.1.5 Discussion summarize and outlook

Until now, there have been mapped out how the injected CO_2 is behaving in the subsurface, and it have been tried explained what might cause this, separately. The observed changes on the injected CO_2 is best described as a combination of several of the mentioned explanations.

It is evident that the individual plume layers are experiencing different growth models, where it is observed that the lower layers (especially layer 1-4) is experiencing more amplitude dimming compared to the overlying layers. The dimming of the lower layers are best explained by several factors. It is thought to be a combination between that the overlying reflections are causing a reduction in reflection energy (figure 5.3 & 5.8), and that the capping layers at these locations have been more broken over time. Amplitude analysis done by (F. C. Boait et al., 2012) have indicated that the acoustic attenuation cannot solely be the cause of the dimming observed on the lower plume layers, and it is instead partly attributable to CO_2 migration and/or CO_2 dissemination which reduce the impedance contrast between the sandstone and shale layers.

The mapping of the migration pathways supports this, where it is observed that there is several more reflection terminations on the intra-reservoir shale layers in the later datasets compared to earlier, indicating that there are more CO_2 being migrated through the shale layers on the later datasets. The observation of increase in high amplitudes in the upper sand package is also indicating a much more direct pathway for the CO_2 to migrate upwards, and can be caused by that the major interpreted chimney is experiencing a growth in permeability, or that there is several other chimney structures developing that transport CO_2 upwards. From the results in chapter 4.4.3 and from figure 5.8 supports that the best explanation is a combination of these two. Pushdown also show greatest values over the central part of the plume with pushdown values increasing with time, supporting the explanation that there must be more free CO_2 around the central part of the plume in later years, compared to the early years.

The plume layers are expected to follow the topography of the capping shale layers (Hermanrud et al., 2009; Lindeberg, Zweigel, Bergmo, Ghaderi, & Lothe, 2001), although the shales cannot be mapped from the seismic data. Whether all the internal shales are different from each other, or that they are having common features, is difficult to say anything certain about. It was tried to rationalize that since the two topmost reflectors have several common topographical feature, the other intra-reservoir shales would possible have some of the same features. The amplitude anomalies around the chimney structure suggest, in contrast, some more differences of the shales. Although there are many uncertainties regarding the chimney structure, as it is characterized with relatively much vertical displacement of the reflectors in the close region. The lateral extent of the intra-reservoir shales are also unknown, as some of the CO_2 layers may be trapped underneath shales that does not extend within the area of the chimney structure. The observed dimming of the lower CO_2 accumulations may also have something to do with the intra-shale topographies. It can be that the pressure from the injection well is changing with time, which will cause alteration of CO_2 flow beneath the shales. The CO_2 may be accumulating more under the shallower parts of the shale topographies, thus leaving larger areas that does not create a reflection amplitude.

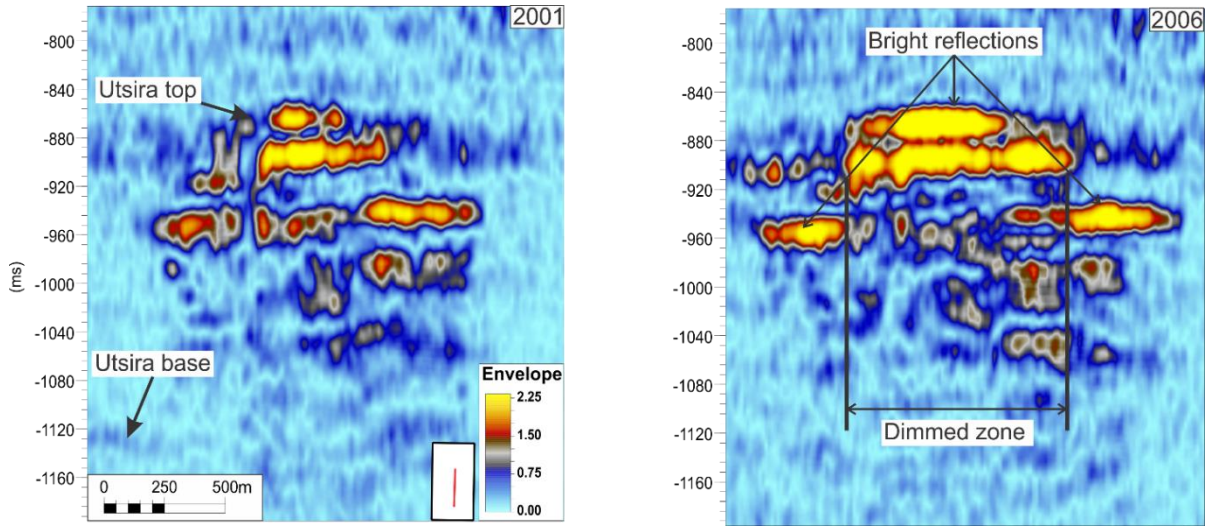

Figure 5.8: Seismic inline 1850 obtained over the 2001 and 2006 datasets, mapped with the envelope attribute. The 2006 dataset are indicating a large area in the central part of the plume with considerable reflection dimming. The dimming is considered being caused by reflection dimming from the two topmost layers (as it can be observed how the bright reflections at the top lies perfectly over the dimmed zone), and by dimming by free CO_2 migrating upward the formation, causing energy loss and discontinuity in the lower levels.

In order to say something about the possible outlook for the injection site, a correlation of the observed CO_2 movement and the behavior of the CO_2 accumulation within the topmost sand package is being used. It was observed (chapter 4.4.2.1) that the CO_2 is measured to be increasing in income flux beneath the Utsira top, where it has approximately grown over 775% in total amount from 2001 to 2006. If the increase of migrated CO_2 in the upper sand package is to be held the same for the future (will probably stabilize at some point), most of the injected CO_2 that is being injected close to the base will find its way up to the top and accumulate under Utsira top. The rest of the injected CO_2 is assumed to be migrating and accumulated under some internal shales, with layer 5 as most probable since it has shown its capability of storing a relative large amount of CO_2. In addition, some of the CO_2 will be trapped chemically and solubility by the formation waters and sediments in the storage reservoir (Eiken et al., 2011; Hermanrud et al., 2009). When the injection of CO_2 is being stopped some years in the future, it is expected that the CO_2 within the formation beneath the top accumulation that is not trapped solubility or by capillary forces, will be slowly migrating upwards and accumulate at the reservoir top.

The accumulation beneath Utsira top reveals that the CO_2 tend to follow the topography at the shallowest locations. As long as the formation holds the normal pressure gradient, it is expected that most of the injected CO_2 will find its way into the topmost part of the formation and be accumulating at these shallowest parts (R. A. Chadwick et al., 2009). From the mapped topography of the Utsira top and the accumulation of the topmost CO_2 layer (layer9) reveals that the CO_2 is spreading more in a northward direction with time, and is thus expected to stay in that way for the future. The same spreading is observed for the middle CO_2 layers (layer 5) only that it is not spreading as fast. The most probable future spreading is therefore thought to be in the north direction caused mainly from CO_2 layer 5 and 9, which also is suggested by the majority of the models so far (Eiken et al., 2011; Gibbins & Chalmers, 2008).

5.2 Storage security

From the result chapter it was indicating that there is few indication of leakage above the storage formation. The use of subtracted seismic time-lapse data (figure 4.22 b and c) has given us very good insight into observing differences in the overlying sealing sediments, and it cannot be observed any sign of leakage. The only exception is the artifacts/noise caused by the different acquisition parameters for the surveys. It was observed some high amplitudes just above the injection formation (figure 4.21), where the bright amplitudes was interpreted to be caused by shallow gas inside the sealing unit. However, the shallow gas found right above the injection formation was not interpreted to be caused by the injection of CO_2. This interpretation was based on that the amplitudes did not seem to change during injection, and were cancelled out when making subtraction cubes.

The origin of the shallow gas is, on the other hand, important to consider. If the shallow gas has migrated up from a deeper source and into the sealing unit, it may have migrated through the storage formation. This can leave migration routes that the injected CO_2 might take. This seems a little unlikely since there is no certain evidence for prior fluid migration upward through the sealing unit around the injection site, so the best interpretation of the shallow gases is that they might have formed biogenically *in situ*, and does not necessary imply migration from below (Andy Chadwick et al., 2008; S. Holloway, 2004). The nature and source of shallow gas needs therefore to address if indicators for its presence have been detected, and at Sleipner there is no clear spatial correlation between seismic amplitude anomalies and structures in the Utsira sand (S. Holloway, 2004).

The seabed seems also quite unchanged during the injection years, part from small changes caused most possible of the acquisition differences, which leaving it quite confident that no leakage has occurred where CO_2 has leaked into the seabed. This is also supported by ROV videos taken over the seafloor, where no seafloor changes or pockmarks have been observed (Eiken et al., 2011).

As the CO_2 is constantly being injected into the formation, it may cause overpressures. This can lead to cracking or faulting of the overlying sealing units, or it might cause re-faulting of the underlying polygonal faults that were created by the mobilizing of the softer sediments, and can be a threat to future safety. There is, however, no sign of overpressures in the sediments (Eiken et al., 2011) and might be due to the relatively high permeability in the storage sediments which allow the pressure to move fluids away from the injection site in great distances (Bergmoa, Grimstad, Lindeberg, Riis, & Johansen, 2009; R. A. Chadwick et al., 2012).

It is, however, important to stress the need for caution in this type of analysis. The detectable limit of the CO_2 is strongly dependent on the nature of the CO_2 accumulation. It have been presented that small thick accumulations in porous strata is detectable, but distributed leakage fluxes through low permeability strata may be difficult to detect with the use of conventional seismic techniques (Andy Chadwick et al., 2008). Leakages along faults within low permeability rocks would be difficult to detect as long as it does not change the fluid pressures, in which case it should be detectable on shear-wave seismic data (Andy Chadwick et al., 2008). At Sleipner the 4D seismic

data is, however, expected to be of sufficient quality to could confirm eventually leakages in the overburden caprock (Eiken et al., 2011).

6. Conclusion

The conclusions presented here have been drawn from the interpretation of four 3D seismic dataset over the CO_2 injection site at the Sleipner field. One of the cubes was acquired before injection began, whereas the three other were acquired at different times in the injection process. The combination of these cubes illustrates a 4D seismic time-lapse of the growing CO_2 plume.

- The injected CO_2 can easily be seen on the seismic post-injection datasets as bright reflection anomalies with negative reflection coefficients. The bright reflection anomalies are clearly separated from the reflection pattern from the baseline dataset.

- The injected CO_2 is observed to take nine separate locations/layers within the storage formation that is interpreted to be capped by intra-reservoir shales beneath a substantial reservoir topseal.

- The majority of the CO_2 layers tend to have an elliptical planform with the long axis in the NNE-SSW direction and eccentricities in the range 2.5 to 4.5, which is also observed for the total CO_2 plume. The distribution of the CO_2 within the layers are inferred to be a response of the topographies of the overlying shales. The topographies of the shales are thought to be in relation with the mud-diapirs at the formation base.

- Reflection pattern of CO_2 beneath these capping topographies have shown that there is a difference in the upper and lower part of the storage formation. The lower layers seem to experiencing dimming effect with time, whereas the upper layers experiencing amplitude growth. Two main effects have been thought to cause this dimming of the lower layers. The first effect is that while the upper layers are growing, they take away more energy from the seismic wave and thus leave less energy for mapping the lower layers. The second effect is that there are more CO_2 leaking from the lower layers as the capping effect of the shales reduces with time. The second effect will also cause more free fluids in the formation that attenuates the seismic signal. This is supported by the observed growth of the topmost layers and that there are observed more pushdown beneath the center of the plume.

- Caprock integrity have been observed to be intact as CO_2 is injected beneath, and there has not been observed any signs of leakage.

- Observations from the topmost CO_2 layer indicates a growth of input CO_2 flux, and is interpreted to even grow more in the future as the CO_2 seems to find more direct routes upward the formation. The CO_2 at this layer is seen to be migrating under the topography of the Utsira top horizon in a northward direction. The topography of the Utsira top horizon may therefore reveal future migration routes.

- Detailed mapping of the interior of the plume have been difficult due to several seismic effects caused by the injected CO_2; pushdown, pullup and acquisition differences between the datasets.

7. References

Akervoll, I., Lindeberg, E., & Lackner, A. (2009). Feasibility of Reproduction of Stored CO2 from the Utsira Formation at the Sleipner Gas Field. *Energy Procedia*, *1*(1), 2557-2564. doi: http://dx.doi.org/10.1016/j.egypro.2009.02.020

Andreassen, K. (2009). Marine Geophysics - Lecture notes in GEO-3123, 2012. *University of Tromsø*.

Arts, R., Eiken, O., Chadwick, A., Zweigel, P., van der Meer, B., & Kirby, G. (2004a). Seismic monitoring at the Sleipner underground CO2 storage site (North Sea). *Geological Society, London, Special Publications*, *233*(1), 181-191. doi: 10.1144/gsl.sp.2004.233.01.12

Arts, R., Eiken, O., Chadwick, A., Zweigel, P., van der Meer, L., & Zinszner, B. (2004b). Monitoring of CO2 injected at Sleipner using time-lapse seismic data. *Energy*, *29*(9–10), 1383-1392. doi: http://dx.doi.org/10.1016/j.energy.2004.03.072

Bergmoa, P. S., Grimstad, A.-A., Lindeberg, E., Riis, F., & Johansen, W. T. (2009). Exploring geological storage sites for CO2 from Norwegian gas power plants: Utsira South. *Energy Procedia*, *1*(1), 2953-2959. doi: http://dx.doi.org/10.1016/j.egypro.2009.02.071

Bickle, M., Chadwick, A., Huppert, H. E., Hallworth, M., & Lyle, S. (2007). Modelling carbon dioxide accumulation at Sleipner: Implications for underground carbon storage. *Earth and Planetary Science Letters*, *255*(1–2), 164-176. doi: http://dx.doi.org/10.1016/j.epsl.2006.12.013

Boait, F., White, N., Chadwick, A., Noy, D., & Bickle, M. (2011). Layer spreading and dimming within the CO2 plume at the sleipner field in the north sea. *Energy Procedia*, *4*(0), 3254-3261. doi: http://dx.doi.org/10.1016/j.egypro.2011.02.244

Boait, F. C., White, N. J., Bickle, M. J., Chadwick, R. A., Neufeld, J. A., & Huppert, H. E. (2012). Spatial and temporal evolution of injected CO2 at the Sleipner Field, North Sea. *Journal of Geophysical Research. Solid Earth*, *117*(3). doi: http://dx.doi.org/10.1029/2011JB008603

Büenz, S. (2013). Lecture notes in GEO-3131 - Energy and Environment Geoseminar *University of Tromsø*.

Chadwick, A., Arts, R., Bernstone, C., may, F., Thibeau, S., & Zweigel, P. (2008). *Best practice for the storage of CO2 in saline aquifers - observations and guidelines from the SACS and CO2STORE projects* Nottingham, UK, : (British Geological Survey Occasional Publication, 14).

Chadwick, A., Arts, R., Eiken, O., Williamson, P., & Williams, G. (2006b). Geophysical monitoring of the CO2 plume at Sleipner, North Sea. In S. Lombardi, L. K. Altunina & S. E. Beaubien (Eds.), *Advances in the Geological Storage of Carbon Dioxide* (Vol. 65, pp. 303-314): Springer Netherlands.

Chadwick, A., Noy, D., Lindeberg, E., Arts, R., Eiken, O., & Williams, G. (2006a). *Calibrating reservoir performance with time-lapse seismic monitoring and flow simulations of the Sleipner CO2 plume*. Paper presented at the GHGT-8: 8th International Conference on Greenhouse Gas Control Technologies, Trondheim, Norway. http://nora.nerc.ac.uk/1031/

Chadwick, R. A. (2004b). 4D seismic imaging of an injected CO2 plume at the Sleipner Field, central North Sea. In R. J. Davies (Ed.), *3D seismic technology : application to the exploration of sedimentary basins* (Vol. 29, pp. 311-320). London, UK: Geological Society of London.

Chadwick, R. A., Noy, D., Arts, R., & Eiken, O. (2009). Latest time-lapse seismic data from Sleipner yield new insights into CO2 plume development. *Energy Procedia, 1*(1), 2103-2110. doi: http://dx.doi.org/10.1016/j.egypro.2009.01.274

Chadwick, R. A., Williams, G. A., Williams, J. D. O., & Noy, D. J. (2012). Measuring pressure performance of a large saline aquifer during industrial-scale CO2 injection: The Utsira Sand, Norwegian North Sea. *International Journal of Greenhouse Gas Control, 10*(0), 374-388. doi: http://dx.doi.org/10.1016/j.ijggc.2012.06.022

Chadwick, R. A., Zweigel, P., Gregersen, U., Kirby, G. A., Holloway, S., & Johannessen, P. N. (2004a). Geological reservoir characterization of a CO2 storage site: The Utsira Sand, Sleipner, northern North Sea. *Energy, 29*(9–10), 1371-1381. doi: http://dx.doi.org/10.1016/j.energy.2004.03.071

CMI. (2011). Carbon Mitigation Initiative. Author: Roberta Hotinski. from http://cmi.princeton.edu/wedges/

Delepine, N., Clochard, V., Labat, K., & Ricarte, P. (2011). Post-stack stratigraphic inversion workflow applied to carbon dioxide storage: application to the saline aquifer of Sleipner field. *Geophysical Prospecting, 59*(1), 132-144. doi: 10.1111/j.1365-2478.2010.00905.x

Dudfield, P., & Woods, A. W. (2013). On the use of seismic data to monitor the injection of CO2 into a layered aquifer. *Earth and Planetary Science Letters, 368*(0), 132-143. doi: http://dx.doi.org/10.1016/j.epsl.2013.02.035

Eiken, O., Ringrose, P., Hermanrud, C., Nazarian, B., Torp, T. A., & Høier, L. (2011). Lessons learned from 14 years of CCS operations: Sleipner, In Salah and Snøhvit. *Energy Procedia, 4*(0), 5541-5548. doi: http://dx.doi.org/10.1016/j.egypro.2011.02.541

Galloway, W. E. (2002). Paleogeographic Setting and Depositional Architecture of a Sand-Dominated Shelf Depositional System, Miocene Utsira Formation, North Sea Basin. *Journal of Sedimentary Research, 72*(4), 476-490. doi: 10.1306/110801720476

Gibbins, J., & Chalmers, H. (2008). Carbon capture and storage. *Energy Policy, 36*(12), 4317-4322. doi: http://dx.doi.org/10.1016/j.enpol.2008.09.058

Gregersen, U., Michelsen, O., & Sørensen, J. C. (1997). Stratigraphy and facies distribution of the Utsira formation and the Pliocene sequences in the northern North Sea. *Marine and Petroleum Geology, 14*(7–8), 893-914. doi: http://dx.doi.org/10.1016/S0264-8172(97)00036-6

Hagen, S. (2012). *Sleipner*. Paper presented at the Knowledge Sharing in CCS projects - Workshop mobile, Alabama. www.statoil.com

Head, M. J., Riding, J. B., Eidvin, T., & Chadwick, R. A. (2004). Palynological and foraminiferal biostratigraphy of (Upper Pliocene) Nordland Group mudstones at Sleipner, northern North Sea. *Marine and Petroleum Geology, 21*(3), 277-297. doi: http://dx.doi.org/10.1016/j.marpetgeo.2003.12.002

Henriksen, E. (2013). Lecture notes in GEO-3119 - Petroleum prospecting. *University of Tromsø*.

Hermanrud, C., Andresen, T., Eiken, O., Hansen, H., Janbu, A., Lippard, J., . . . Østmo, S. (2009). Storage of CO2 in saline aquifers–Lessons learned from 10 years of injection into the Utsira Formation in the Sleipner area. *Energy Procedia, 1*(1), 1997-2004. doi: http://dx.doi.org/10.1016/j.egypro.2009.01.260

Herzog, H. J. (1999). The economics of CO2 capture.

Houghton, J. T. (2009). *Global warming: the complete briefing*. Cambridge: Cambridge University Press.

http://www.ecy.wa.gov/climatechange/whatis.htm. (2014). Climate change. from http://www.ecy.wa.gov/climatechange/whatis.htm

IPCC. (2005). *IPCC Special Report on Carbon Dioxide Capture and Storage. Prepared by Working Group III of the Intergovernmental Panel on Climate Change [Metz, B., O. Davidson, H. C. de Coninck, M. Loos, and L. A. Meyer (eds.)]*. the United States of America: Cambridge University Press, Cambridge, United Kingdom and New York, NY, USA, 442 pp.

IPCC. (2007). *Climate Change 2007: Mitigation. Contribution of Working Group III to the Fourth Assessment Report of the Intergovernmental Panel on Climate Change [B. Metz, O.R. Davidson, P.R. Bosch, R. Dave, L.A. Meyer (eds)]* (C. U. Press Ed.). Cambridge University Press, Cambridge, United Kingdom and New York, NY, USA., 862 pp.

Korbol, R., & Kaddour, A. (1995). Sleipner-Vest CO2 disposal - injection of removed CO2 into the Utsira foramtion. *Energy Conversion and Management, 36*(6-9), 509-512. doi: 10.1016/0196-8904(95)00055-i

Lindeberg, E., & Bergmo, P. (2003). *The long-term fate of CO2 injected into an aquifer*. Amsterdam: Elsevier Science Bv.

Lindeberg, E., Zweigel, P., Bergmo, P., Ghaderi, A., & Lothe, A. (2001). *Prediction of CO2 distribution pattern improved by geology and reservoir simulation and verified by time lapse seismic*.

Loseth, H., Gading, M., & Wensaas, L. (2009). Hydrocarbon leakage interpreted on seismic data. *Marine and Petroleum Geology, 26*(7), 1304-1319. doi: 10.1016/j.marpetgeo.2008.09.008

NETL. (2010). Best Practice for Geologic Storage Formation Classification: Understanding Its Importance and Impacts on CCS Opportunities in the United States. In N. E. T. Laboratory (Ed.).

NPD. (2011). NPD CO2 Storage Atlas. from http://www.npd.no/no/Publikasjoner/Rapporter/CO2-lagringsatlas/

NPD. (2014a). Exploration well 15/9-11. from http://factpages.npd.no/FactPages/Default.aspx?nav1=wellbore&nav2=PageView|Exploration|All&nav3=329&culture=en

NPD. (2014b). Exploration well 16/7-8S. from http://factpages.npd.no/FactPages/Default.aspx?nav1=wellbore&nav2=PageView|Exploration|All&nav3=4612&culture=en

Pham, V. T. H., Riis, F., Gjeldvik, I. T., Halland, E. K., Tappel, I. M., & Aagaard, P. (2013). Assessment of CO2 injection into the south Utsira-Skade aquifer, the North Sea, Norway. *Energy, 55*(0), 529-540. doi: http://dx.doi.org/10.1016/j.energy.2013.03.026

Rafaelsen, B. (2013). Lecture notes in GEO-3115 - Petroleum Geology, . *University of Tromsø*.

Ramberg, I. B., Bryhni, I., Nøttvedt, A., Solli, A., & Nordgulen, Ø. (2006). *Landet blir til: Norges geologi*. Trondheim: Norsk geologisk forening.

Rider, M. H. (1996). *The geological interpretation of well logs*. Caithness: Whittles.

S. Holloway, A. C., E. Lindberg, I. Czernichowski-Lauriol and R. Arts. (2004). Saline Aquifer CO2 Storage Project. In SACS (Ed.), *Best Practice Manual* (pp. 58).

Schlumberger. (2011). *Petrel 2010 - Interpreter's Guide to Seismic Attributes*.

Schlumberger. (2014). Ocean Plug-ins for Petrel - Multivolume Compare from http://www.ocean.slb.com/Pages/Product.aspx?category=allpetrel%28Base%29&cat=Petrel&pid=PCRE-B1%28Base%29

Selley, R. C. (1998). *Elements of petroleum geology*. San Diego: Academic Press.
Tissot, B. P., & Welte, D. H. (1984). *Petroleum formation and occurrence*. Berlin: Springer.
Torp, T. A., & Gale, J. (2004). Demonstrating storage of CO2 in geological reservoirs: The Sleipner and SACS projects. *Energy, 29*(9–10), 1361-1369. doi: http://dx.doi.org/10.1016/j.energy.2004.03.104
Worldometer. (2013). Worldometers. from http://www.worldometers.info/world-population/#pastfuture
Zweigel, P., Arts, R., Lothe, A. E., & Lindeberg, E. B. G. (2004). Reservoir geology of the Utsira Formation at the first industrial-scale underground CO2 storage site (Sleipner area, North Sea). *Geological Society, London, Special Publications, 233*(1), 165-180. doi: 10.1144/gsl.sp.2004.233.01.11